FIBER-OPTIC BUNDLE FLUORESCENCE MICROSCOPY

FOR FUNCTIONAL BRAIN ACTIVITY MAPPING

by

Jaepyeong Cha

A dissertation submitted to the Johns Hopkins University in conformity with the

requirements for the degree of Doctor of Philosophy

Baltimore, Maryland

May 2016

ABSTRACT

Understanding the relationship between cellular activities in the animal brain and the emerging patterns of animal behavior is a critical step toward completing the Brain Activity Map. This dissertation describes the development of fiber-bundle microscopy capable of high-resolution cellular imaging, for mapping of functional brain activity in freely moving mice. As a part of this work, several fiber-bundle microscope systems and image processing algorithms were proposed and developed. These optical imaging methods and system performance were tested and evaluated by performing *in vivo* animal brain imaging.

Several fiber-bundle imaging devices, including a dual-mode confocal reflectance and fluorescence micro-endoscope, a single ball-lens imaging probe, and a spatially multiplexed fiber-bundle imager, were designed and developed for high-resolution imaging of brain cells and visualization of brain activity. A dual-mode micro-endoscope, simultaneously achieving laser scanning confocal reflectance and fluorescence imaging, was developed to quantitatively assess gene transfection efficacy using human cervical cancer cells. A single ball-lens integrated imaging probe was designed for endoscopic brain imaging. Lastly, a spatially multiplexed fiber-bundle imager that allows concurrent monitoring of astrocytic activities in multiple brain regions and enables optical manipulation with cell-specific targeting was proposed and experimentally demonstrated.

Novel image-processing algorithms were used along with the developed imaging systems. Structured illumination employing a digital micro-mirror device (DMD) was integrated into the system to achieve depth-resolved imaging with a wide-field

illumination fiber-bundle microscope. Data from super-resolution fiber-bundle microscopy based on the linear structured illumination were numerically processed to extend the lateral resolution beyond the diffraction limit.

To evaluate the performance of the developed fiber-bundle microscope systems and image reconstruction algorithms, the systems and methods were each tested and validated on *in vivo* animal models, namely transgenic mice expressing a genetically encoded Calcium indicator (GCaMP3) within astrocytes. We showed that locomotion triggers simultaneous activation of astrocyte networks in multiple brain regions in mice. We have also demonstrated real-time cellular-resolution dual-color functional brain imaging in mice. Finally, we established a platform that allows real-time and non-invasive imaging of the intact central nervous system of freely behaving mice. Using this platform, we observed, for the first time, physiologically relevant activation of astrocytes during behaviorally relevant tasks and in the natural setting.

In addition, we present a proof-of-concept study by using a fiber-bundle ring light-guided portable multispectral imaging (MSI) platform capable of tissue characterization and preoperative surgical planning for intestinal anastomosis.

Dissertation Committee:

Prof. Dr. Jin U. Kang, ECE (Thesis Advisor, Dissertation Reader)

Prof. Dr. Amy C. Foster, ECE (Dissertation Reader)

Prof. Dr. Mark Foster, ECE

Prof. Dr. Dwight E. Bergles, Neuroscience (Co-advisor)

ACKNOWLEDGEMENTS

During my graduate years at Johns Hopkins University, I have been exceedingly blessed to be accompanied and supported by a wonderful group of people. The completion of my dissertation would not have been possible without their help and encouragement. It is with great pleasure that I would like to express my deepest gratitude to them.

First, I would like to gratefully and sincerely thank my thesis advisor, Dr. Jin U. Kang, for his guidance, leadership, patience, and understanding during my graduate studies. His mentorship, his outstanding experience, and his insightful advice always guided me and my research along the correct path. For the past 5 years, I have seen myself grow to become an independent researcher and I learned the invaluable academic research skills, as well as traits of openness and self-confidence, from Dr. Kang.

I would also like to thank my co-advisor, Dr. Dwight E. Bergles, for his patience during our collaboration. Dwight has given me a great opportunity to interact with an interdisciplinary team of neuroscientists and optical engineers. I am indebted to Dr. Bergles for giving me the opportunity to work with some exemplar scientists (Martin, Andres, and Yung-Tian) from his lab. This thesis has benefited greatly from their input and their quality neuroscience research.

I would like to express my earnest appreciation to the members of my dissertation committee and graduate board oral (GBO) exam committee, Dr. Amy C. Foster, Dr. Mark Foster, Dr. Jacob B. Khurgin, Dr. Xingde Li, Dr. Solange P. Brown, Dr. Andres Hurtado, and Dr. Peter Gehlbach, for their constructive review of my dissertation research. A special "thank you" is to Solange, who has helped me to embark on my thesis

TABLE OF CONTENTS

LIST OF FIGURES

CHAPTER 1: INTRODUCTION

1.1   Motivation

One of the key challenges in biology is studying intact biological systems with both

global perspective and local precision [1, 2]. This is especially true for brain science.

Over the last few decades, enormous efforts have been directed towards determining both

local and global connectivity within the brain, but these efforts have been impeded by the

fact that high-resolution brain-wide cellular imaging of the whole brain in live animals is

hardly achievable. Although electrophysiological approaches have been used to study the

firing patterns of neurons during animal behaviors [3, 4], dense mapping of brain

activities has been hampered due to the spatial resolution and sampling limitations of

electrode arrays.

However, recent optical imaging technologies, in tandem with the development of

fluorescent probes such as voltage sensitive dyes (VSDs) [5] and genetically encoded

calcium indicators (GECIs) [6, 7], have allowed comprehensive sampling of both

neuronal and non-neuronal cells in live animals [8, 9], and thus have greatly expanded

our ability to study brain activities. In addition, recent developments in fiber-optic

imaging techniques have enabled functional brain imaging in freely moving animals [10].

Fiber-optics allows the construction of lightweight headpieces that replaces bulky optical

components and permit the use of high-performance light sources and detectors with

increased experimental flexibility [11].

Among the variety of fiber-optic techniques used for a wide range of clinical and

preclinical research [12], fiber-bundle based optical imagers have been proven to be

excellent tools for *in vivo* studies [13, 14]. The fiber bundles' small diameter, flexibility,

and long probe length allow easy access to a wide range of organs and small cavities to deliver the probe deep into the body and provide high-resolution imaging. Earlier studies have shown that fiber bundle based brain imaging in freely moving mice could acquire and relate functional cellular signals from cortical and deep brain regions to animal behavior [10, 15].

Nonetheless, fiber bundle imagers exhibit several inherent limitations such as honey-comb pattern noises, cross-talk between adjacent fibers, and low coupling efficiency, that limit its resolution and image signal-to-noise ratio (SNR) [16-18]. Further improvements to spatial resolution, higher imaging depth and sensitivity are needed to make functional imaging in freely moving animals more effective. At the same time, despite the technical advances in miniaturized optics and electronics, these imaging approaches have so far been applied to single brain regions at a time, and simultaneous monitoring of cellular events from multiple brain regions has still not been achieved [19, 20]. If the head-tethered fiber-optic microscope could be configured to provide functional connectivity imaging from multiple brain regions while animals behave freely that would enable a wide range of neuroscience studies [21]. This would lead to unprecedented advances in our understanding of the functional connections between cellular networks and complex animal behaviors and open new doors to mapping functional brain activity.

1.2   Research Objectives

Throughout this research, my emphasis has been to design, develop and implement a high-resolution fiber bundle microscope system for imaging functional brain activities in freely moving animals through optimizing its performance by testing numerous imaging

system designs, developing image processing algorithms, and finally validating them through *in vivo* animal studies. The above-mentioned objectives are specifically addressed in the following aims:

1. Develop fiber bundle imagers that provide high-resolution cellular imaging and visualization of astrocyte activities within the live mice brain.

2. Improve the image quality of wide-field fiber bundle imagers by implementing a digital micromirror device (DMD)-based linear structured-illumination and computational reconstruction algorithm.

3. Evaluate the system performance throughout *in vivo* animal studies using a freely moving transgenic mouse expressing genetically encoded calcium indicator (GCaMP3) within astrocytes.

1.3   Dissertation Overview

This dissertation presents the development of fiber bundle-based microscopic imaging technologies and their applications in brain science and biomedical imaging. Chapter 2 reviews the fundamental principles of fiber-optic fluorescence microscopy. Chapter 3 presents optical layouts and imaging probe designs of fiber bundle imagers. Chapter 4 describes the optical sectioning and super-resolution processing techniques to improve wide-field fiber bundle image quality. Chapter 5 validates fiber-bundle microscope systems and image restoration algorithms through *in vivo* animal studies using a transgenic mouse model. Chapter 6 illustrates a proof-of-concept study using a portable multispectral imaging (MSI) platform for tissue characterization and preoperative

surgical planning in intestinal anastomosis. Chapter 7 summarizes the dissertation and proposes future directions of research.

CHAPTER 2: FUNDAMENTAL PRINCIPLES OF FIBER-OPTIC FLUORESCENCE MICROSCOPY

2.1   Optical Fibers

Optical fibers are circular dielectric waveguides that can transmit light with extremely low losses. It consists of a dielectric core with a higher refractive index surrounded by a concentric cladding with a lower refractive index. Fibers are typically made of silica doped with index-modifying dopants such as GeO_2. A protective coating of one or two layers of cushioning material (such as acrylate) is used to protect the fragile glass fibers from mechanical stress and external forces.
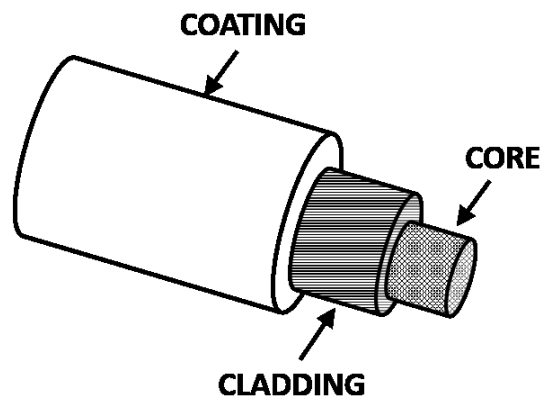
Figure 2.1. General composition of optical fiber.

Optical fibers can be characterized by their optical structure and light transmission properties. In general, optical fibers can be classified into two types: single mode fibers and multimode fibers. As the names imply, the number of modes that the fibers support classifies them as either single or multimode optical fibers. The basic structural differences are the core size and the index difference between the core and the cladding.

2.1.1 Single-mode Fibers (SMFs)

The core sizes of single mode fibers (SMFs) are typically small, less than 10 μm. A fiber
core of this size allows only the fundamental or lowest order mode to propagate if the
index difference between the core and cladding layers is sufficiently small. SMFs support
only one lowest guided mode. The normalized frequency V is a dimensionless parameter
that relates in a very useful manner the core radius a and the numerical aperture NA to the
operating wavelength λ;

$$V = \frac{2\pi a}{\lambda} NA, \qquad (1)$$

To satisfy the condition for an SMF, V has to be less than or equal to 2.405. When
$V < 2.05$, only the lowest order mode is guided, while higher-order modes become leaky
waves. For low V values (< 1.0), most of the power in the fiber propagates in the cladding
layer. Power transmitted by the cladding can easily become leaky since the mode angle is
quite small for such a weakly guided fiber when the fiber bends. Thus, the value of V
should remain near 2.405 for applications requiring a short bend radius.

The advantage of having only a single mode within an optical fiber is that the
signal distortion caused by modal dispersion due to the different phase and group
velocities associated with each guided mode can be avoided. SMFs are commercially
used for all the long-haul fiber optic communication networks.

2.1.2 Multi-mode Fibers (MMFs)

Multi-mode fibers (MMFs) support more than one guided mode. The number of guided
modes supported depends upon the physical parameters (core radius, relative refractive

index difference) of the fiber and the wavelength of the transmitted light, which are included in the normalized frequency V of the fiber as mentioned in the previous section.

Typically, MMFs have large core diameters in excess of 50 μm, which is sufficient to support a large number of higher-order modes. A large core size and a higher NA have several advantages. Light can be easily coupled into the MMFs with high coupling efficiencies. The higher NA and larger core size make the fiber connection easier and enable the transmission of higher optical power. However, MMFs also have some disadvantages. As the number of modes increases, the effect of modal dispersion increases. Modal dispersion (intermodal dispersion) means that modes arrive at the fiber end at slightly different times, which causes the light pulse to spread. Modal dispersion limits the bandwidth in systems used for optical communications [22].

There are two different types of core structure for MMFs:

2) Step-index MMFs

The step-index fiber is as shown below in Figure 2.2. For fibers with large V parameters, the number of modes can be approximated as [22]:

$$M = \frac{4}{\pi^2}V^2, \qquad (2)$$
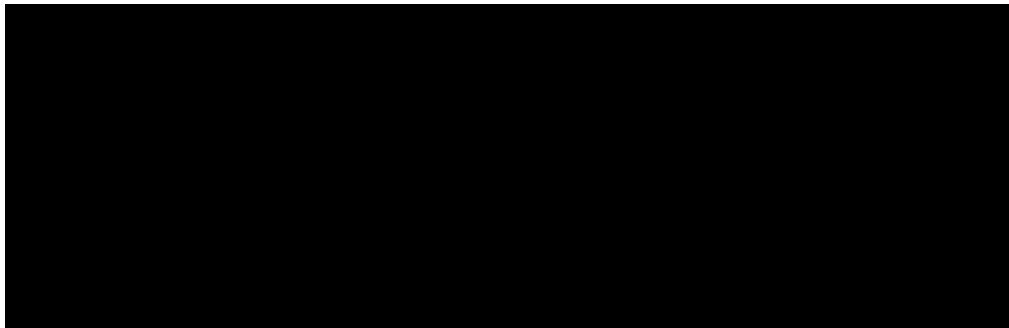
Figure 2.2. Step-index multi-mode fiber.

b) Graded-index MMFs
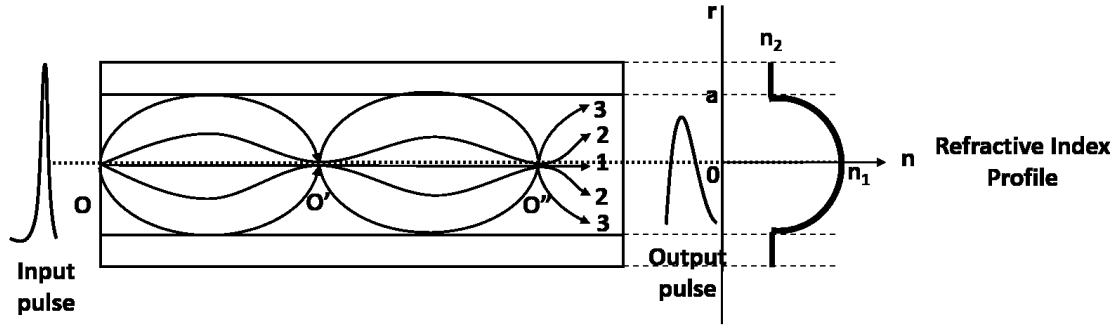
Figure 2.3. Graded-index multi-mode fiber.

In graded-index fibers, as their name suggests, the value of the refractive index of the

core $n(r)$ varies with the radial distance (r).

$$n(r) = \begin{cases} n_1[1 - \Delta(r/a)^\alpha]; & r < a, \\ n_1(1 - \Delta) = n_2; & r > a, \end{cases} \qquad (3)$$

where

$$\Delta = \frac{n_1^2 - n_2^2}{2n_1^2} \approx \frac{n_1 - n_2}{n_1}, \qquad (4)$$

and α, called the grade profile parameter, determines the steepness of the profile. This

function drops from n_1 at $r=0$ to n_2 at $r=a$. For $\alpha =1$, $n_2(r)$ is linear, and for $\alpha =2$ it is

quadratic. As α →∞, $n^2(r)$ approaches a step function [22]. Rather than being reflected at

an abrupt core/cladding boundary, the wavefront of light is steered continuously as it

traverses the refractive index gradient. Light travels faster through the outer, lower

refractive index medium, and hence tends to keep up with light propagating in the inner

regions of the core, resulting in less temporal dispersion in the light propagation.

2.1.3 Fiber bundles

A coherent fiber bundle is a bundle of SMF optic cores assembled into a 2D matrix where the relative position of the individual fiber is maintained throughout the length of the bundle. Tens of thousands of fibers are combined in a bundle, with each fiber transferring one spot of light from an object at one end of the bundle to a conjugate point at the opposite end of the fiber. This process constitutes an image transfer. In addition to image transfer, fiber bundles have other advantages in illumination systems; for example, by feeding a large fiber bundle with a single light source and splitting the bundle into two or more branches, it can be used to illuminate multiple locations. They can also be used to merge light from several sources into a single output. However, since fiber cores are discrete, the object plane is sampled discretely. This complicates the image reconstruction, as shown in Figure 2.4.
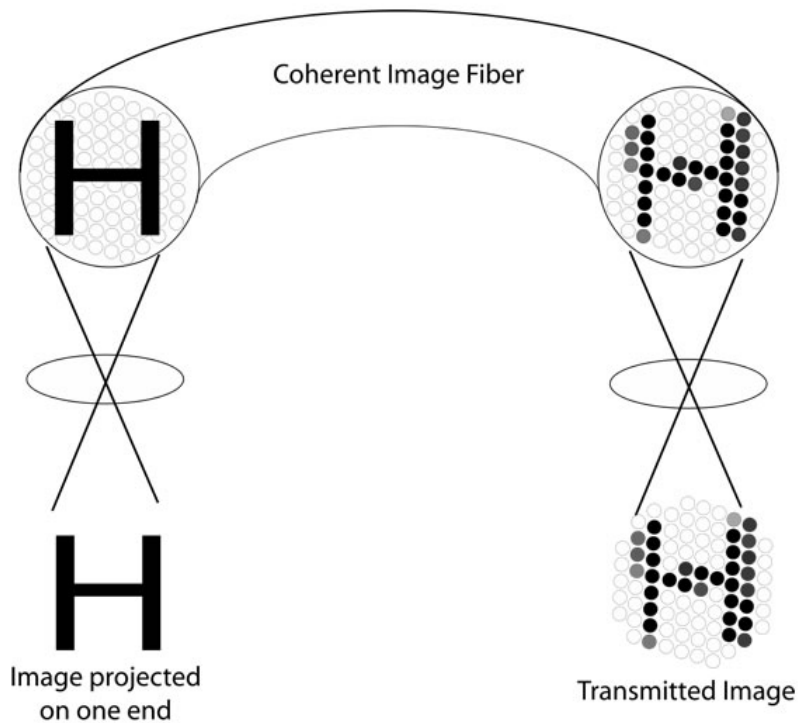
Figure 2.4. Image formation in coherent image transfer fiber bundle.

9

2.2   Fluorescence Microscopy

Fluorescence microscopy is a powerful tool for biologists. It provides high-resolution cellular imaging and visualization of physiological processes in a living cell or tissue with fluorescent markers. Many new techniques have been developed over the last few decades and these advances have benefited from the recent developments of synthetic organic dyes, fluorescent proteins, and semiconductor quantum dots.

Fluorescence can be characterized by the absorption of a photon and the emission of a photon at longer wavelength, which is referred to as the Stokes Shift process. The fluorescence molecule, originally in the ground state, turns into a high-energy state when the energy from excitation light is absorbed and excited. When returning to the ground state, the molecule emits a photon with energy equivalent to the difference between the lowest excited state and the ground state. As the emitted photon has less energy than that of absorbed photon, a longer wavelength of light is released.

The basic function of a fluorescence microscope is to excite the fluorescent probes of the target sample and detect the emission light. However, optimal use of fluorescence microscopy requires a basic understanding of its working principles. In the following sections, we introduce the basic terms and two forms of fluorescence microscopy.

2.2.1   Point-spread-function (PSF) and Resolution

The impulse response is used to describe the system response to an ideal sharp input delta function. With an optical microscope, the input delta function is a single point source, and the corresponding image through the optical microscope is referred to as the point-

spread-function (PSF). In general, the PSF has radial symmetry and can be described as an airy disk, which defines the resolution of the optical microscope.

The resolution of a microscope refers to the ability to distinguish two objects that are close to each other. The smallest separation where the objects can be distinguished is considered as the resolution of the microscope. There are various criteria for measuring the resolution of an optical system.

2.2.1.1 Abbe criterion

Abbe's diffraction limit defines a maximum resolution that can be achieved by a conventional light microscope and it can be easily derived by calculating the maximum spatial frequency of an object which will diffract light into the microscope aperture.
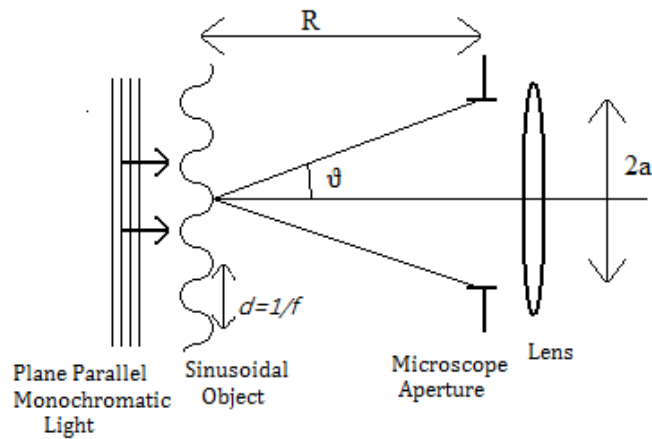
Figure 2.5. Diffraction of sinusoidal object with parallel light.

To find the maximum spatial frequency, one can use a single sine pattern. If the object is illuminated by plane parallel coherent light, the maximum of the resulting diffraction can be obtained at an angle:

$$\theta = \sin^{-1} \lambda f \cong \lambda f , \qquad (5)$$

11

where f is the spatial frequency of the object and λ is the wavelength of the illumination light. The maximum angle at which the light enters the microscope aperture is defined by

$$\theta_{max} = \tan^{-1} a/R \cong a/R,\qquad(6)$$

where a is the aperture of the microscope and R is the distance between the object and aperture. The maximum resolvable frequency and the minimum period are given by:

$$f_{max} = a/\lambda R,\qquad(7)$$

$$d_{min} = \lambda R/a,\qquad(8)$$
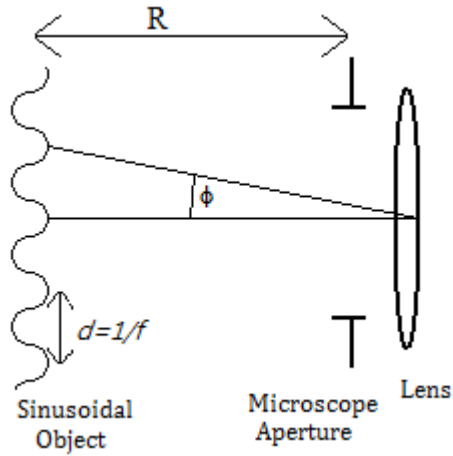
Figure 2.6. Smallest resolvable angle by the Abbe criterion.

The minimum detectable angle ϕ at the microscope is given by

$$\phi = d_{min}/R = \lambda/a,\qquad(9)$$

The smallest detectable spot, l, is defined as

$$l = d_{min}/2 = f\lambda/2a.\qquad(10)$$

Substituting the numerical aperture of the lens $NA = n\sin\vartheta = n\sin\tan^{-1}\frac{a}{f} \cong \frac{a}{f}$, we have

$$l = \lambda/2NA.\qquad(11)$$

2.2.1.2 Rayleigh criterion

According to the Rayleigh limit, two point objects can be resolved when the distance

between them is greater than the difference between the maximum and the first minimum

of the diffraction pattern. To obtain Airy patterns, we assume a circular aperture of the

lens.

$$\psi(x,y) = \psi(r) = circ(r/r_0), r = \sqrt{x^2 + y^2}$$

If we compute the Fourier transform of the *circ*-function,

$$F_{xy}(\psi) = \psi(k_x, k_y) = \iint \psi(x,y)\exp[j(k_x x + k_y y)]dxdy.$$

Introducing new variables,

$$x = r\cos\theta, y = r\sin\theta, k_x = k_r \cos\phi, k_y = k_r \sin\phi,$$

$$\psi(k_x, k_y) = \hat{\psi}(k_r, \phi) = \int_0^\infty \int_0^{2\pi} \hat{\psi}(r)\exp[jk_r r(\cos\theta\cos\phi + \sin\theta\sin\phi)]rd\theta dr$$

$$= \int_0^\infty r\hat{\psi}(r)\int_0^{2\pi} \exp[jk_r r\cos(\theta - \phi)]d\theta dr$$

$$J_0(\beta) = \tfrac{1}{2\pi}\int_0^{2\pi} \exp[j\beta\cos(\theta - \phi)]d\theta,$$

where $J_0(\beta)$ is the zeroth-order Bessel function. Then, we can obtain the *Fourier-Bessel*

transform which arises in circularly symmetric problems.

$$B(\hat{\psi}(R)) = \hat{\psi}(k_r) = 2\pi \int_0^\infty r\hat{\psi}(r)J_0(K_r r)dr$$

Finally, using the relationship

$$aJ_1(a) = \int_0^a \beta J_0(\beta)d\beta,$$

13

$$\hat{\psi}(k_r) = \frac{2\pi r_0}{k_r} J_1(r_0 k_r),$$

we have

$$\hat{\psi}(r,z) = \psi(x,y,z) \propto \frac{2\pi r_0 z}{k_0 r} J_1(\frac{r_0 k_0}{z} r).$$

$$\left\{2\frac{J_1(\pi\zeta)}{\pi\zeta}\right\}^2$$
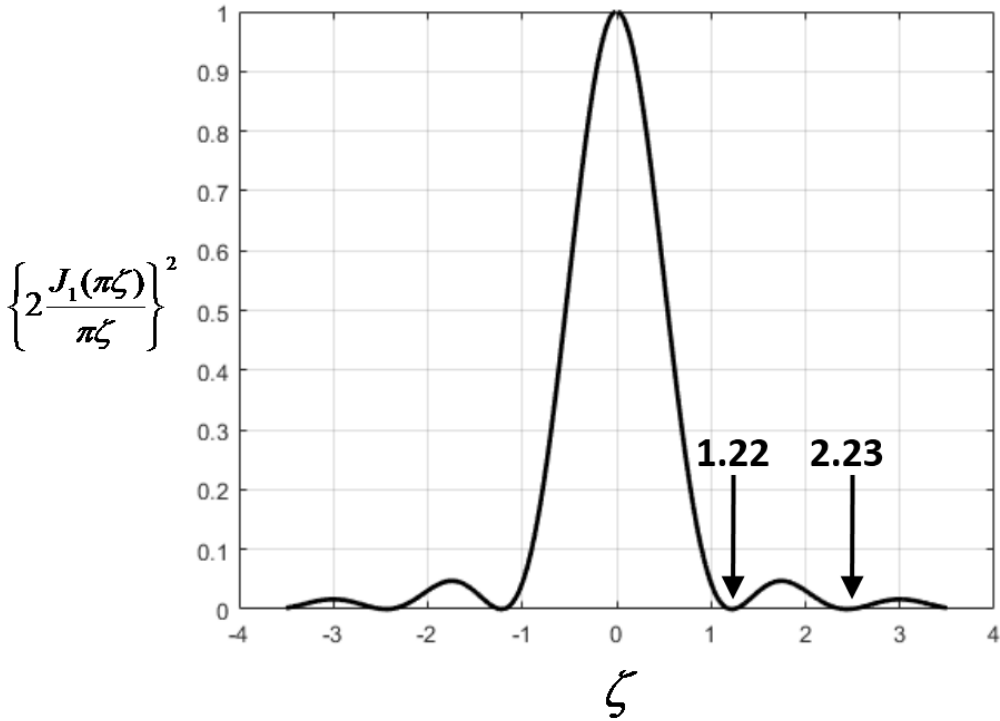
Figure 2.7. Plot of Airy pattern of the circular aperture; arrows indicate 1.22 and 2.23.

The intensity is proportional to $|\psi(r,z)|^2$ and is depicted in Figure 2.7. The plot is called an Airy pattern. The two arrows in the figure point to the first and second zero of the pattern, which are at $\zeta = 1.22$ and $\zeta = 2.23$, respectively. It follows the minimum separation, $l = 1.22\lambda(\frac{f}{2a}) = 0.61\lambda / NA$, which is the Rayleigh criterion.

2.2.1.3 Sparrow criterion

The Sparrow resolution limit is defined as the distance between two point sources where the images no longer have a dip in brightness between the central peaks, but rather

14

exhibit constant brightness across the region between the peaks. Mathematically, the Sparrow criterion is stated in terms of the second spatial derivative of the intensity:

$$\left[\partial^2 I(\xi)/\partial \xi^2\right]_{\xi=0} = 0$$

For a circular aperture, the Sparrow criterion becomes

$$l = 2.976\lambda/\pi 2a = 0.95\lambda/2a = 0.47\lambda/NA.$$

The Sparrow resolution limit is closer to the Abbe value and approximately two-thirds of the Rayleigh resolution limit.

2.2.2 Wide-field Fluorescence Microscopy (WFFM)

In the most basic form, wide-field fluorescence microscopy (WFFM) involves a light source, excitation and emission filters, and an objective lens, as depicted in Figure 2.8. The emission light from the sample is collected by a 2D array detector, such as a CMOS or CCD camera. The main advantages of WFFM are that it is the least expensive technique, provides good spatial resolution, has fast temporal resolution, and in many cases requires minimum amounts of excitation light power. A wide-field microscope cannot differentiate photons from different axial planes; therefore, the lateral resolution can be calculated according to the Rayleigh diffraction limit expressions,

$$r_{x,y} = \frac{0.61\lambda}{NA}, r_z = \frac{2\lambda\eta}{NA^2},$$

where λ is the wavelength of the emitted light, η is the refractive index of the medium between the lens and specimen, and NA is the numerical aperture of the objective. The main disadvantage of WFFM is that all of the emitted light is integrated through the sample in z-direction. Therefore, it is difficult to achieve depth-resolved imaging.

15
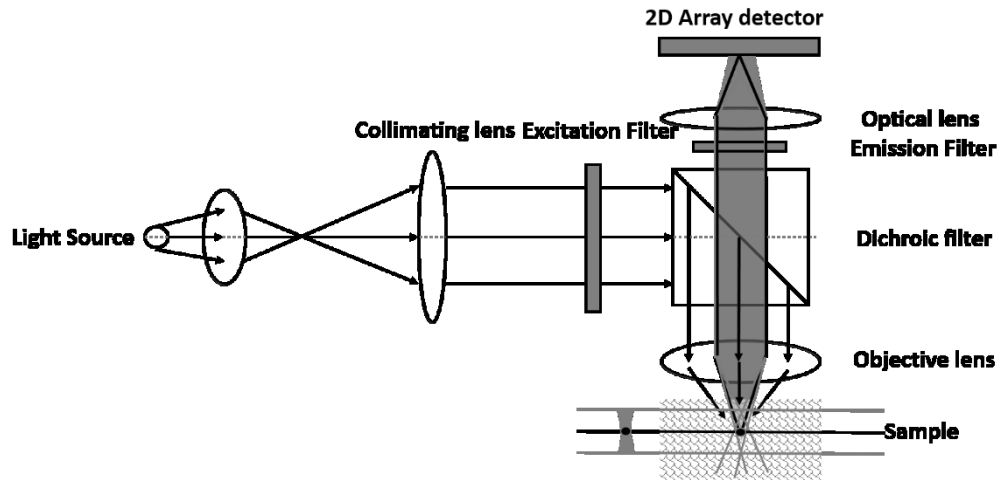
Figure 2.8. Schematic of wide-field fluorescence microscope.

2.2.3   Laser Scanning Confocal Microscopy (LSCM)
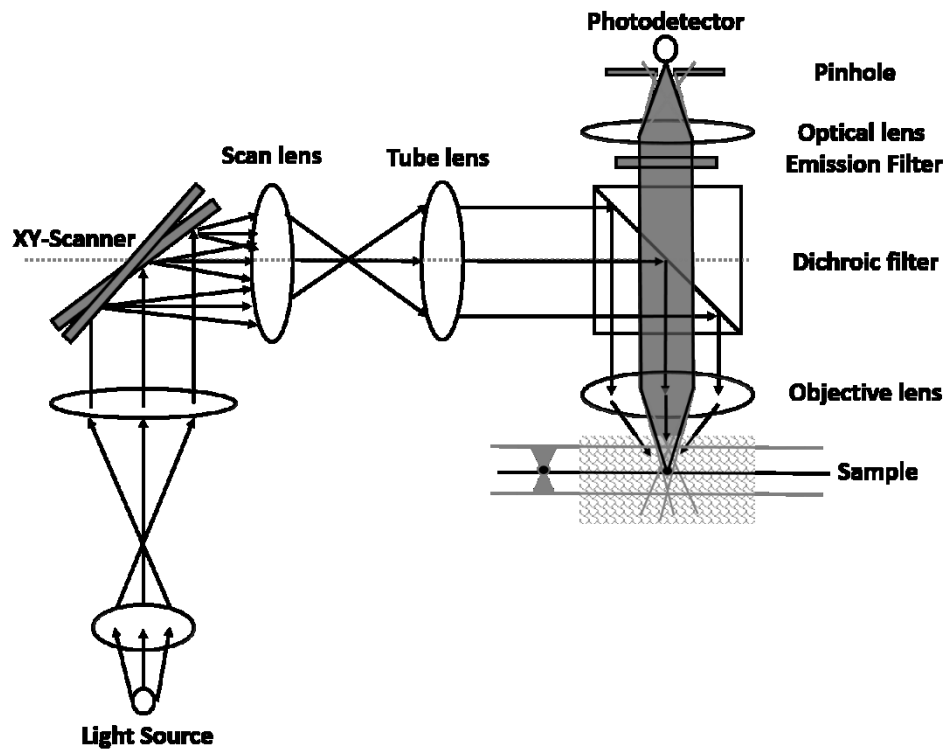
Figure 2.9. Schematic of laser scanning confocal microscope.

As Figure 2.9 shows, the light source is directed to the sample through collimating and scanners, and an objective lens that focuses the light to a diffraction limited spot in the sample. Emission light from the sample is directed to a photodetector, such as a PMT, through a pinhole that is in conjugate image plane to the point of focus in the sample. After spatial filtering by the pinhole, the fluorescence light is collected by the detector. At the heart of the confocal microscope is the pinhole. When placed in the conjugate image plane, it enables optical sectioning. The light originating from other off-focus planes is blocked from passing through the pinhole. Therefore, only the in-focus light can be detected by the detector. For a confocal system, the pinhole radius is set smaller than r_{airy} and the full width at half maximum (FWHM) extent of both the lateral and axial PSF are approximately 30% narrower than that of a conventional wide-field microscope [23]. This improved PSF can be explained by Lukosz's principle [24] and thus,

$$r_{x,y} = \frac{0.4\lambda}{NA}, r_z = \frac{1.4\lambda\eta}{NA^2}$$

The main advantage is that one may optically section the sample with high-resolution. Another advantage is the versatility for multicolor imaging, variable pinhole sizing for optimal sectioning according to the sample thickness. Disadvantages of LSCM include the low scan speed, photobleaching, and/or photo-damage on the sample.

2.3   Fiber-optic Fluorescence Microscopy

Optical fibers are being investigated for use in fluorescence microscopes, optical coherence tomography (OCT) scanners, and laser scanning nonlinear microscopy systems [12, 25, 26]. Their main difference from standard bulk optic imaging systems is that the free-space beam path and bulk optics components are replaced by optical fibers and fiber optic components. This allows the imaging probe to be remoted into various body cavities. Optical fibers are immune to electromagnetic interference, therefore microscopes utilizing optical fibers can be used in conjunction with magnetic resonance imaging (MRI), computed tomography (CT), and other imaging modalities without any interference. The imaging fiber can be an SMF, an MMF, or a multi-core fiber bundle. Imaging probes typically consist of optical lenses at the distal end of the fiber, where lenses such as micro lenses, graded index (GRIN) lenses, or ball lenses are used.

2.3.1   SMF-based Fiber-optic Microscopy

One of the simplest fiber endoscope configurations is a microscope based on SMF. In the case of SMF microscopes, each image pixel is obtained sequentially using mechanical scanning methods to generate two- or even three-dimensional images. Two main forms of distal scanning are based on scanning mirrors or scanning fibers [26-28]. A pair of small mirrors for *xy*-scanning similar to scanning system employed in most conventional bulk optic laser scanning microscopes are attached at the end of fiber to achieve laser beam scanning. Another type of scanning involves scanning the fiber tip. The tip of the fiber may be accurately scanned using piezoelectric elements [29]. In addition, the core of the fiber can act as an ideal pinhole. Therefore, microscopes based on SMF inherently

perform spatial filtering, such as in confocal microscopy, that blocks out-of-focus beams, as illustrated in Figure 2.10.
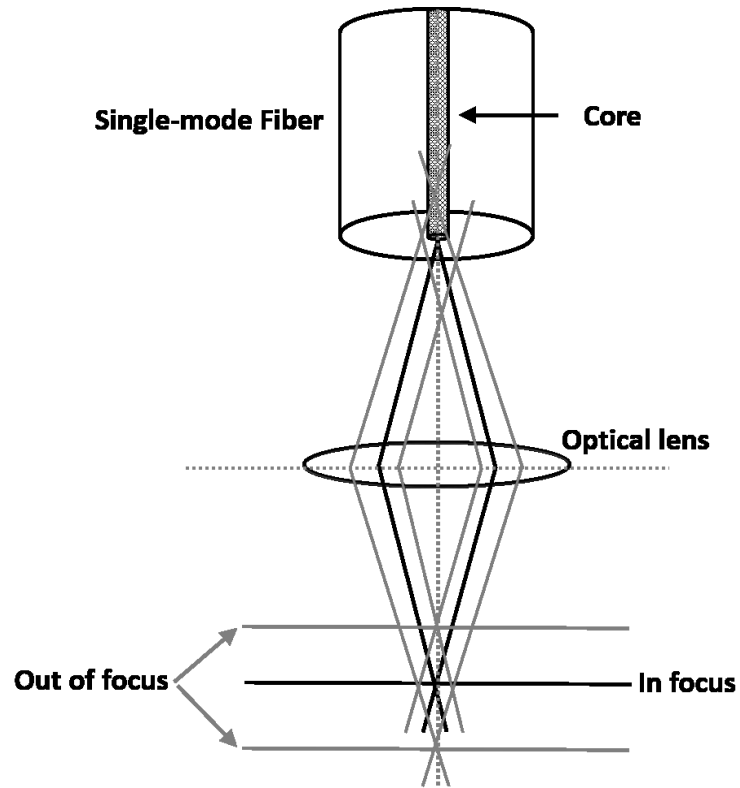
Figure 2.10. Confocal effects in single-mode fiber based microscopy.

The backscattered light from the specimen gets coupled into the fiber only if it is from the in-focus plane. The light from out-of-focus planes is effectively rejected by the SMF. Under the Gaussian approximation, the fiber spot size r_0 can be expressed, for an SMF with a step refractive-index profile, as

$$r_0 = \rho / (2 \ln V)^{1/2}, \, [30]$$

where ρ, the core radius of the fiber, is in the range of 2-5 μm and V is the fiber parameter. For an SMF, the maximum value of V is 2.592 so that r_0 is in the range of 1.6-4 μm.

2.3.2   Fiber bundle Microscopy

The most generally accepted method of fiber endoscopic imaging is through the use of a fiber bundle. Fiber bundles containing several tens of thousands of 10-50 μm diameter fiber cores are commercially available and widely used for medical and industrial applications. A fiber bundle can be used to transfer an image from a target location to another image plane on an optical system. An advantage of confocal laser scanning microscopes using a fiber bundle is that the actual scanning mechanism is placed at proximal facet of the fiber instead of the distal end. Thus, no scanner is needed at the distal end, which minimizes the probe size and allows easy applicability to various targets, such as hollow cavities. Such microscopes can operate in a contact mode in which the polished end of the fiber bundle defines the image-isolation plane by directly touching the imaging target. Alternatively, an appropriate imaging lens can be attached to the distal exit surface of the fiber bundle to allow demagnification. Unlike the SMF-based microscopes, in the case of fiber bundle-based microscopes all imaging pixels can be obtained in parallel.

2.3.2.1 Wide-field fiber bundle microscopy

Two-dimensional images can be obtained from a fiber bundle microscope using wide-field illumination and a two-dimensional array detector (CCD or CMOS camera), as shown in Figure 2.11.
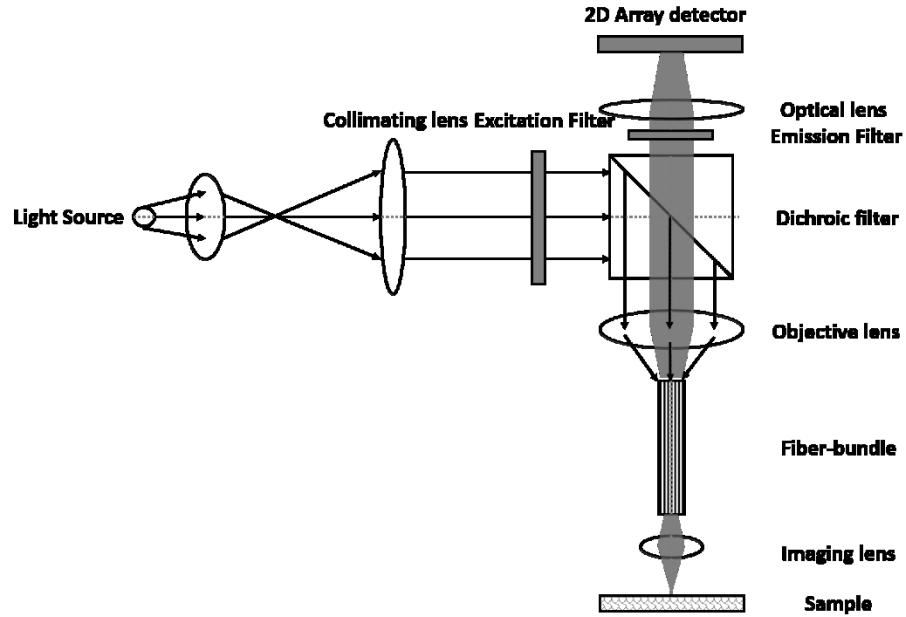
Figure 2.11. Schematic of wide-field fiber bundle microscope.

For such wide-field illumination, it is desirable to use an extended light source with a low coherence, such as a thermal light source or light-emitting diode (LED) [31]. If a spatially coherent light source such as a laser is used to illuminate the fiber bundle, the cross-coupling between adjacent cores in the fiber bundle can introduce strong cross-talk and undesired interference patterns [18]. A wide-field microscope operating in this mode cannot differentiate photons from different axial planes and does not exhibit a confocal effect.

Figure 2.11 illustrates its configuration. The target is imaged at the distal facet of the fiber bundle. The image is then sampled by the fiber cores, which serve as an image conduit to transport the image to the proximal facet of the fiber bundle. To preserve the diffraction-limited lateral resolution, the image of the target on the fiber bundle facet has to be sampled by the fiber cores at a frequency greater than twice its highest spatial frequency; otherwise, the lateral resolution is limited simply by the core size and pitch of

the fiber bundle. Moreover, when the proximal facet of the fiber bundle is imaged by the camera sensor plane, the two-dimensional pixel array of the camera has to sample the proximal facet of the fiber bundle at least twice the frequency of the highest spatial frequency of the fiber bundle core; otherwise, the aliasing artifact can smear the image.

2.3.2.2 Confocal laser scanning fiber bundle microscopy

Two-dimensional images can be obtained from a fiber bundle microscope by scanning a point light source with a two-dimensional mechanical scanner such as a Galvo mirror, as shown in Figure 2.12.
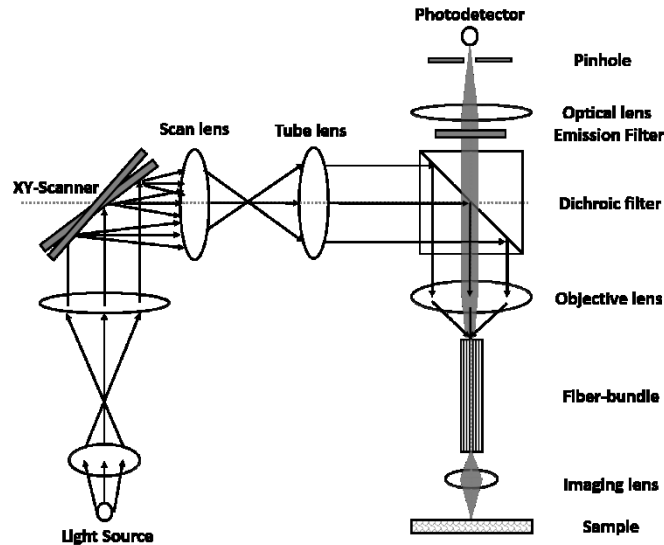
Figure 2.12. Schematic of confocal laser scanning fiber bundle microscope.

Since the image is obtained pixel-by-pixel, cross-talk between adjacent cores in the fiber bundle is no longer a problem and a laser source with high spatial coherence can be used to achieve high coupling efficiency. The confocal effect of the laser-scanning fiber bundle microscope is schematically presented in Figure 2.13, which shows that photons from the in-focus plane couple into a single core of the fiber bundle, while photons from the out-of-

focus plane couple into multiple cores of the fiber bundle. For both cases, the signals are guided by the fiber core (or cores) from the distal end to the proximal end. The small pinhole in front of the detector that is in conjugate with the probing light spot is used to effectively reject the signal from out-of-focus planes guided by the multiple fiber cores; therefore, the resolution of laser-scanning fiber bundle microscopy can be comparable to that of SMF-based confocal microscopy. However, the lateral resolution cannot be described as $0.4\lambda / NA$ in a conventional confocal microscope because the image of the object is pixelated by the fibers. The lateral resolution cannot be better than the separation between two spots that are illuminated by two adjacent fibers [32].
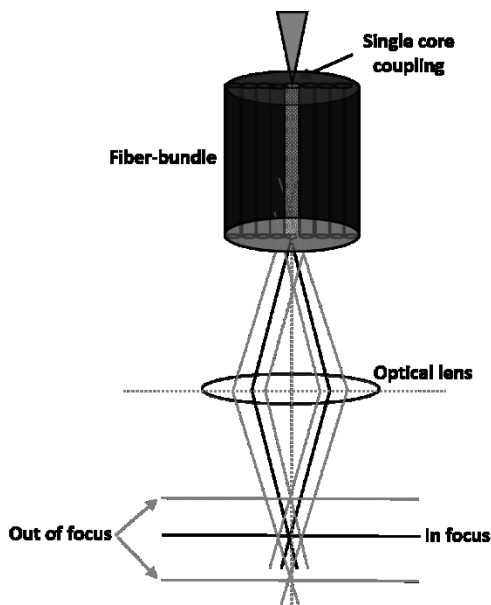
Figure 2.13. Confocal effects in laser scanning fiber bundle microscopy.

2.3.2.3 Cladding effects and optical efficiency of fiber bundle

The cores of fiber bundles transmit light, but they are surrounded by shared common cladding layers. Thus, some light must fall onto the cladding rather than the cores. Most light entering the cladding is lost, which can limit transmission efficiency [28].

23

As with any fiber-based imaging system involving illumination and detection via the same fiber, end-face reflections and auto-fluorescence from the fibers or associated packaging may give rise to additional background signals. As with single-fiber microscope systems, these reflections may be minimized using refractive index matching [32]. Alternatively, this may be achieved by first using a high degree of over-sampling to properly capture the fine structure of the pattern, and then subtracting the fluorescence pattern of the fiber bundle from the raw target data sets [28].

CHAPTER 3: DESIGN AND EVALUATION OF FIBER BUNDLE IMAGERS

3.1   Background and Overview

There have been many types of fiber-optic imaging systems that include endoscopic systems based on fiber bundles. In this chapter, several high-resolution endoscopic imagers based on fiber bundles are presented. These fiber imagers are designed specifically for high-resolution cellular imaging.

Recent fiber-optic technologies have led to the development of several novel sub-cellular imaging methods *in vivo* [33]. A number of groups have developed flexible confocal endoscopes that can image *in vivo* based on high-resolution fiber bundles [34-36]. In addition, a commercial confocal microendoscope device (Cellvizio, France) that can acquire high-resolution real-time images of various tissues (e.g., esophagus, bile duct, and colon) via the instrument channel of an endoscope has been commercially available for several years [37-39]. Nevertheless, these systems function either as confocal reflectance or fluorescence microscopes, making it difficult to register both fluorescing and entire cells simultaneously. In section 3.2, a dual-modality microendoscope system is presented, which can simultaneously register both fluorescing and entire cells for label-free optical assessment of intracellular gene delivery. The system uses two separate detection systems, enabling both high resolution reflectance and fluorescence imaging at the same time. The system then identifies and counts the cells from both images; therefore, gene transfection efficacy can be automatically calculated by the ratio of cell counts from both images.

Section 3.3 illustrates a single ball-lens integrated imaging probe design and applications to endoscopic brain imaging. Previous research has used a bare fiber bundle-

based imaging platform to record intrinsic fluorescence changes in contact with brain tissues [40, 41]. Although these studies suggested the feasibility that fiber bundle imaging could be used for extracting spatiotemporal brain activity in live animals, bare fiber bundles without any focusing elements have limitation, where the output beam diverges right after it has been launched from the fiber tip [42]. This diverging characteristic not only results in low spatial resolution limited by the size of the core of the fiber bundle, but also the working distance is directly in contact with the target tissues. Therefore, the distal end of the fiber bundle should be at a very close distance to have an appropriate level of SNR, but may damage the intact tissues [43]. To tackle this issue, there have been several interesting studies that include the idea of incorporating small lenses at the distal end of fiber bundle [10, 44-46]. GRIN lens probes are typically used for deep brain imaging [47, 48]. In this section, the design of a single ball lens-integrated fiber bundle imaging probe is presented, which can be used to achieve a longer working distance with a finer lateral resolution for continuous monitoring of brain activity in live mice. One of the main advantages, over the GRIN lens probes, is in that it enables to control the magnifications of the sample imaging by changing the working and coupling distances of the ball-lens in a stainless steel tube without any further optical elements. Two types of imaging probes are presented. The first, which is designed for deep brain imaging, uses a ball lens of 500-μm diameter and a highly flexible 350-μm fiber bundle that are encased by a 21G stainless steel sheath. The second probe, using a 1-mm-diameter sapphire ball lens, is fabricated for imaging intrinsic fluorescence from the cerebral cortex. These probes are both evaluated through *in vivo* brain imaging in live mice.

Finally, in section 3.4, a spatially multiplexed fiber bundle imager is proposed and demonstrated to permit simultaneous recording and perturbation of multiple brain regions. Although conventional bench-top microscopes have been used for a single region imaging of biological samples at a time, monitoring and controlling concurrent cellular events from multiple brain regions is yet to be established [49, 50]. Spatial multiplexing is one of the well-known fiber-optic sensing techniques, which isolates the optical fiber paths for each sensor to clearly address distinct systems while maintaining the return-signal integrity [51]. This can be achieved by the arrangement of individual optical links from the source to individual point sensors in the network, which then feed into the detection system. Several research groups have utilized this technique for large-scale optical sensing and networks [52]. Such a simple technique can be applied to fiber bundle imagers and may have unique advantages over the traditional bulk-optic imaging systems. In this section, flexible photostimulation with diverse beam patterns and synchronous imaging of three different brain tissue regions is demonstrated.

3.2   Dual-mode Laser Scanning Confocal Reflectance/Fluorescence Fiber bundle Imager for Gene Transfection Efficacy Assessment

In this section, a dual-modality microendoscope system registers simultaneously both fluorescing and entire cells for label-free optical assessment of intracellular gene delivery. The system uses two separate detection systems, enabling both high resolution reflectance and fluorescence imaging at the same time. The system then identifies and counts the cells from both images; therefore, gene transfection efficacy can be automatically calculated by the ratio of cell counts from both images.

3.2.1   Methods

3.2.1.1 System design
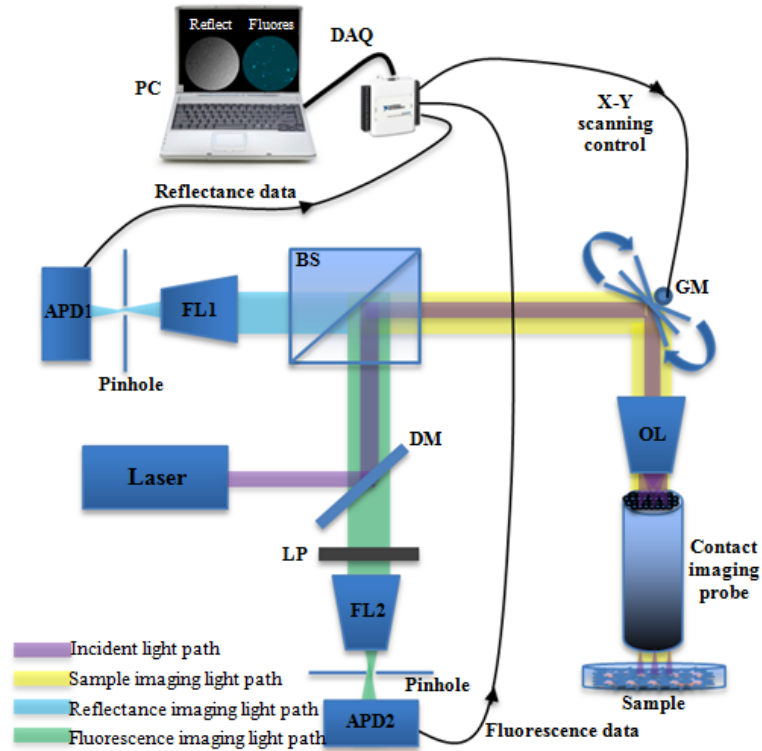
Figure 3.1. System configuration (GM: galvo mirror, DM: dichroic mirror, BS: 50:50 beam splitter, OL: objective lens, FL 1&2: focusing lens, LP: longpass filter, APD 1&2: avalanche photodetector, DAQ: digital-to-analog & analog-to-digital converter).

A schematic of the imaging system is illustrated in Figure. 3.1. The laser scanning

confocal microscope is connected to a coherent fiber bundle imaging probe [53]. Incident

light from a 4-mW, 405-nm blue laser with beam diameter 3.0 mm × 5.0 mm (LDM 405,

Thorlabs) is reflected by a dichroic mirror (DMLP425R, Thorlabs), a 50:50 beam splitter

(BS013, Thorlabs), and an X-Y galvo scanner (GVS002, Thorlabs) in series and coupled

into a multi-core fiber bundle by a microscope objective lens (Plan 20X/0.4, Olympus).

The imaging probe is a coherent fiber bundle (FIGH-10-500N, Fujikura) and consists of

10,000 fiber cores with an image diameter of 460 µm. Returning light from the specimen is divided into two pathways by the beam splitter. One pathway, which is used for the reflectance imaging (colored blue in Figure. 3.1), is directed through the beam splitter and spatially filtered using a focusing lens (FL1) (Plan N 10X/0.25, Olympus) and a 100-µm pinhole to reject background and out-of-focus light. An avalanche photodetector (APD1) (APD110A, Thorlabs), a highly sensitive Si avalanche photodiode, with an active area diameter of 1 mm^2, is used to detect the reflectance imaging light. The second pathway, which is used for the fluorescence imaging (colored green in Figure. 3.1), gets reflected by the beam splitter, transmitted through the dichroic mirror, and then filtered by a longpass filter (452 nm cut-off, Thorlabs) to obtain only the fluorescence signal. Similar to the reflectance imaging path, the longpass filtered beam is spatially filtered using a focusing lens (FL2) (Plan N 10X/0.25, Olympus) and a 100-µm pinhole. The resulting fluorescence signals are detected by APD 2 (APD110A2, Thorlabs), which is a UV-enhanced Si avalanche photodiode.

Data from the two detectors are acquired simultaneously using a DAQ board (NI USB-6211, National Instruments) with a sampling rate of 250 ks/s at 16-bit resolution. Two analog output channels of the DAQ are used to control X-Y scanner mirrors. The graphical user interface, control software, and automated cell-counting algorithm are programmed using LabVIEW 2011 (National Instruments).
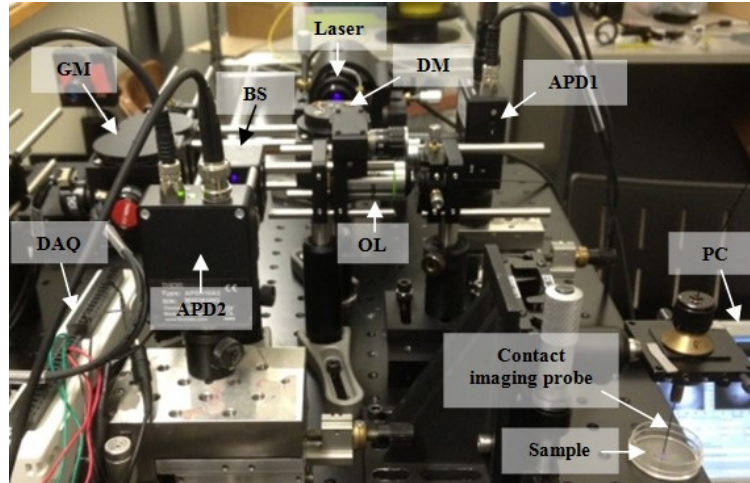
Figure 3.2. Photograph of the system implementation.

3.2.1.2 Cell culture and preparation of transfection systems

HeLa cells were seeded onto 35-mm culture dishes (24 × 104 cells/ml) and allowed to

adhere for 24 h under standard tissue culture conditions the day before the transfection.

The diluted 1.5 µg cyan fluorescent protein (CFP) plasmid DNA was mixed with 3.0 µl

of four different transfection reagents (FuGENE 6, Lipofectamine 2000, Ultra, and X-

tremeGENE HP) according to the manufacturers' instructions. The solutions were mixed

and incubated for the appropriate time to allow formation of complexes. Finally, all the

transfection complexes were transferred into the culture dish. All samples were fixed

with 4% paraformaldehyde 24 h after transfection.

3.2.1.3 Sample imaging and image analysis

A U.S. Air Force resolution target was used to assess the system resolution. The system

has a maximum circular field of view 460 µm in diameter; the lateral resolution is

approximately 3.5 µm (Figure. 3.3,) and images are displayed at 1 Hz with an image size

of 250 × 250 pixels. The image size and scanning rate are limited by the hardware

performance since the scanner has a maximum bandwidth of 250 Hz, but it could be

further improved by replacement of the hardware with alternatives that meet the

requirement of high-rate scanning operations [32].
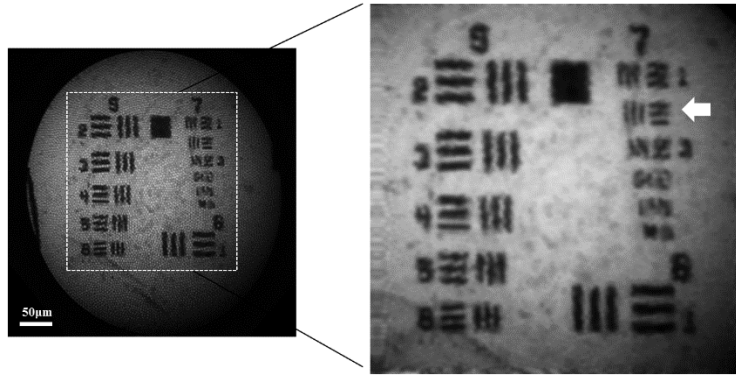
Figure 3.3. USAF target image (raw data [left], processed data [right]; group 7 element 2–resolution 3.48 μm).

HeLa cell sample imaging in each of the reagent-induced transfection systems was

conducted using both the presented system and a high-resolution bench-top fluorescence

microscope (ECLIPSE TE2000-U, 20X/0.45, Nikon) for comparison. For the reflectance

imaging of the microendoscope system, a reference image without the sample was used

to subtract background due to the Fresnel reflection from the proximal end of the imaging

probe [54]. The distal tip of the imaging probe was dipped into the culture dish and was

nearly in contact with the sample. The 16-bit gray scale digital images were saved,

processed, and analyzed. For each of the transfection systems, five images were taken

from randomly selected sites around the culture dish to count the average number of cells

in the way that a conventional hemocytometer operates [55].

An automated image analysis is implemented using MATLAB 2010a (MathWorks) to

assess CFP expression in each of the transfection systems. The automated image

processing algorithm performed the following procedures: (1) original data were contrast-enhanced by histogram equalization; (2) spatial pixelation effects of the imaging probe were removed by applying Gaussian blurring (sigma equals to the core-to-core distance of 4.5 μm) [44]; (3) gray-thresholding was applied and the image went through an edge detector. Morphological operators of opening and closing, and a labeling function provided by MATLAB were used to identify the spatial regions correlated to cells. By labeling segmented cells, the total number of cells (T) were marked and counted, and the number of fluorescence-expressing cells (F) were also counted from the images (see Figures 3.4 and 3.5). The ratio between the total and the number of fluorescence-expressing cells was used to determine how many cells were transfected by each of the vector systems.

3.2.1.4 Statistical analysis

Data were expressed as mean CFP expression percentages with standard error of five sites in different regions of the culture dish. One-way analysis of variance (ANOVA) was applied to determine the significance of differences among reagent groups; p values less than 0.05 were considered significant. For comparison of the results between the dual-modality microendoscope and the bench-top microscope, significance was determined by a Student's 2-sample t test, $p<0.05$ (OriginPro 8, OriginLab).

3.2.2 Experimental Results

3.2.2.1 Dual-modality microendoscope sample imaging

Five random sites sample imaging in different transfection reagent groups were performed using our dual-modality microendoscope system. Representative imaging

results are shown in Figure 3.4. For the reflectance imaging, individual HeLa cells are

distinguishable (Figure 3.4(a)) and countable, as registered by the white X-marks in the

middle of each cell (Figure 3.4(b)). The negative control (untransfected cells) shows the

largest cell population among the groups; FuGENE 6 and X-tremeGENE HP have

relatively high cell populations, whereas Lipofectamine 2000 and Ultra have the lowest.

In contrast, in the outer parts of the fluorescence imaging, the control group displays no

fluorescence signals compared to other reagents groups (Figure 3.4(c)). The fluorescent

cells appear blurred with flares due to the inter-core cross-talk between adjacent fibers

[18] , but can be clearly segmented. Fluorescent cells are also X-marked with red color

and counted in the same way (Figure 3.4(d)).
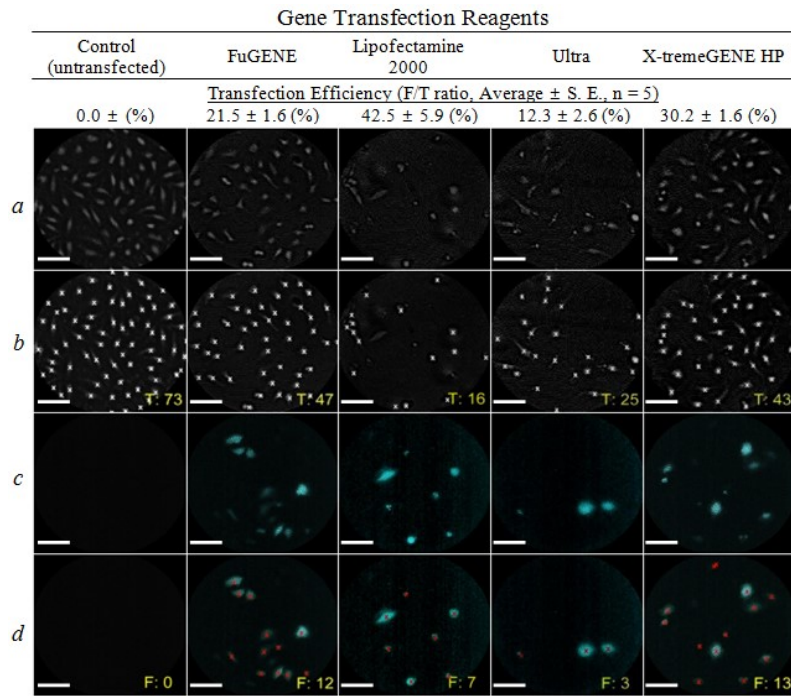
Figure 3.4. Representative dual-modality microendoscope sample imaging results in four different reagent groups: a. reflectance image, b. total cell counting from the reflectance image, c. fluorescence image, d. fluorescent cell counting from the fluorescence image (All white bars – 100 µm, T: total cell counting number, F: fluorescent cell counting number, pseudo-color applied on the fluorescence images).

As represented in the top of Figure 3.4, the Lipofectamine 2000 transfection reagent promoted maximal gene transfection efficiency (F/T ratio) in HeLa cells (42.5 ± 5.9%) compared to the other three reagents. X-tremeGENE HP resulted in the second highest (30.2 ± 1.6%). The difference in CFP expression between using Lipofectamine 2000 and X-tremeGENE HP was significant ($p<0.05$). FuGENE 6 was third in CFP expression (21.5 ± 1.6%; $p<0.05$), and Ultra contributed to the lowest gene transfection (12.3 ± 6.3%; $p<0.05$).

3.2.2.2 Bench-top microscope imaging

For a comparison study, bench-top microscope imaging using the same samples was performed. Figure 3.5 illustrates representative sample imaging results. In the bright-field imaging, not only individual cells are visible, but the cell structures and even debris are also resolved (Figure 3.5(a)). The images were automatically processed using the same MATLAB program and the cells are indicated by green X-marks (Figure 3.5(b)). As expected, the negative control group shows the largest population while the Lipofectamine 2000 and Ultra reagent groups have the least. For the fluorescent cells, cell shapes are clearly visible with no distortion or flares (Figure 3.5(c)). Each cell is X-marked with red color (Figure 3.5(d)).
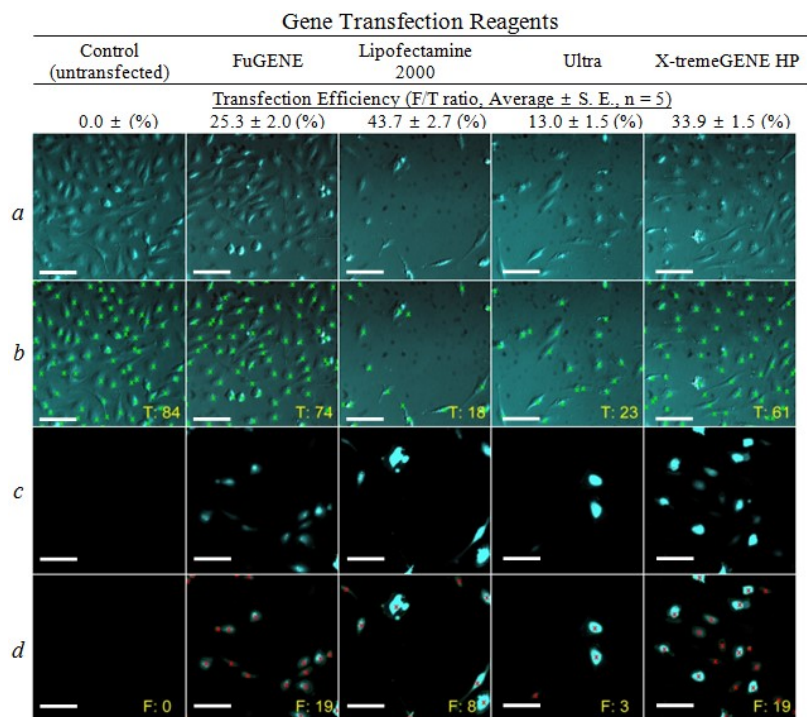
Figure 3.5. Representative bench-top microscope sample imaging results in four different reagent groups: a. bright-field illumination image, b. total cell counting from the bright-field illumination image, c. fluorescence image, d. fluorescent cell counting from the fluorescence image (All white bars – 100 μm, T: total cell counting number, F: fluorescent cell counting number, pseudo-color applied on fluorescence images).

Similarly, out of the four, the Lipofectamine 2000 transfection reagent promoted maximal transfection efficiency in HeLa Cells ($43.7 \pm 2.7\%$) compared to the other reagents (Figure 5); X-tremeGENE HP resulted in the second highest CFP expression ($33.9 \pm 1.5\%$). The difference in CFP expression between using Lipofectamine 2000 and X-tremeGENE HP was significant ($p < 0.05$). FuGENE 6 was third in CFP expression ($25.3 \pm 2.0\%$; $p < 0.05$) and Ultra contributed to the lowest gene transfection ($13.0 \pm 1.5\%$; $p < 0.05$).

3.2.2.3 Comparison between dual-modality microendoscope and bench-top microscope

By comparing Figures 3.4 and 3.5, it can be seen that the cell-counting algorithm produced consistent results for both the dual-modality microendoscope and the bench-top microscope images. The average transfection efficiencies obtained from the presented system tend to be lower than those from the bench-top system. This result originates from the relatively small numerical aperture of the imaging probe ($NA = 0.39$) compared to 0.45 in bench-top system; thus fluorescence collection efficiency in the former could be worse than in the latter. However, the resultant relative efficacies for all four reagents using both imaging systems were found to be highly consistent. A statistical comparison of the two sets of images was done; the results are illustrated in Figure 3.6. The bench-top microscope and dual-modality microendoscope results are clearly correlated with the *p*-value (<0.05) using a two-tailed Student's *t* test.
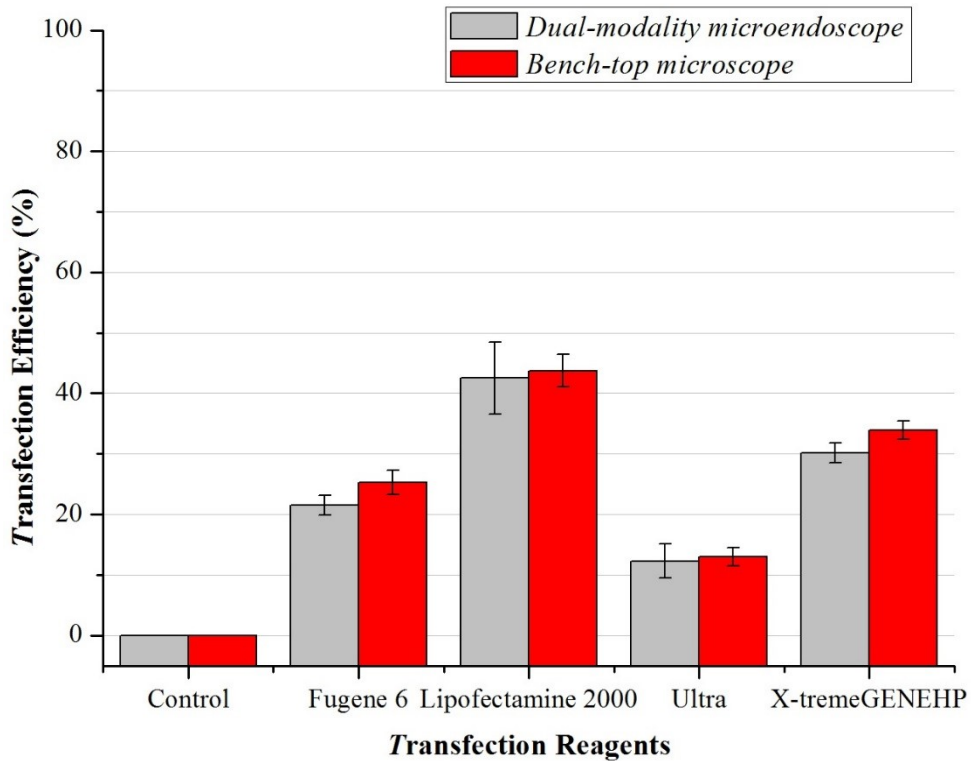
Figure 3.6. Comparison of transfection efficiency in the four reagent groups.

3.2.3 *Discussion*

Assessment of gene transfection efficacy in specific vector systems is essential in gene therapy studies. Optical imaging with flexibility, accessibility, and minimal invasiveness that provides such information can thus be useful in evaluating the efficacy of gene therapy. The dual-mode microendoscope system has proved capable of measuring the gene transfection efficiency by simultaneously monitoring high-resolution reflectance and fluorescence images of HeLa cells. Albeit the Gaussian degradation in the image processing algorithm was utilized to remove pixelation effects, individual cells were successfully identified and registered. This resulted from the sufficient signal-to-noise ratio accomplished by the imaging system.

In this study, approximately 3.5-µm lateral resolution was achieved, but limited by the core size (2.9 µm) of the imaging bundle. Even though the results proved the imaging performance adequate to obtain individual cell imaging, higher resolution is still needed to achieve sub-cellular imaging. Once the CFP plasmid is transferred to the cell, significant amounts of cyan fluorescent proteins are produced in ribosome and those are seen regionally throughout the cells. As depicted in Fig. 3.5, the bench-top microscope resolved the micro-organelles (i.e., nuclei) which contributed to the fluorescence signals. However, the system was not able to resolve sub-cellular organelles. A coherent fiber bundle with a smaller core-to-core spacing and a miniaturized objective lens (e.g., GRIN lens) assembly to the distal end of the imaging probe can be used to achieve higher resolution [36].

According to Lane et al. [36], it is still challenging to acquire high quality images during *in vivo* imaging because of movement of the imaging probe caused by motion artifacts such as heart beating and breathing of live animals. Further improvements of the imaging system include motion artifact reduction by the motion compensation technique, which has recently been developed in [56] and by an increase of imaging capability by applying highly sensitive detectors and high-speed equipment for real-time assessment.

3.3   Single Ball-Lens integrated Fiber bundle Imaging Probe for Endoscopic Fluorescence Imaging in Live Mice

In this section, a single ball lens-based fiber bundle imaging probe is demonstrated, which has better lateral resolution and a longer working distance than a corresponding bare fiber bundle for endoscopic fluorescence imaging. Two types of imaging probe, one for deep brain imaging and another for cortex imaging, are fabricated and evaluated through *in vivo* mice brain imaging.

3.3.1   Methods

3.3.1.1 Geometrical optics of the ball-lens
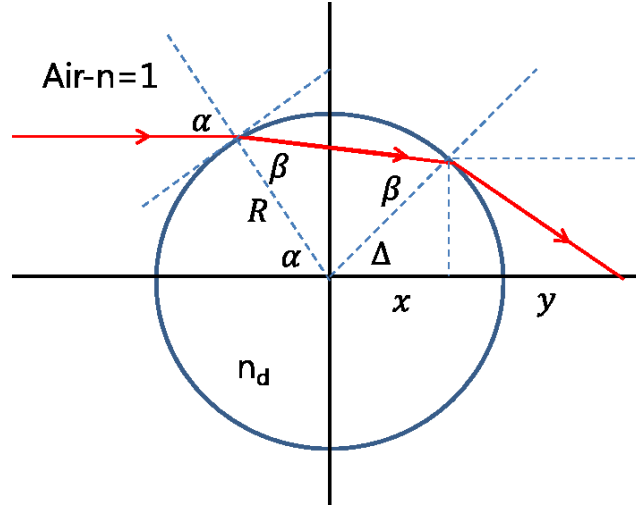
Figure 3.7. Ray tracing in a ball-lens.

Ray-tracing in a ball-lens is shown in Figure 3.7. The angle of exit is the same as the angle of entrance, and the ray inside the ball-lens follows a symmetrical path. Solid lines represent the ray path and the dotted lines are for measurement. The angle β is found from Snell's Law. The spherical geometry is expressed in the fact that the triangle in the circle is isosceles. Therefore the angle Δ in the figure is,

$$\Delta = \pi - [\alpha + (\pi - 2\beta)] = 2\beta - \alpha , \qquad (1)$$

Then, $x = R\cos(2\beta - \alpha), z = R\sin(2\beta - \alpha)$. The length y is determined from the angle of refraction out of the glass, which is α by Snell's Law; the angle of the right triangle of which y is a leg is $\alpha - \Delta$ (alternate interior angles). Thus, $\tan(\alpha - \Delta) = \tan(2\alpha - 2\beta) = z/y$, and

$$y = R\cos(2\alpha - 2\beta)\frac{\sin(2\beta - \alpha)}{\sin(2\alpha - 2\beta)} . \qquad (2)$$

Thus, the focal length f can be calculated as follows:

$$f = x + y = R[\cos(2\beta - \alpha) + \frac{\sin(2\beta - \alpha)}{\sin(2\alpha - 2\beta)}\cos(2\alpha - 2\beta)], \qquad (3)$$

where α is the angle of incidence from the air and β is the angle of refraction in the glass. Assuming the paraxial approximation in which the sines are replaced by their arguments and the cosine is replaced by 1, and using the paraxial form of Snell's Law: $n_d\beta = \alpha$, one can find that

$$f \approx R[1 + \frac{(2 - n_d)\alpha}{2(n_d - 1)\beta}] = \frac{n_d}{2(n_d - 1)}R. \qquad (4)$$
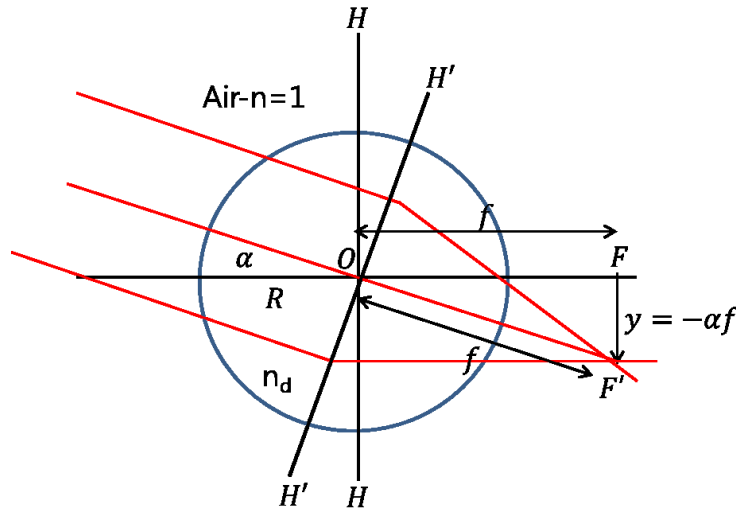
Figure 3.8. Paraxial ray construction.

The paraxial ray construction for the ball-lens is shown in Figure 3.8. The parallel incident rays have been drawn at an angle α with the axis. They come to a focus at the tip of the arrow. From the symmetry of the sphere, it is clear that $y = -\alpha f$, which also defines the focal length. The principal plane for axial rays is HH, and that for the rays at an angle α is $H'H'$. The incident rays are drawn up to this plane, and then are continued through the focal point F at a distance f from O. The focal plane of the sphere is curved, with a radius equal to f. By drawing rays either parallel to the axis or through the center, the image location for any object location can be found in the familiar way.
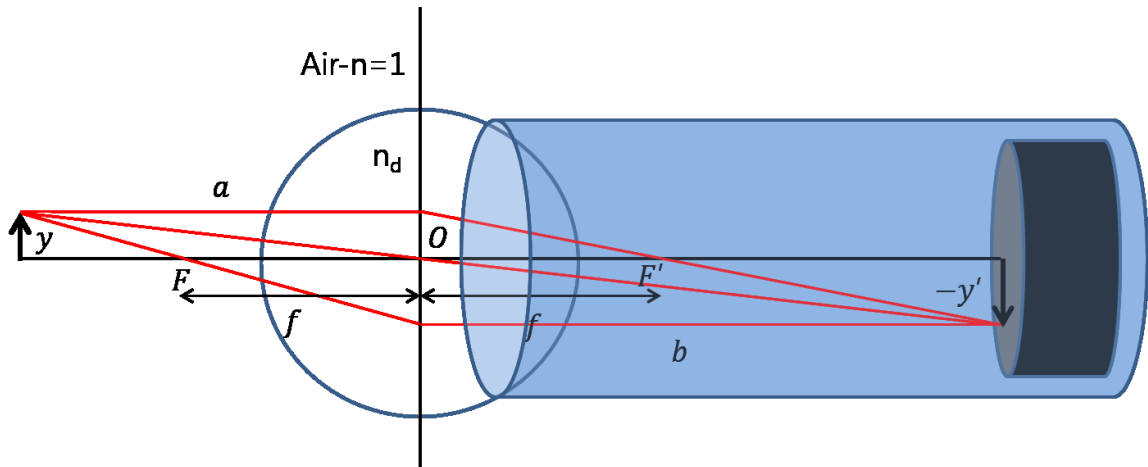
Figure 3.9. Gaussian lens formulas for the ball-lens.

With respect to paraxial optics, the ball-lens can be simply regarded as the thin lens. The Gaussian ray construction is shown in Figure 3.9, and is seen to be identical to that for a thin lens. Three rays that are easy to locate are drawn. One passes through the optical center, while the other two pass through the focal points. Only two of these rays are necessary to locate the image when an object is known. It is easy to find the expressions for linear magnification M from similar triangles, and eliminating y/y' between two of them one can find the Gaussian lens formula $1/a + 1/b = 1/f$. Object and image heights are positive upward, object and image distances a and b are positive as shown.

3.3.1.2 System setup and imaging probe design

The basic setup in principle is a fiber integrated epi-fluorescence microscope. As illustrated in Figure 3.10, a 10-mW, 473-nm diode-pumped solid-state laser (BWB-10-OEM, B&W Tek) served as the illumination light source, with the beam from the laser expanded and reflected by a beam expander and a dichroic mirror, respectively. The

41

reflected light is coupled into a multi-core fiber bundle as a wide-field illumination by a microscope objective lens (Plan N 10X/0.25 NA., Olympus).

For the deep brain imaging, the ball-lens imaging probe utilized a 500-μm-diameter sapphire ball-lens and a 10,000 core 350-μm-diameter fiber bundle (FIGH-10-350S, Fujikura), which are encased by a 21G stainless steel tube (OD: 0.82 mm, ID: 0.51 mm) as shown in Figure 3.10(c). A custom made one-end sealed glass capillary tube, called cannula, was prepared and implanted into the brain. The imaging probe is located inside the cannula using a 3-axis motorized micromanipulator [47].

For the cortical fluorescence imaging, a 1-mm-diameter sapphire ball-lens and 30,000 core 650-μm-diameter fiber bundle (FIGH-30-650S, Fujikura) that are encased by 18G stainless steel tube (OD: 1.27 mm, ID: 0.84 mm) were used, as depicted in Figure 3.11(a). The Zemax simulation result indicates that a spatial resolution of approximately 3-10 μm could be achieved with the working distance of 1.24 mm (Figure 3.11(b)). The USAF target and 4 μm fluorescent bead imaging results indicate that a 3.1 μm lateral resolution can be achieved with a 47.1 μm axial resolution. The returning light from the brain sample is collected by the same fiber and passes back through the same microscope objective lens, dichroic mirror, and emission filter. The resultant fluorescence signal is detected by a CCD camera (GS2-FW-14S5M, Point Grey Research).
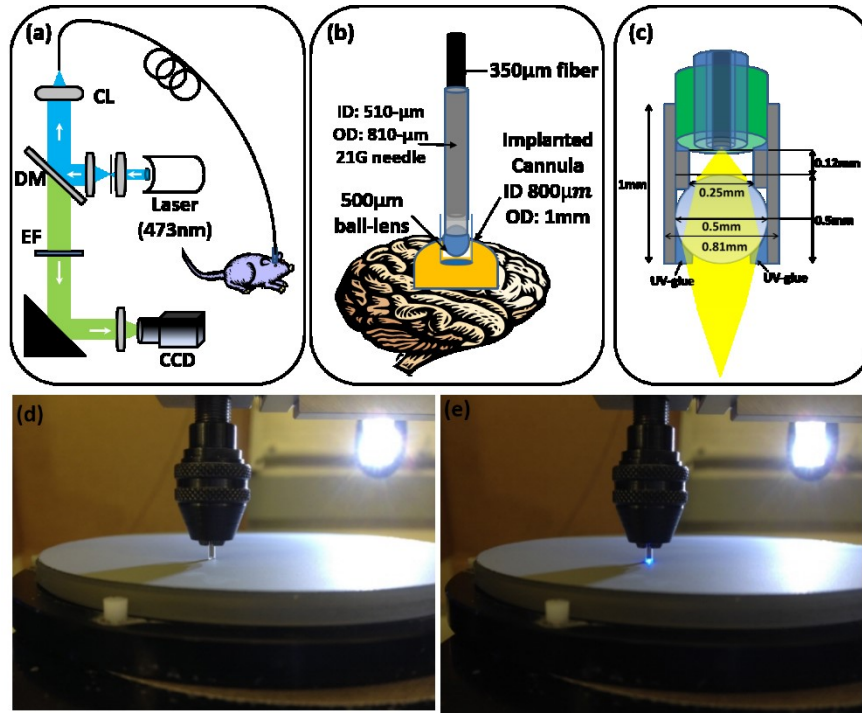
Figure 3.10. System setup and single 500-µm ball-lens imaging probe design. (a) System setup (DM: dichroic mirror, CL: condensing lens, EF: emission filter, RM: reflecting mirror). (b) Glass-capillary based implantation. (c) Deep brain imaging probe design. (d) Photo of prototype probe with one-end sealed cannula. (e) Photo of prototype with illumination light on.
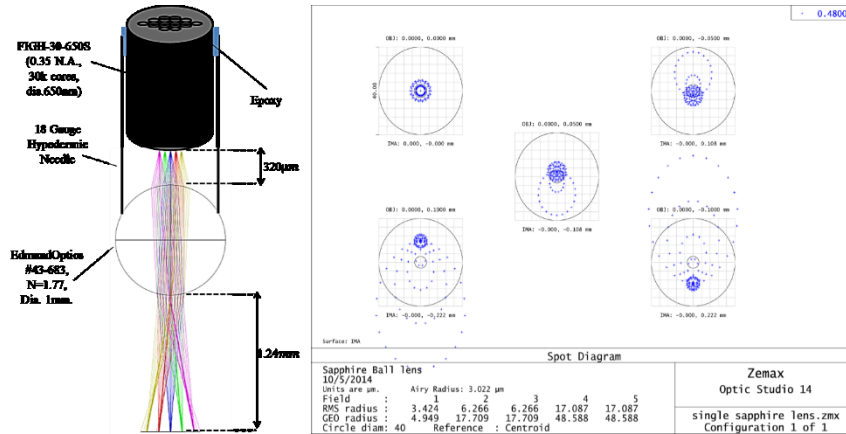
Figure 3.11. Single 1-mm sapphire ball-lens imaging probe design. (a) Imaging probe with specification. (b) Zemax simulation result at image plane.

43

3.3.1.3 Fixed brain sample imaging

The system performance was first evaluated through *in vitro* using a 50-µm thick

GCaMP3 immunostained mouse brain section and explored by *ex vivo* studies using a

transgenic mouse whole brain sample, which contains GFP cells throughout the brain.

The GCaMP3 targets were pyramidal neurons lying in the hippocampus, while the GFP

targets were the glial progenitor cells (NG2$^+$ cells) that are well known for generating

oligodendrocytes and repairing myelin [57]. For *ex vivo* studies, the sample was located

on a slide glass, and a small hole into the brain was made. The imaging probe was

positioned above the hole by 3 axis manipulator. The raw images were acquired at 30 fps

with an image size of 1280 × 960 pixels. The post image processing was applied using a

customized script in MATLAB 2013b (Mathworks) using the following procedures: (1)

background autofluorescence images were subtracted from the raw data; (2) subtracted

data were contrast enhanced by histogram equalization; (3) spatial pixelation effects of

the imaging probe were removed by applying Gaussian blurring; (4) pseudocolor (green)

was applied to visualize the green fluorescence signals.

3.3.1.4 In vivo mouse brain imaging and animal protocols

For the animal preparation, craniotomies were performed by the following steps. In the

first step, a custom designed stainless steel plate was attached to the skull for

immobilization of the head under a custom-designed head-fixation stage. In the second

step, the scalp incision was made and a small craniotomy was performed using a dental

drill with the stereotaxic apparatus. Mice were anaesthetized by i.p. injection of ketamine

(100 mg/kg) and xylazine (10 mg/kg). As soon as the animals were unconscious,

petroleum jelly was applied to the eyes. Bone was removed and replaced with a coverslip

(1 mm^2 in size, 100 µm thick). A No. 1 cover glass was placed on the dura mater and the

edges sealed with dental cement (Caulk Division, Dentsply International; Grip Cement).

After the surgery, the head of the animal was immobilized and imaging was initiated. The

laser power was adjusted up to 0.4 mW to prevent the intact brain tissue from damaging.

The tip of the imaging probe was positioned over the 1 mm^2 cranial window by

micromanipulators. The continuous duration of *in vivo* imaging never exceeded a

maximum of five minutes.
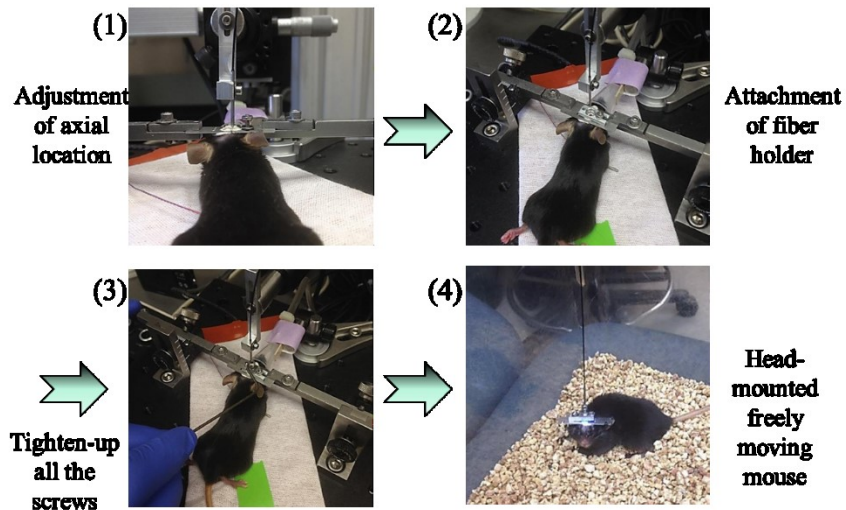
Figure 3.12. Animal preparations for integrating ball-lens imaging probe on mouse head.

3.3.2 Results and Discussion

3.3.2.1 Numerical calculations of 500 µm ball-lens probe with different materials

Simulations of two ball-lens types were performed to estimate the working distance and

coupling distance for the imaging probe. The sapphire ball-lens ($n = 1.77$) has the

effective focal length of 287 µm, while the N-BK7 ball-lens ($n = 1.517$) has the effective

focal length of 367 µm. Based on geometrical/paraxial ray-optics, the working distance

of $(M+1)f/M$ - 250 μm and coupling distance of $(M+1)f$ - 250 μm were obtained. Figure

3.13 shows the simulation results of the working distances as functions of magnification

(M) for the sapphire and N-BK7 ball-lenses. The results indicate that the working

distances at $M = 1$ in the sapphire and BK-7 ball lenses are 324 μm and 484 μm,

respectively. As the imaging fiber bundle has a limited numerical aperture, the ball-lens

NA, calculated as $2d(n-1)/nD$ (d: beam size, D: ball diameter, n: refractive index) should

be considered to yield better coupling efficiency with the fiber.
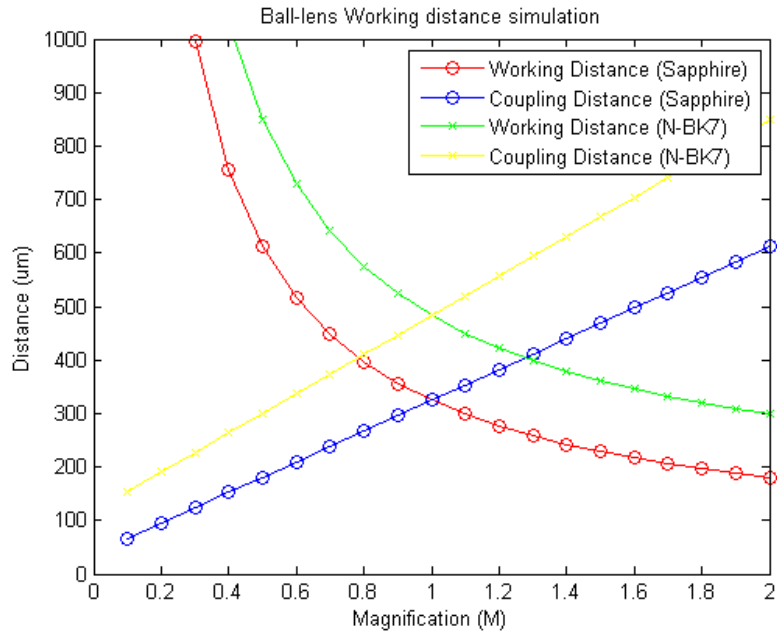
Figure 3.13. Working distance simulation results of a ball-lens with 500-μm diameter.

3.3.2.2 Fixed brain sample imaging

As shown in Figures 3.14 and 3.15, sapphire ball-lens-based imaging probes were

fabricated and the brain sample imaging studies were conducted using the prototype

probes. First, a 50-μm-thick brain slice was imaged, which contains GCaMP3

immunostained pyramidal neurons. The pyramidal neurons were clearly visible as

depicted in Figure 3.14(b). This imaging result is also compared to that from a bench-top

fluorescence microscope. Second, the probe was tested in *ex vivo* whole brain sample imaging. A one-end sealed glass capillary tube was inserted into a small hole and the deep imaging probe was lowered into the implanted capillary. As the NG2$^+$ cells contain GFPs, the fluorescent cell bodies and processes are visible in green. The imaging results are also compared to that from a bench-top fluorescence microscope. As the imaging field of view of the fiber is relatively small compared to that of the bench-top fluorescence microscope, a relatively small number of cells are visible.
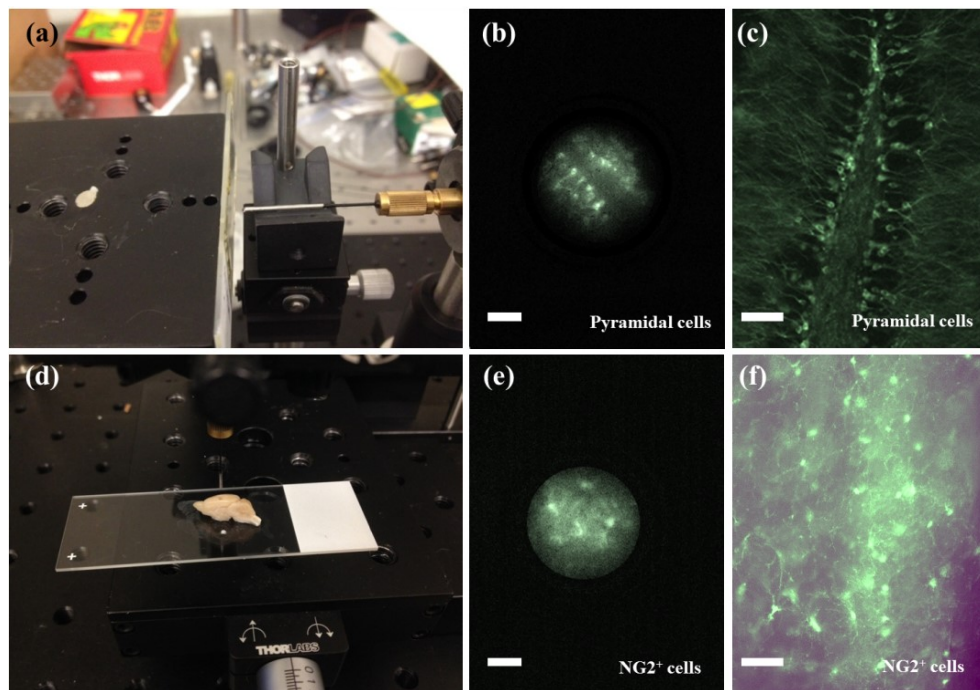
Figure 3.14. Fixed brain sample imaging results. (a) 50-µm-thick GCaMP3 immunostained brain section sample. (b) Pyramidal cells image obtained from fiber-optic imaging probe. (c) Pyramidal cells reference image obtained from conventional bench-top fluorescence microscope. (d) GFP tagged whole brain sample. (e) NG2$^+$ cells image obtained from fiber-optic imaging. (e) NG2$^+$ cells reference image obtained from conventional bench-top fluorescence microscope. (All the white bars: 100 µm).

Similar experiments were also performed using a 1-mm-diameter sapphire ball-lens imaging probe and the fluorescence images were obtained from the same samples as shown in Figure 3.15. The imaging results were compared with those from bench-top microscope imaging.
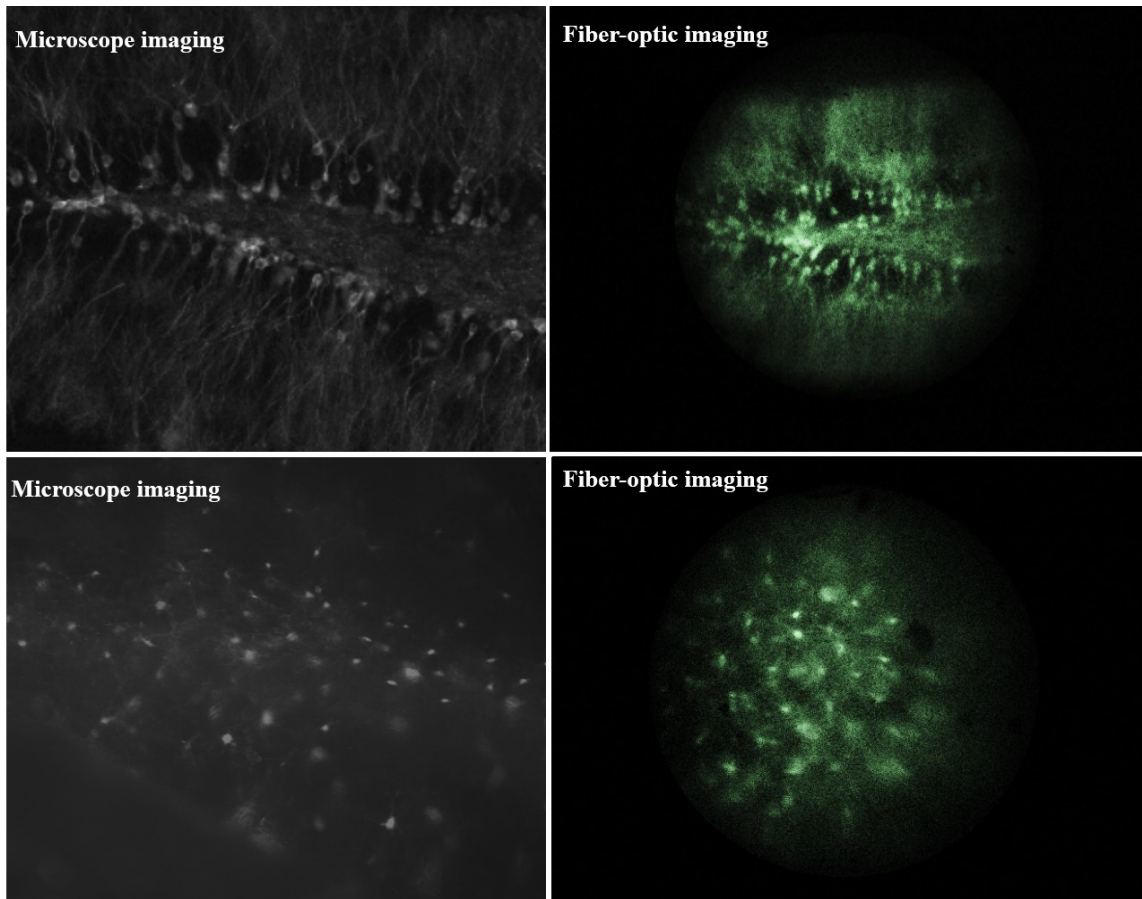
Figure 3.15. Fixed brain sample imaging results using sapphire ball-lens imaging probe with 1-mm diameter.

3.3.2.3 In vivo live mice brain imaging
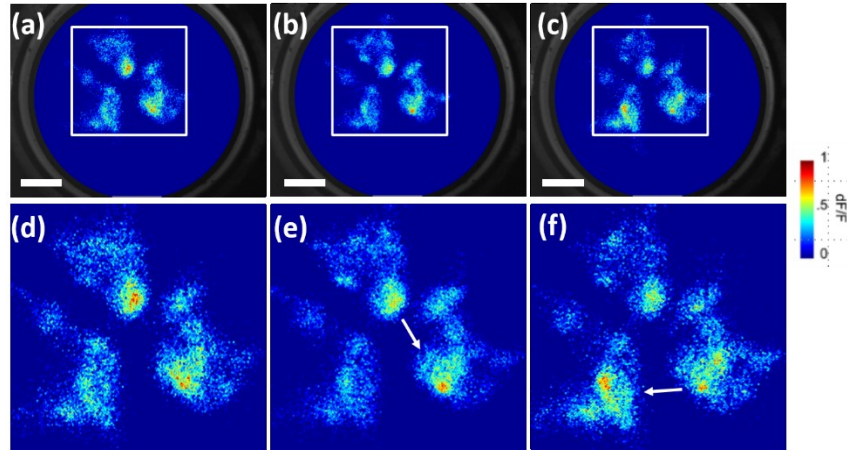
Figure 3.16. (a)-(c) Time-lapse astrocytes calcium imaging in primary visual cortex of the head-fixed transgenic mouse brain. (d)-(f) Enlarged view of (a)-(c). All bars: 100 μm.

In vivo validation was first performed using a head-fixed transgenic mouse, which expresses a genetically encoded calcium indicator (GCaMP3) within astrocytes. When the animal was startled by an air-puff stimulus, astrocytic calcium transients in the primary visual cortex (V1) region were observed, as shown in Figure 3.16. As one can see from the figure, the calcium transients started from one cell and then calcium waves were transferred to other cells. The imaging probe successfully resolved cellular activities and captured the sequential propagations of calcium waves.
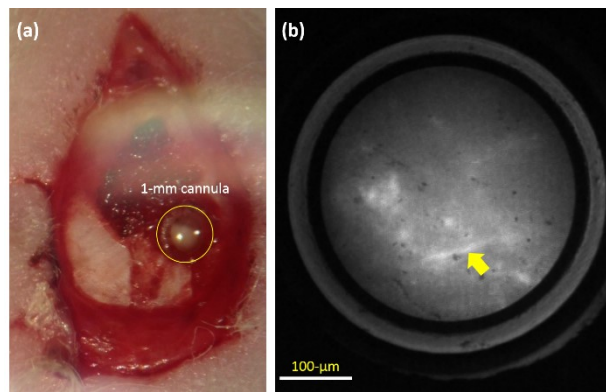
Figure 3.17. Fluorescein dye injected blood vessel imaging 1 mm deep inside the brain.

Deep brain imaging was tested using 500μm Sapphire ball-lens imaging probe. A 1-mm one-end sealed cannula was implanted in the mouse brain and secured for 10 days to get recovered. To test the feasibility, fluorescein dextran conjugate dye was injected via tail vein and the imaging probe was located inside the cannula by a motorized manipulator. The imaging result is shown in Figure 3.17. During the recording, the flow of red blood cells was visible (not shown in the figure).

The 1 mm sapphire Ball-lens imaging probe was finally integrated into a freely moving mouse and used to visualize cerebral microcirculation and red blood cell dynamics (Figure 3.18.) The flow of red blood cells is tested by mouse tail intravenous fluorescein dye injection into the blood stream. This provided a contrast of blood plasma and red blood cells, displaying dark cells on bright background. In capillaries, individual red blood cells were clearly visible and captured in real-time.
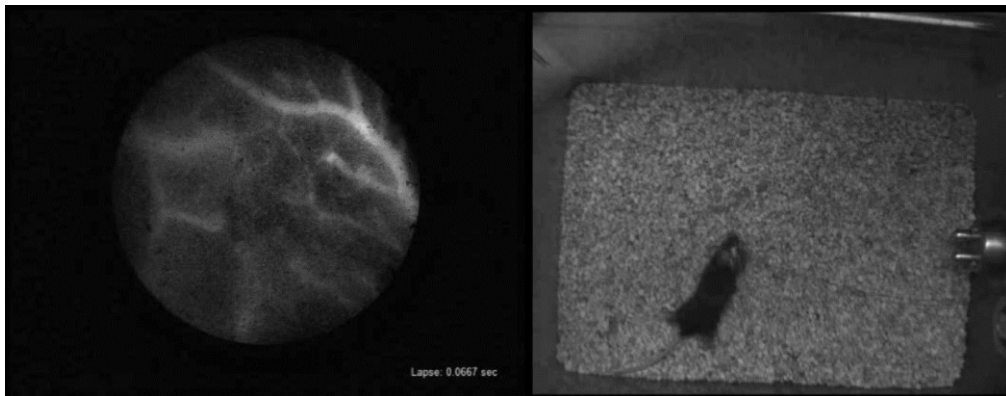
Figure 3.18. Cerebral microcirculation imaging in freely moving mice.
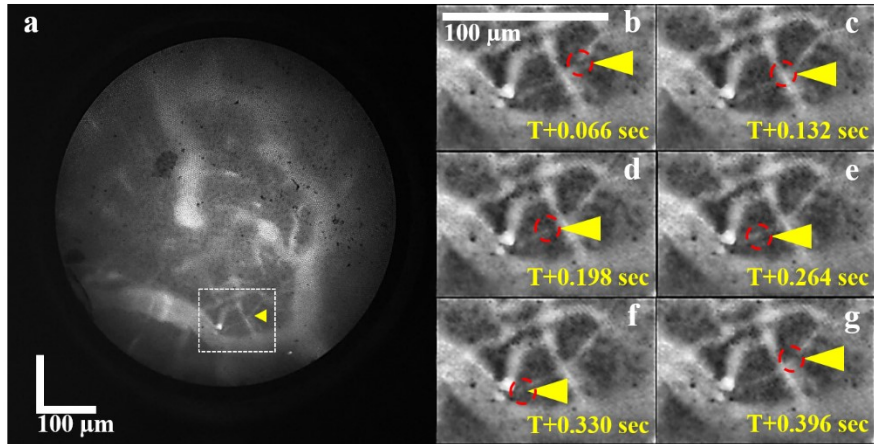
Figure 3.19. Movie frames of single red blood cell dynamics visualized in vivo using the developed ball-lens imaging probe.

As depicted in Figure 3.19, a time-lapse tracking of red blood cell is demonstrated. As the size of red blood cells in the rodent model is 7-8 µm, the 1 mm sapphire ball-lens imaging probe resolved individual red blood cells and the system visualized the blood flow dynamics in freely moving animals.

3.3.3 Discussion

In this work, a single ball-lens integrated fiber bundle imaging probe is demonstrated. This system allows repeated attachment of the fiber probe that enables longitudinal studies to relate brain activity and animal behaviors. Future work will focus on the application of the probe to the brain activity monitoring in freely behaving mice and the correlation analysis between brain function and specific animal behaviors.

One of the issues encountered in deep brain imaging is that the implanting cannula approach was invasive and might affect brain function and/or damage tissues. In addition, due to the motion artifacts such as breathing and heart beating, stable imaging

with tight focusing was difficult. This problem can be solved using head-fixation or head-mounted deep brain imaging.

For side-viewing capability, a 45˚ prism can be attached to the imaging probe that will allow volume imaging across the implanted cannula, as introduced by [48].

3.4 Spatially Multiplexed Fiber bundle Imager for Simultaneous Imaging and Optical Manipulation of Multiple Brain Regions

In this section, a spatially multiplexed fiber-optic spatial light modulator (SLM) microscopy system for simultaneous cellular imaging and spatio-temporal photostimulation of multiple brain regions is proposed. System feasibility is demonstrated via simultaneous imaging of multiple brain regions and a single wavelength photostimulation. The system utilizes a tri-furcated fiber bundle for three regions of interest (ROIs) multiplexing and a DMD for patterned illumination. The feasibility of the proposed system is assessed via *in vitro* studies using transgenic mouse brain cells expressing a genetically encoded calcium indicator (GCaMP3).

3.4.1 *Methods*

"Spatially Multiplexed Fiber-optic Microscopy," which utilizes a DMD as an SLM and a multi-furcated fiber bundle imager, enables both imaging and stimulating tissues in multiple brain regions. Two lasers of wavelength 488 nm and 532 nm are simultaneously used for photostimulating and imaging cells within a tri-furcated fiber bundle of 650-μm diameter [49, 50]. The DMD permits programmable patterned illumination with millisecond temporal resolution and a single CCD camera is used for three spatially multiplexed imaging of triple sites on the proximal end of the tri-furcated fiber bundles.

As illustrated in Figure 3.20(a), for the photostimulation mode, incident light from a 50-mW, 488-nm laser (OBIS488LX50, Coherent Inc.) is reflected by a DMD (DLP300 LightCrafter, Texas Instruments), passes through a scanning/tube lens pair, is reflected by a dichroic mirror (MD499, Thorlabs), and coupled into a tri-furcated 30,000 core fiber bundle (FIGH-30-650S, Fujikura) by a microscope objective (Plan 10X/0.25, Olympus). For the imaging mode, a high-power 532 nm laser beam is expanded, passes through a beam splitter and the dichroic mirror, and is then coupled into the fibers by the same objective lens. The distal end of the fibers is encased by a 1 mm achromatic dual-lens pair (#65-564, Edmund Optics) and an 18G stainless steel sheath to form a miniature objective. The returning fluorescent light from the sample passes back through the same fibers and objective before being reflected by the beam splitter and filtered by an emission filter (600/40 nm). Spectrally filtered 640×480 pixel size images are acquired at 30 fps by a CCD (FL2-O3S2M, Point Grey Research). The graphical user interface, data acquisition and control software are programmed using visual C# (Visual Studio 2010, Microsoft).
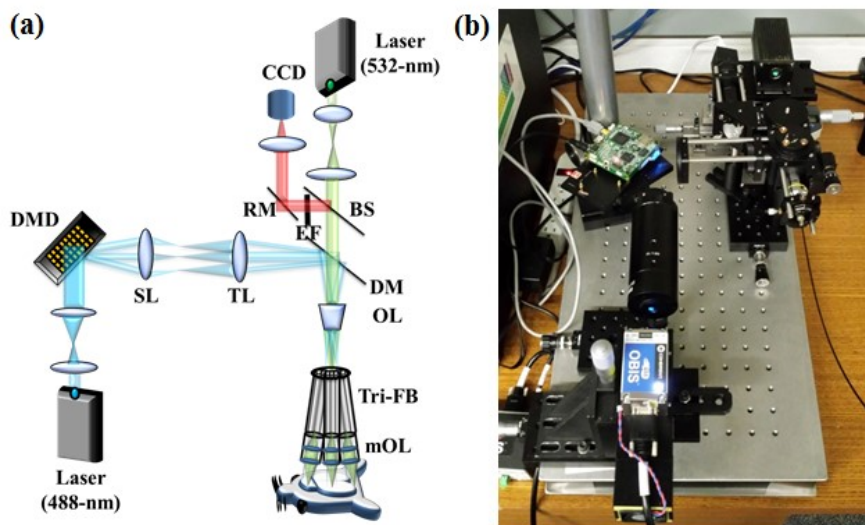
Figure 3.20. System configuration. (a) Schematic of the spatially multiplexed fiber-optic SLM microscope (DMD: digital micromirror device, SL: scanning lens, TL: tube lens, DM: dichroic mirror, OL: objective lens, Tri-FB: tri-furcated fiber bundle, mOL: miniature objective lens, BS: 50:50 beam splitter, EF: emission filter, RM: reflective mirror). (b) Picture of the system implementation.

3.4.2 Experimental Results

Operation of photostimulation was tested in multiple regions using a VIS/NIR detector card (VRC2, Thorlabs), which reflected fluorescence ranges from 400 to 640 nm. Patterned beam sequences generated by a DMD were illuminated through the fibers in series and the emitted fluorescence images were captured by the CCD camera. As depicted in Figures 3.21(a)-(c), a single beam spot moves from one fiber to another. In contrast to laser scanning microscopes, SLM microscopes allow simultaneous illumination of multiple regions. Figure 3.21(d) clearly shows that three beam spots on each of the three fibers can be excited at the same time. This shows the main advantage of using a DMD for optical manipulation: it can simultaneously photostimulate multiple targets. In addition, checkerboard patterns (or grid patterns) were also tested to demonstrate the capability of multi-cellular photostimulation. Various beam sizes were generated and illuminated from one fiber to another. Figure 3.21(h) demonstrates that our system allows a multi-spot photostimulation in multiple regions at the same time. For optogenetics applications, our system makes it possible to manipulate multiple brain cells on different brain areas concurrently.
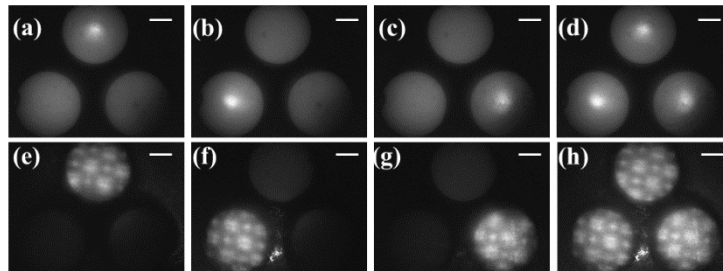
Figure 3.21. Photostimulation test results on laser viewing card. (a) Single fluorescent beam spot imaged on the first fiber. (b) Single fluorescent beam spot imaged on the second fiber. (c) Single fluorescent beam spot imaged on the third fiber. (d) Concurrent fluorescent beam spots on all fibers. (e) Multiple fluorescent beam spots imaged on the first fiber. (f) Multiple fluorescent beam spots imaged on the second fiber. (g) Multiple fluorescent beam spots imaged on the third fiber. (h) Concurrent multiple fluorescent beam spots on all fibers. All white bars: 200 μm.
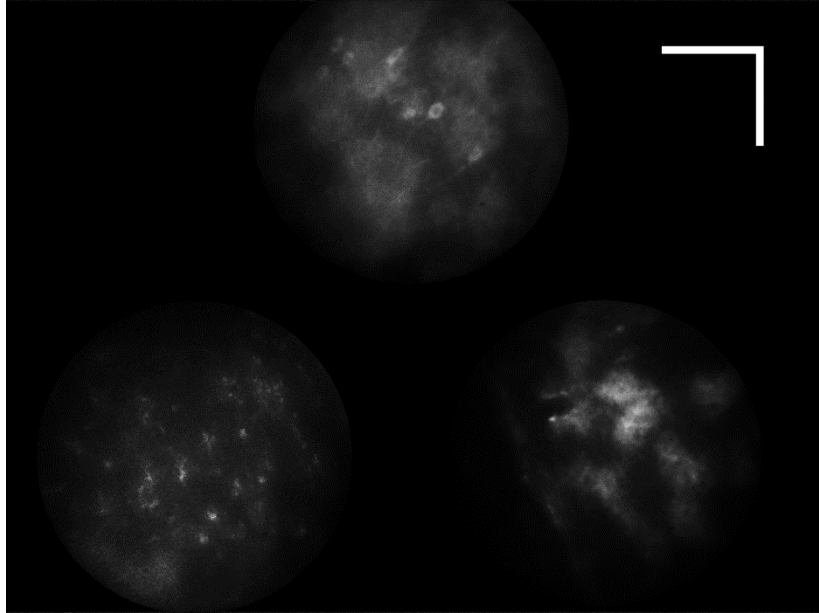
Figure 3.22. Simultaneous imaging of multiple brain regions, white bars: 200 μm.

For the evaluation of spatially multiplexed imaging capability, we performed imaging of three different regions of red fluorescent expressing mouse brain samples. As depicted in Figure 3.22, spatially multiplexed three images appear together. Different types of fluorescent cells in discrete brain regions are clearly visible and distinguished [20, 49].

3.4.3 Discussion

The current limitation on the DMD-based system is huge loss in energy transfer due to diffraction; this can be further improved by utilizing a high-power light source or holographic approaches [15].

The photostimulation generated by the developed system may activate relatively large numbers of Ch2-expressing cells or subcellular components around targeting areas

because of the large beam size, even when the optical methods are used for local illumination or for cell-specific targeting, which will result in difficulties in fine manipulations. This can be further improved using a greater numbers of micromirrors with smaller individual mirror size in the DMD. In freely moving animals, simultaneous imaging and manipulation with a fiber bundle enabled near-cellular resolution photoactivation [15].

Further development of new optical sensors and light-sensitive proteins with different spectra are also required for finer imaging and manipulation. Potential applications include ratiometric calcium imaging [58] and neural activity imaging of mice expressing ultrasensitive fluorescent calcium sensor proteins such as GCaMP6 or RcaMP [7, 59].

The multiplexing number of this system can be simply amplified by adding a channel of fibers without modification of the basic configuration of the current system. Thus, simplicity and expandability are two of the major advantages of this spatial-multiplexing design. This system is not only suitable for recording brain activities from multiple sites in freely behaving animals [60], but also enables the possible imaging of multiple animals [21], or multiple organs at the same time by reaching fiber channels to each target.

CHAPTER 4: STRUCUTRED ILLUMINATION FIBER-BUNDLE MICROSCOPY AND IMAGE QUALITY ENHANCEMENT

4.1   Background and Overview

Although the standard fiberscopes introduced in the previous chapter provide high quality *in vivo* imaging, to push the fiberscope technology further toward the super-resolution imaging a structured illumination microscopy (SIM), that can significantly improve image resolution and SNR compared to wide-field fiber bundle microscopy, is designed and developed. SIM employs a combination of optical manipulations and computational algorithms to obtain optical sections and/or two-dimensional images featuring significantly improved resolution.

In terms of optical sectioning, due to the fact that fluorescence emission originating from structures outside the focal plane is far less modulated, the in-focus information can be easily discriminated from the out-of-focus information simply by comparing several images where the pattern resides at different lateral positions. Fluorescence arising from structures that lie outside the focal plane will not vary in intensity between the successive images, whereas emission from structures residing at the focal plane will feature a clear variation in their intensity patterns depending on the position of the modulated excitation pattern. Thus, an optical section can be calculated by comparing the intensities between images on a pixel-by-pixel basis. As presented in Figure 4.1, three raw images captured using an evenly spaced grid pattern at different positions verify that fluorescence arising from outside the focal plane does not exhibit variations between the three images. In contrast, emission originating from structures within the focal plane varies dramatically with the grid position such that comparison of

the emission intensity changes between the grid images enables removal of fluorescence during mathematical calculation of an optical section. Note the region of blurred high fluorescence intensity originating in a region removed from the focal plane that is indicated in Figure 4.1 by white arrowheads.
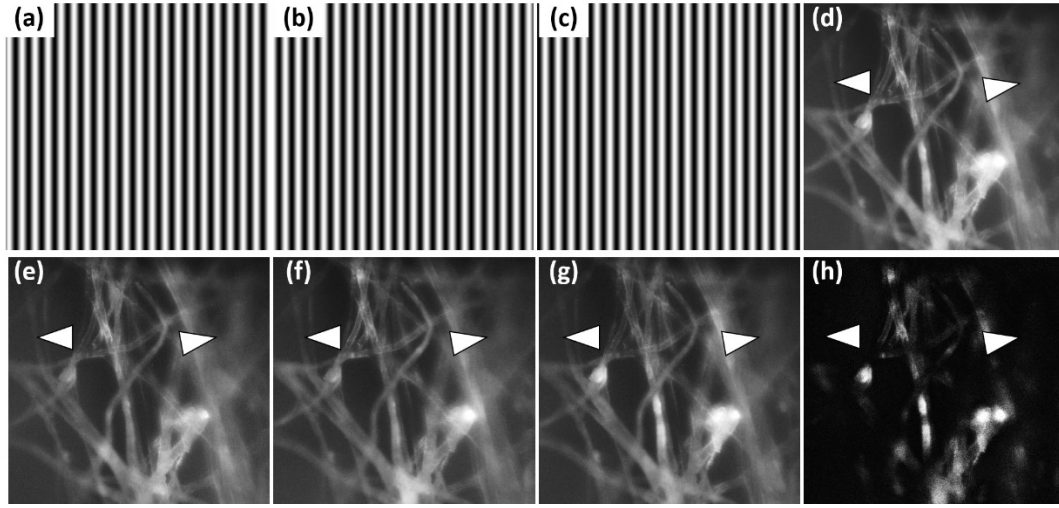
Figure 4.1. Three phase shifted structured illumination images (a, b, c), wide-field fluorescence image and its reconstruction (e, f, g) for optical sectioning (h).

When optical sectioning is conducted using non-coherent light sources, such as an Halogen bulb, the axial response of the grid projection can be approximated using the following equation:

$$r_z = (3.83/16\pi)(\lambda \times 10^{-3})/[(\eta \sin^2(\alpha/2)v_g(1 - v_g/2)], \qquad (1)$$

where λ is the illumination wavelength in nanometers, η is the refractive index of the imaging medium, α is the aperture angle of the objective, and v_g is the effective grid frequency in the specimen plane:

$$v_g = (M\lambda v)/(b \cdot NA), \qquad (2)$$

In the grid frequency equation (2), M is the objective magnification, v is the grid frequency, b is an instrument-dependent magnification factor of the reflected light beam path, and NA is the objective numerical aperture. As a result, the thickness of an optical section is determined by the grid frequency and the objective characteristics. The choice of the illumination pattern density very much depends on the type of sample as well as on the intended method of data processing [28]. A comparatively thick sample and/or a sample with volume-like staining is more difficult to process when using densely patterned illumination because the large amount of out-of-focus fluorescence will dominate the small amount of modulated fluorescence stemming from the focal plane. An elegant way to achieve sufficient flexibility and to optimize this trade-off between relatively noise-free sectioning and fast acquisition speed is to generate the pattern using a programmable array such as an SLM or DMD.

SIM can also be used to achieve resolution beyond the diffraction limit. As described in Chapter 2, the Abbe resolution limit criterion provides an indication of a classical resolution limit in an optical microscope. In terms of spatial frequency, the Abbe limit defines the finest periodic structure that can be imaged by an optical microscope. Light scattered from an object consists of individual components of different frequencies with various phases and magnitudes (the spatial frequency components) [61]. Fine object features will scatter light into high-frequency components that propagate at large angles. The image formed by an optical microscope is the summation of the components that pass through the aperture of the objective lens and arrive at the image plane. However, the aperture of the objective lens is finite so that it is not capable of collecting very high spatial frequency components scattered from a very fine structure. Therefore, the aperture

of the back focal plane of the objective lens plays the role of a low-pass filter, blurs the image, and determines the resolution of the optical system. Thus, the SIM technique is developed to extend the resolution beyond this limit by shifting high spatial frequencies from outside the observable region into the observable region in the form of moiré fringes [62]. A set of images that were prepared from three phases at 120˚ orientations, which ultimately after processing, yield a real image that contains twice the spatial resolution as would be observed in wide-field fluorescence microscopy [63, 64]. Let us assume that the object image $D(r)$ and observed image $O(r)$ are related by:

$$O(r) = D(r) \cdot I(r), \qquad (3)$$

where $I(r)$ is the structured illumination pattern, and r is the spatial vector of the x and y coordinates.

The Fourier transform of this relation is the convolution:

$$O(k) = D(k) \otimes I(k), \qquad (4)$$

where k is the spatial frequency vector in reciprocal space. This convolution mixes information from outside the observable region into the observable region in reciprocal space [65]. Therefore, the observed patterned image contains previously unobservable information. If the structured illumination pattern is chosen properly, the unobservable information in moiré fringe form can be decoded and restored. A reconstruction can be created with the previously unavailable super-resolution information to get the super-resolved image. Because the resolution extension is based on the structured illumination pattern's frequency, $I(r)$ should be as fine as possible to get maximal resolution [65, 66]. In general, the structured illumination is a sinusoidal pattern of parallel stripes:

$$I(r) = I_0 \left[1 + \cos(2\pi f_0 \cdot r + \phi) \right], \qquad (5)$$

60

where f_0 is the frequency of the illumination pattern and ϕ is the phase of the illumination pattern in real space. The Fourier transform of that pattern consists of three delta functions:

$$I(k) = I_0[\delta(k) + \frac{1}{2}\delta(k + k_0)e^{i\phi} + \frac{1}{2}\delta(k - k_0)e^{-i\phi}], \quad (6)$$

so that convolution integral (4) becomes a sum of three components. The phase factor, $e^{i\phi}$, represents the phase ϕ of the illumination pattern in reciprocal space. The observed image, $O(k)$, at each point k in reciprocal space only depends on three information components:

$$O(k) = I_0[D(k) + \frac{1}{2}D(k + k_0)e^{i\phi} + \frac{1}{2}D(k - k_0)e^{-i\phi}]. \quad (7)$$

It is not possible to separate the contributions from the three terms of (5) based on only a single image. However, three observations with different values of ϕ will normally supply three independent versions of (5), enabling the separation of the three contributions. This process can be repeated with the pattern at different orientations, resulting in an image of the object at double the normal resolution. Equation (5) has three components: the unshifted object Fourier transform, $D(k)$, and two shifted copies of the object Fourier transform, $D(k + k_0)$ and $D(k - k_0)$. The shifted components contain part of the object's unobservable information in a conventional imaging system. The structured illumination process makes the previously unobservable information accessible by shifting these components into the optical transfer function (OTF) support region of the conventional microscope. To obtain the superresolved image, the three information terms need to be separated and moved back to their proper positions. The unshifted component

$D(k)$ does not need to be moved, but the spatial frequencies of those shifted components from $k+k_0$ and $k-k_0$ coordinates should be moved back to the k coordinates [65, 66]. Then, a reconstruction is generated to restore all components to get a super-resolved image. If the numerical aperture of illumination is the same as that of observation, the illumination pattern frequency f_0 cannot exceed k_0. The new resolution limit is then $k+k_0=2k_0$. Hence, by using linear structured illumination one can at most double the resolution of the conventional wide-field fluorescence microscope [63, 64]. However, doing this only at one dimension extends resolution in a single direction, which as described in optical sectioning. In order to approximate an OTF support of radius $2k_0$ one must repeat this process using several different orientations of the grid pattern.
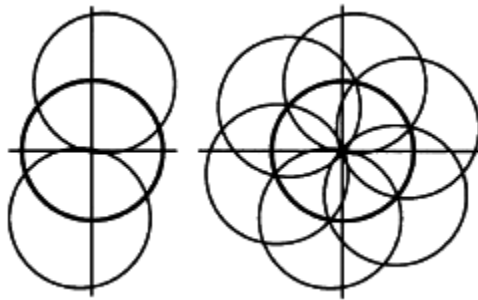
Figure 4.2. Resolution can be two-fold increased in 2D by changing angle of frequency mixing.

This chapter describes the use of linear structured illumination to overcome diffraction limited resolution in wide-field fiber bundle imaging and provide solutions to improve the image quality of fiber bundle images.

In section 4.2, the SIM technique is applied to depth-resolved fiberscopy that removed background noise and enhanced optical sectioning. The structured light is

illuminated by a programmable micromirror array, which is capable of rapid reconfiguration of illumination pattern and modulation frequency.

In section 4.3, the lateral resolution enhancement of fiberscope images is illustrated through numerical and analytical calculations based on previous work [67]. The performance of linear structured illuminated and wide-field illuminated fiber microscopes is compared using a USAF 1951 target and Purkinje cells from a mouse brain.

4.2 Depth-resolved Fiber bundle Microscopy using Programmable Digital Micromirror Device (DMD) based Structured Illumination

In this section, a depth-resolved SIM fiberscopy using a high-speed DMD is presented to enhance optical sectioning in wide-field fiber bundle fluorescence microscopy. The system performance is characterized using phantom samples of brain slice and mouse kidney, and validated through *in vivo* brain imaging using a head-fixed live transgenic mouse, expressing GFP fluorescence signals within astrocytes.

4.2.1   Method

4.2.1.1 System implementation
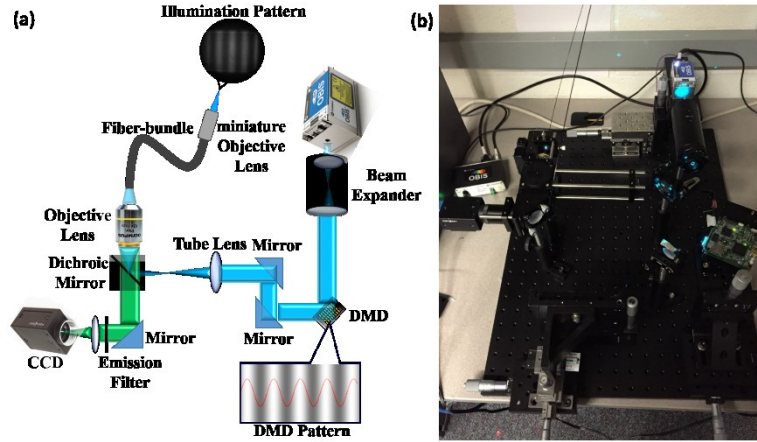
Figure 4.3. System configuration (DM: dichroic mirror, BS: 50:50 beam splitter, GM: galvo mirror, OL: objective lens, FL 1&2: focusing lens, LP: longpass filter, APD 1&2: avalanche photodetector, DAQ: digital-to-analog & analog-to-digital converter).

The optical layout of the DMD-based fiberscope imaging system and a photo of

implementation are shown in Figure 4.3. Excitation light is provided by a 50-mW, 488-

nm laser (OBIS488LX, Coherent Inc.) The laser beam is passed through a 20X beam

expander (#55-579, Edmund Optics) to fill the active area of the DMD (DLP3000, Texas

Instruments). The expanded beam is guided by two silver mirrors, relayed through a tube

lens, and then reflected by a dichroic mirror (DMLP490, Thorlabs) in series and coupled

into a multi-core fiber bundle by a microscope objective lens (Plan 10X/0.3, Olympus).

The tube lens is utilized to adjust the magnification between the DMD and the proximal

facet of the fiber bundle. For the demonstration of optical sectioning, a high-resolution

imaging probe consisting of a 30,000 core fiber bundle (FIGH-30-650S, Fujikura) and a

custom-built miniaturized objective (0.55 *NA*, 1.3X magnification), with an active image

diameter of 500 µm, was used. Fluorescence light originating from the specimen is

decoupled into the same fiber, passes through the dichroic mirror, and is focused by a condensing lens onto the CCD camera (GS3-U3-15S5M-C, Point Grey Research). A bandpass emission filter improves the green fluorescence specificity. The illumination pattern, modulation frequency, DMD, and CCD camera are controlled by MATLAB Image Acquisition Software (Matlab 2015b, Mathworks).

4.2.1.2 Illumination pattern, modulation frequency, and optically-sectioned image

Three phase shifted sinusoidal patterns of light were generated by the DMD and illuminated through the imaging probe. One of the main advantages of using a programmable DMD array over conventional grating-based structured illumination is that one can rapidly change the modulation frequency and greatly increase the frame rate [68]. In this system configuration, a grid period of 100 μm provided a reasonable compromise. The three obtained images were computed to create an optically sectioned image based on simple linear algebra, proposed by [69]:

4.2.1.3 First in first out roll image processing and band-reject filtering

Structured illumination requires three images to be taken in sequence in order to form one optically sectioned image, which reduces the system's frame rate by three fold. Any motion on the order of micrometers between these images creates artifacts that can greatly distort the final image. Thus, to avoid a slow output rate, optically sectioned image can be calculated over a rolling time-stack of images that is updated by adding each new image frame to the processing image stack and removing the oldest image from the stack. This first in first out (FIFO) strategy coupled with fast DMD operation allows the output rate to be as high as the camera frame rate, making the imaging system

insusceptible to any motion artifacts. However, the system would still suffer from initial latency, that is, the output would trail the real-time by a latency of the first three images taken. Therefore, the initial delay should be compensated in post-hoc analysis. After the linear combination of consecutive images, the optically sectioned SIM image still contains honey-comb pattern artifacts. Thus, this noise was removed by applying band-reject filtering in the Fourier domain.

4.2.1.4 Animal protocols

All animal procedures were approved by the Johns Hopkins University Animal Care and Use Committee. Cre knock-in GFP mice were generated. GFP was expressed in astrocytes to image fluorescence. For *in vivo* studies, all animal surgeries were performed under aseptic conditions. The animals were anesthetized with 1.5-2% isoflurane in 95% oxygen. The head was shaved, cleaned with 70% ethanol and betadine, then a scalp incision was made and a small craniotomy was performed using a dental drill with the stereotaxic apparatus. We then place a coverslip (4 mm^2 in size, 100 μm thick) over the craniotomy and then secured it with cement. A head plate was then cemented to the animal's skull. After the surgery, the head of the animal was immobilized with a custom-designed head-fixation stage. To image, the laser power was optimized to 0.4 mW/mm^2 to prevent brain tissue damage. The tip of the imaging probe was positioned over the

4 mm^2 cranial window by micromanipulators. The continuous duration of *in vivo* imaging never exceeded a maximum of one minute.

4.2.2   Experimental Results

4.2.2.1 System characterization
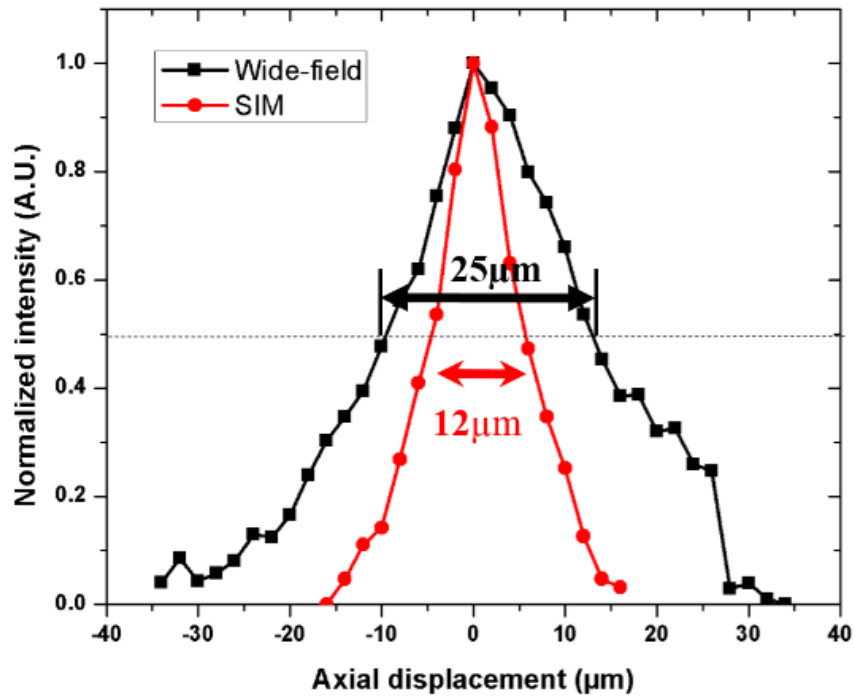
Figure 4.4. Optically-sectioning test.

To characterize the system, 4 µm beads were used to provide system's optical sectioning performance. Measured axial resolutions of the system are found to be 25 µm in wide-

field illumination mode and 12 μm in SIM mode, which indicates approximately two-times greater than that of wide-field illumination (see Figure 4.4.)

4.2.2.2 Phantom imaging results
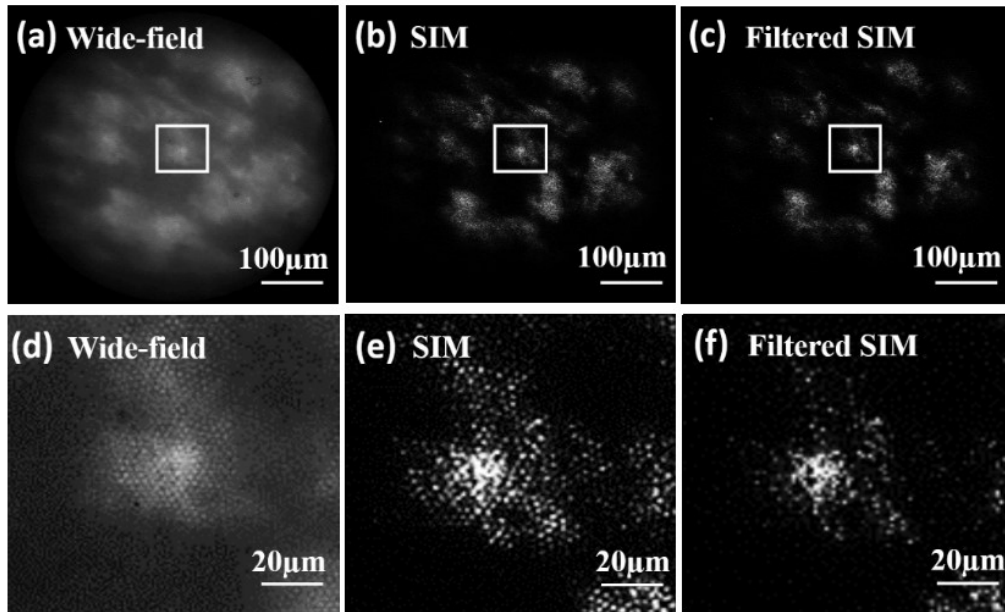
Figure 4.5. Optically-sectioned imaging using biological sample. (a) Wide-field fluorescence image of astrocytes. (b) Depth-resolved image of astrocytes. (c) Band-reject filtered image. (d), (e), (f) are zoomed images of the white boxes.

The system was also tested with thick biological samples of brain section and mouse kidney. Figure 4.5 provides comparisons of structured illuminated and wide-field illuminated images through a fiber bundle. As shown in Figure 4.5(c), one can see the sharp edges among astrocytes. Note that a Butterworth band-rejection filter effectively removes the honey-comb pattern noise from the calculated SIM image and the final image shows no pixelization. Mouse kidney tissue was also tested. As shown in Figure

4.6, blurry effects on wide-field illumination diminished and fine edges are clearly

visible.
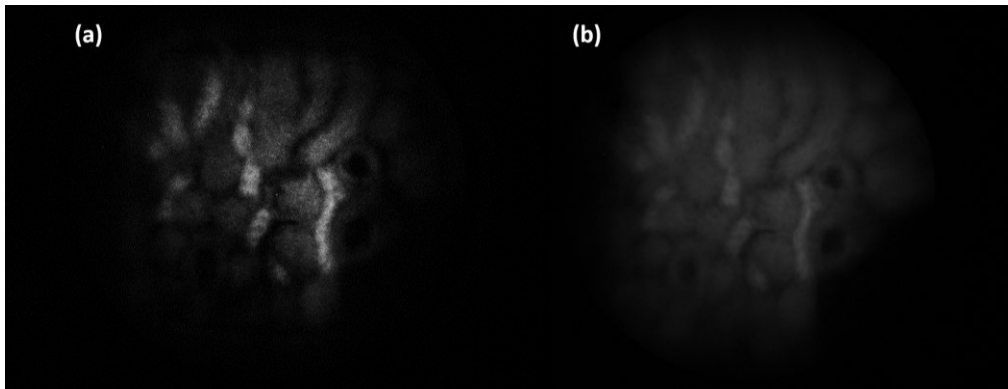
Figure 4.6. Mouse-kidney sample image. (a) SIM technique applied image. (b) Wide-field illumination image.

4.2.2.3 In vivo mice brain imaging
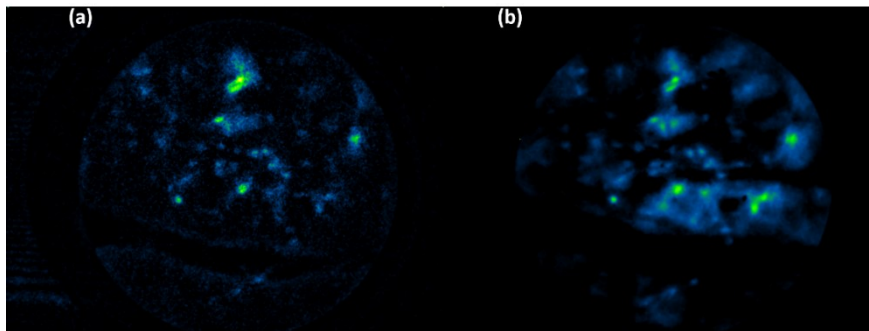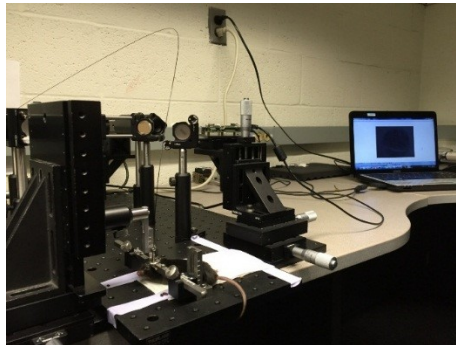
Figure 4.7. *In vivo* transgenic mouse brain imaging results. (a) Optically sectioned SIM image. (b) Wide-field illumination image.

Finally, the system was evaluated through *in vivo* transgenic mouse brain imaging with head-fixation, as shown in Figure 4.7. Optically-sectioned brain section images were obtained. As one can see from the Figure 4.7(a), GFP cells are clearly resolved and blurry parts are minimized.

4.2.3 Discussion

In this work, the implementation of depth-resolved fiberscope imaging is demonstrated using DMD-based structured illumination. The bead test results show that an axial resolution of 12 μm was achieved, which is comparable to results of conventional bench-top confocal fluorescence microscopes.

Taking multiple images can be disadvantageous in terms of speed, but modern CCD cameras employ fast readout systems with negligible readout noise. High-speed systems utilizing DMDs can greatly increase the frame rate, thus alleviating motion artifacts when imaging live tissues [68]. In addition, DMD systems are capable of changing modulation frequency rapidly and could be used to optimize grid patterns in real-time. However, DMDs often have highly inefficient light transmission, which requires a high-power incident light and a beam dump to block the residual light.

In addition, the first in first out roll processing allowed a real-time processing for optically sectioned imaging. This strategy is found to be particularly beneficial to live animal brain imaging, which can compensate for motion artifacts. This new method for

optically sectioned imaging creates a compelling combination of speed, sensitivity, and configurability that will allow imaging of intact brain imaging in freely moving animals.

To avoid information loss during the band-rejection filter process in the frequency domain, according to the Nyquist theorem, the cut-off frequency must not be greater than half of the sampling frequency of the fiber cores. The spectral filter in frequency domain acts like a low-pass filter and therefore compresses the range of gray values to a certain extent. To compensate for these degradation effects, one can use a histogram stretch [16] or high-pass filtering [70]. This can be further improved by applying adaptive spectral filters that automatically match the filter mask to various types of fiberscopes [71].

4.3   Super-resolution Fiberscope Imaging from Structured Illumination

In this section, lateral resolution enhancement of fiberscope images is presented. The performance of linear structured illuminated and wide-field illuminated fiber microscopes is compared through numerical and analytical calculations. Sequentially rotated one-dimensional pattern illumination and its reconstruction provide significant improvements of the lateral resolution and SNR.

4.3.1   Methods

To verify the analytical expressions derived in the section 4.1, numerical experiments were performed using phantom objects consisting of a USAF and a biological sample of purkinje neurons from transgenic mice brain.

4.3.1.1 Creation of object image

An object image of a USAF 1951 target for the SIM simulation is shown in Figure 4.8. A coherent flexible fiber bundle (FIGH-10-500N, Fujikura) mask, which is composed of a 10,000 core, 500-μm diameter with 2.9-μm core size and 4.5-μm spacing (Figure 4.13), is applied to simulate a fiber bundle image [17].
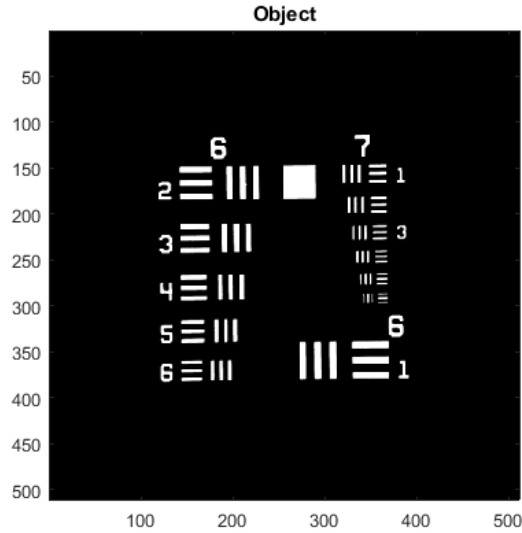
Figure 4.8. Object image, $D(r)$.

The OTF is the magnitude of each spatial frequency observed by the microscope. The simulations and numerical calculations in this study used an analytical wide field OTF for a diffraction-limited optical microscope in the paraxial approximation [63]. This OTF can be expressed as

$$OTF(k) = \{2b(|k|) - \sin[2b(|k|)]\}/\pi ,$$ (6)

where $b(k) = \cos^{-1}(k/k_0)$. Figure 4.9 shows this OTF.
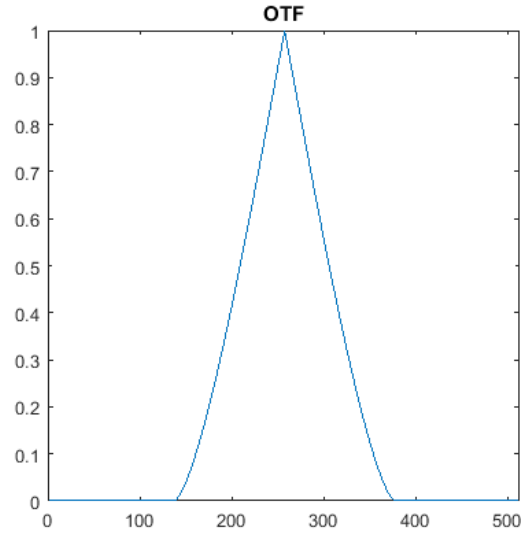
Figure 4.9. OTF spectrum magnitude plot. It is the plot of equation (6) in reciprocal space. The frequency index 255 represents 0 spatial frequency in reciprocal space. The interval from one frequency index to the next corresponds to a spatial frequency interval of $(1/512)/pixel$.

Here, k_0 is the radius of the normally observable region in reciprocal space. The normally observable region is shown in Figure 4.10. This simple expression is picked because the particulars of the OTF are unimportant for the general question. The highest spatial frequency for the OTF, f_c, is set to 180 frequency index where the frequency index 255 represents 0 spatial frequency in reciprocal space. The interval from one frequency index to the next corresponds to a spatial frequency interval of $(1/512)/pixel$.
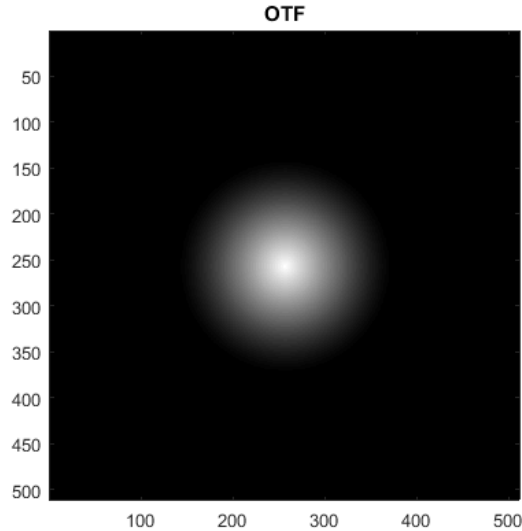
Figure 4.10. OTF spectrum image. It is the image of equation (6) in reciprocal space. The frequency index 255 represents 0 spatial frequency in reciprocal space. The interval from one frequency index to the next corresponds to a spatial frequency interval of $(1/512)/pixel$.

4.3.1.2 Point spread function (PSF) and optical transfer function (OTF)

The PSF is a system's impulse response from a point source to resultant spot on the image plane through the imaging system.

When the object is divided into discrete point objects of varying intensity, the image is computed as a sum of the PSF of each point. As the PSF typically is determined entirely by the imaging system, the images can be analyzed by specifying the optical characteristics of the system. This process can be formulated by a convolution equation.

4.3.1.3 Conventional wide-field fiberscope image

The OTF is the Fourier transform of the PSF. According to the property of convolution, convolving the object with the PSF in real space is equivalent to multiplying the Fourier transform of the object by the OTF in reciprocal space. The product of the multiplication of the Fourier transform of the object and the OTF is then transformed back to real space

74

again to avoid the convolution process. The result in real space is the normally

observable, or conventional, image.

The Fourier transform of the object image, $D(r)$, to reciprocal space is:

$$Dbar(k) = F[D(r)], \qquad (7)$$

where $F[\ ]$ represents the Fourier transform, which is shown in Figure 4.11.
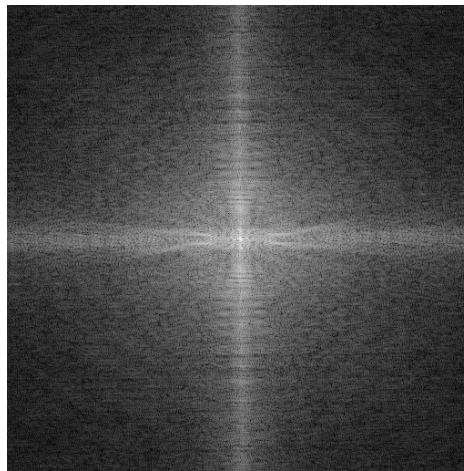
Figure 4.11. Fourier transform of object image $D(r)$ in reciprocal space, $Dbar(k)$.

Multiplying $Dbar(k)$ by the OTF results in

$$DHbar(k) = H(k) \times Dbar(k). \qquad (8)$$

The OTF support region of the object image, $D(k)$, in reciprocal space, is shown in

Figure 4.12.
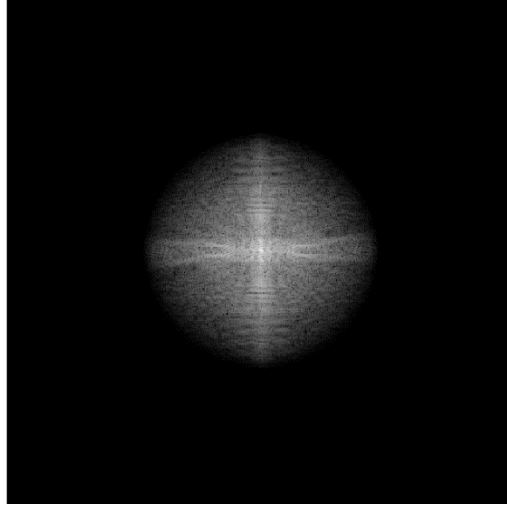
Figure 4.12. OTF support region in reciprocal space, $DHbar(k)$.

Then, transforming back to real space results in:

$$DP(r) = F^{-1}[DHbar(k)], \quad (9)$$

where $F^{-1}[\ ]$ represents the inverse Fourier transform and $DP(r)$ is the sum of the

inverse Fourier transform of $DHbar(k)$ in real space. If we apply fiberscope honey-

comb pattern mask to $DP(r)$, one can see its Fourier transform $DPbar(k)$ as shown in

Figure 4.13.

Comparing Figure 4.7 with Figure 4.13, it can be seen that, after applying the PSF

and fiberscope honey-comb pattern mask, the object image, $D(r)$, that consists of a two-

dimensional USAF target, is changed into a blurred image, $DP(r)$, which simulates a

conventionally observed image in a fiberscope. The goal of this study is to enhance

lateral resolution of the conventionally observed fiberscope images using the super-

resolution structured illumination technique.
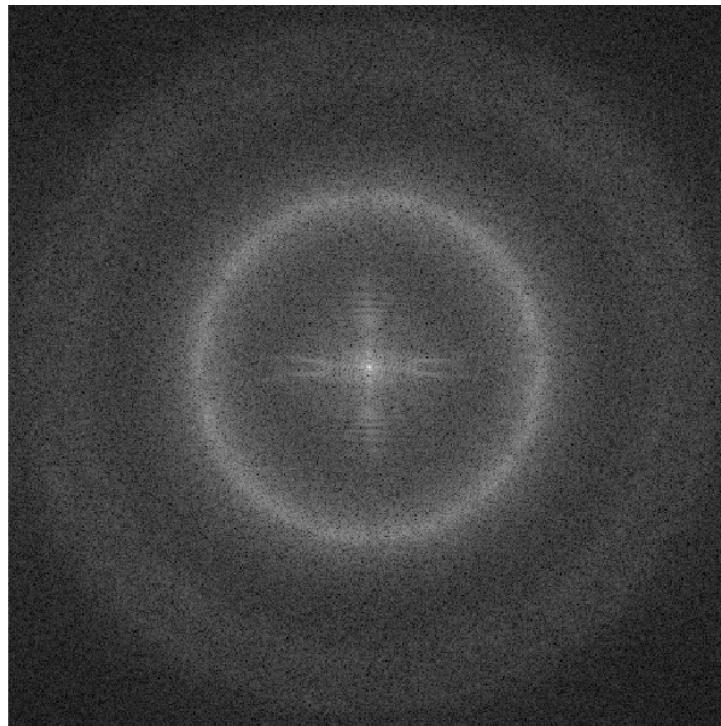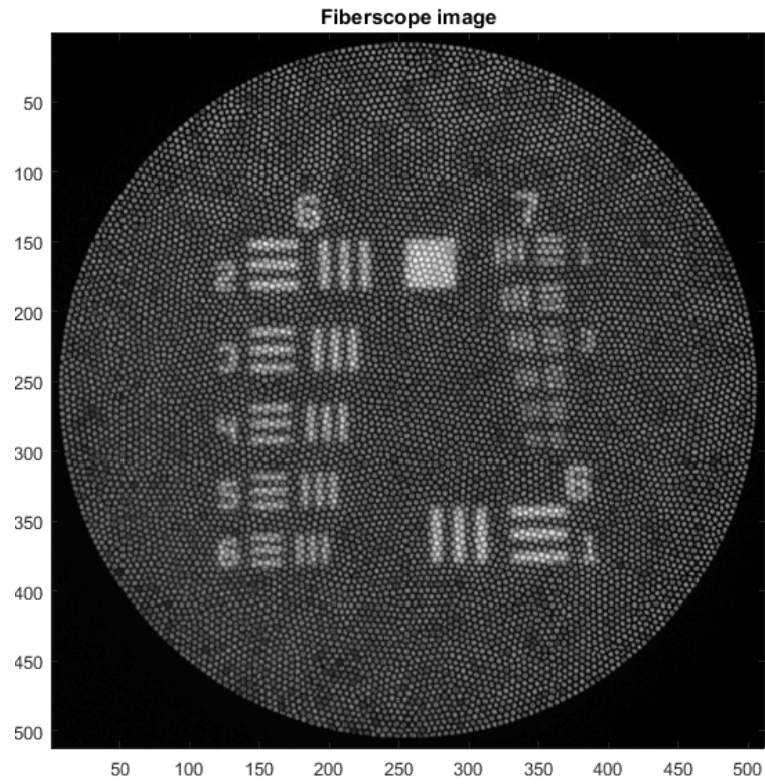
Figure 4.13. Conventional fiberscope image, $DP(r)$ and its Fourier transform, $DPbar(k)$.

4.3.1.4 Structured illumination patterns

As mentioned before, a sinusoidal pattern of parallel stripes is used in this study to generate the illumination pattern, $I(r)$. The illumination pattern is shown in Figure 4.14 for an orientation of 120˚, where orientation is measured clockwise from the horizontal.
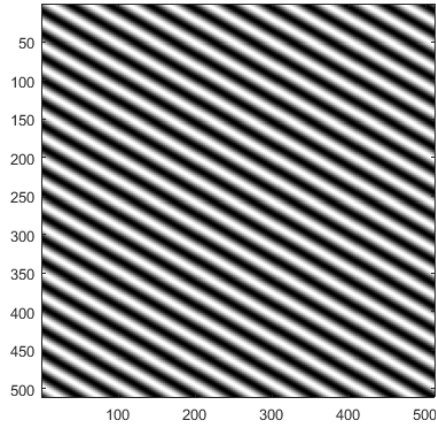
Figure 4.14. Illumination pattern, $I(r)$, with $\varphi = 240˚$, orientation $= 120˚$ in real space.

Figure 4.15. Illuminated image in real space, $DI(r)$. It is illuminated by the illumination pattern shown in Figure 4.14.

In real space, the product of the illumination pattern, $I(r)$, and the object image, $D(r)$, is the illumination patterned object image, $DI(r)$, shown in Figure 4.15. It is then transformed to reciprocal space, $DIbar(k)$, as shown in Figure 4.16. Then, it is multiplied by the OTF to get the conventionally observable patterned image, $DIbars(k)$,

$$DIbars(k) = H(k) \times DIbar(k) . \qquad (10)$$

In equation (10), the patterned object image is limited by the OTF. However, there is some super-resolved information in the shifted components.
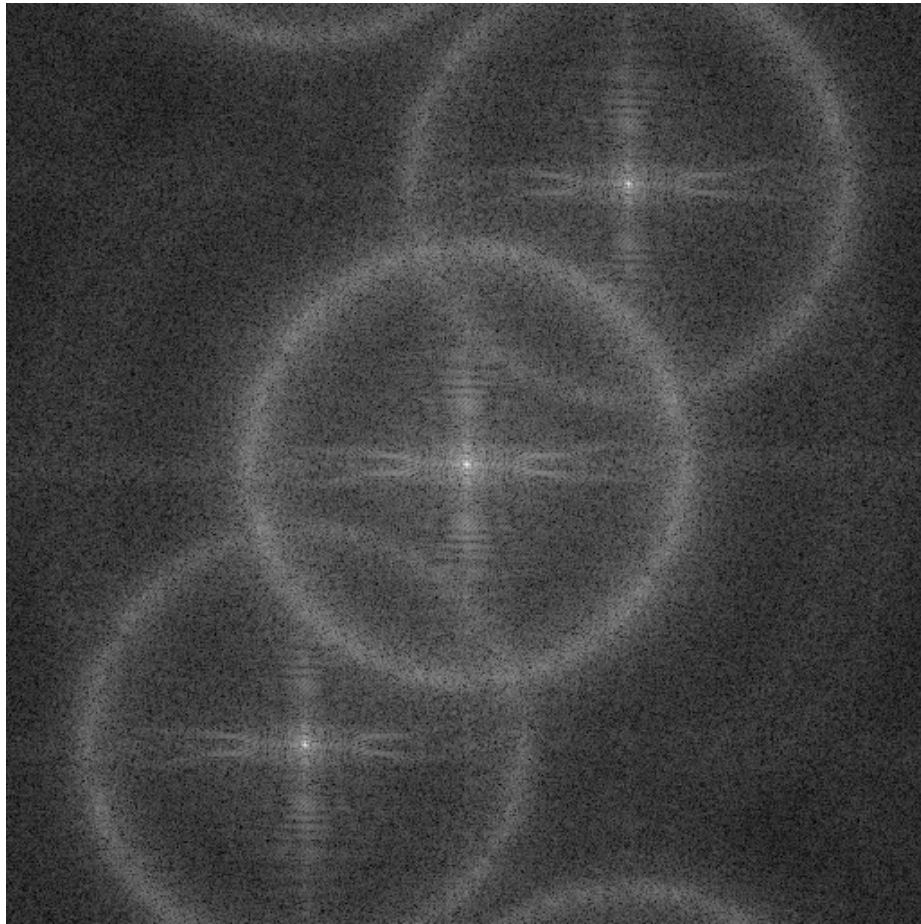
Figure 4.16. Illuminated object in reciprocal space, $DIbar(r)$.

4.3.1.5 Shifted components

As shown in equation (4), the Fourier transform of a sinusoidal pattern consists of three

impulses. The Fourier transform of an object illuminated by this pattern contains three

replicas of the object spectrum. The three components are visualized in Figure 4.16

Figure 4.17 shows a slice through Figure 4.16 at orientation = 120˚. All three components

are combined appropriately to obtain a super-resolved image, $rc(k)$, as shown in Figure

4.18.
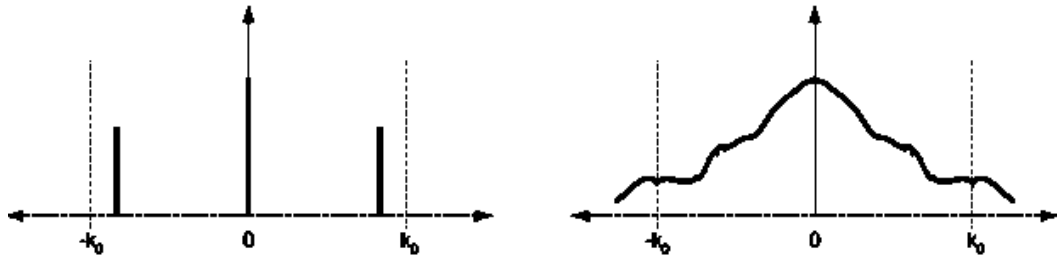
Figure 4.17. Magnitude plot of illuminated object, $DIbar(k)$. This is the plot of equation (5). It is a slice through Figure 4.16 at orientation = 120˚.
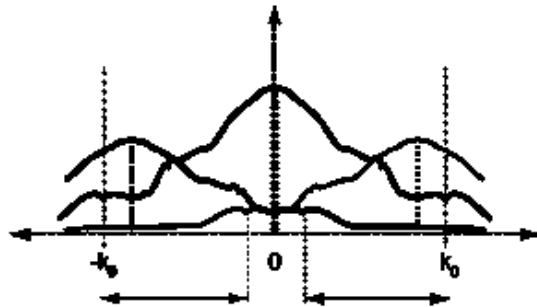
Figure 4.18. Magnitude plot of reconstructed object, $rc(k)$. The detectable region is the normal OTF support region and the plot is the reconstruction of Figure 4.17, after moving the shifted components back to their proper positions.

In order to solve for the three unknown components, three or more images are

needed. The traditional technique uses three images with phase shifts of 0˚, 120˚, and 240

˚ in the sinusoidal illumination [63]. Figure 4.19 shows sinusoidal patterns with three phases for three different orientations. For each orientation, there are three unknown components.
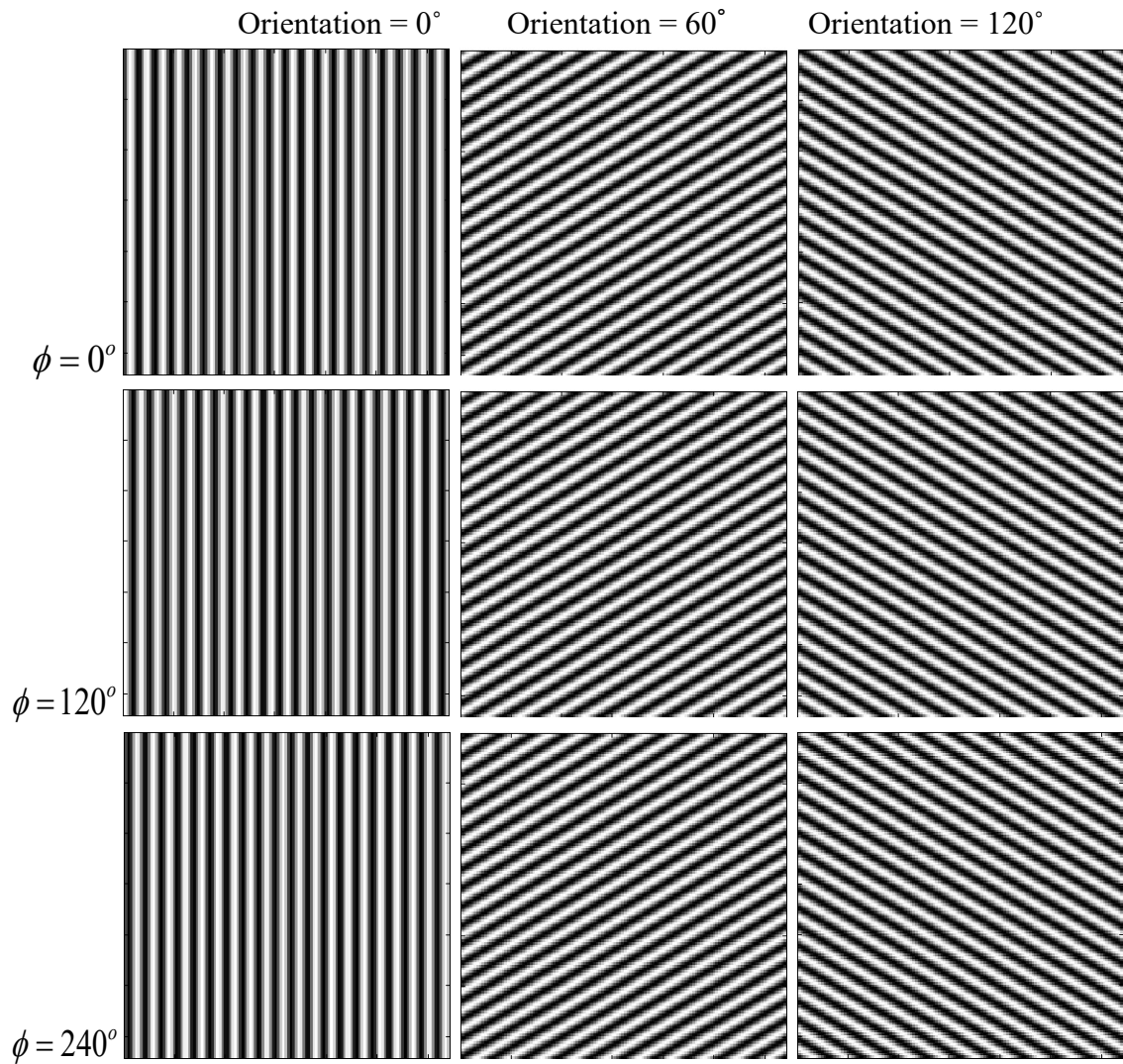
Figure 4.19. Illumination pattern, $I(r)$, in three phases and orientations. They are printed on 512 × 512 pixel grids with the same scales.

4.3.1.6 Information components separation

According to Shroff et al [66], let $H_1(k)$ and $H_2(k)$ be the optical transfer functions

(OTFs) of the illumination and imaging paths, respectively. Recall that $Dbar(k)$ is the

Fourier transform of the object intensity, and $DIbars(k)$ is the Fourier transform of the

OTF support patterned object. The resulting matrix is

$$
\begin{bmatrix} DIbars_1(k) \\ DIbars_2(k) \\ DIbars_3(k) \end{bmatrix} = \begin{bmatrix} e^{i\cdot 0} & e^{i\cdot\phi_1} & e^{-i\cdot\phi_1} \\ e^{i\cdot 0} & e^{i\cdot\phi_2} & e^{-i\cdot\phi_2} \\ e^{i\cdot 0} & e^{i\cdot\phi_3} & e^{-i\cdot\phi_3} \end{bmatrix} \times \begin{bmatrix} \dfrac{1}{2}H_1(0)H_2(k)Dbar(k) \\ \dfrac{1}{4}H_1(k_0)H_2(k)Dbar(k-k_0) \\ \dfrac{1}{4}H_1(-k_0)H_2(k)Dbar(k+k_0) \end{bmatrix}. \qquad (11)
$$

Since the Fourier transforms of the patterned object and the three phases, $\phi_1 = 0$,

$\phi_2 = 120^o$, $\phi_3 = 240^o$, are already known, the Fourier transforms of the shifted object can be

solved by inverting the matrix, which is the shifting factor matrix. For this project, the

equation is solved numerically.

First,

$$
\begin{bmatrix} \dfrac{1}{2}H_1(0)H_2(k)Dbar(k) \\ \dfrac{1}{4}H_1(k_0)H_2(k)Dbar(k-k_0) \\ \dfrac{1}{4}H_1(-k_0)H_2(k)Dbar(k+k_0) \end{bmatrix} = \begin{bmatrix} e^{i\cdot 0} & e^{i\cdot\phi_1} & e^{-i\cdot\phi_1} \\ e^{i\cdot 0} & e^{i\cdot\phi_2} & e^{-i\cdot\phi_2} \\ e^{i\cdot 0} & e^{i\cdot\phi_3} & e^{-i\cdot\phi_3} \end{bmatrix}^{-1} \times \begin{bmatrix} DIbars_1(k) \\ DIbars_2(k) \\ DIbars_3(k) \end{bmatrix}. \qquad (12)
$$

Substituting $\phi_1 = 0$, $\phi_2 = 120^o$, and $\phi_3 = 240^o$ in (12) results in:

$$\begin{bmatrix} \dfrac{1}{2}H_1(0)H_2(k)Dbar(k) \\[2mm] \dfrac{1}{4}H_1(k_0)H_2(k)Dbar(k-k_0) \\[2mm] \dfrac{1}{4}H_1(-k_0)H_2(k)Dbar(k+k_0) \end{bmatrix} = \begin{bmatrix} 1 & 1 & 1 \\ 1 & -0.5+0.866i & -0.5-0.866i \\ 1 & -0.5-0.866i & -0.5+0.866i \end{bmatrix}^{-1} \times \begin{bmatrix} DIbars_1(k) \\ DIbars_2(k) \\ DIbars_3(k) \end{bmatrix}. \quad (13)$$

The three components, $\dfrac{1}{4}H_1(k_0)H_2(k)Dbar(k-k_0)$, $\dfrac{1}{4}H_1(k_0)H_2(k)Dbar(k+k_0)$,

and $\dfrac{1}{2}H_1(0)H_2(k)Dbar(k)$ are thus obtained. Figure 4.20 shows the three components

for each orientation.

$\phi = 240^{o}$
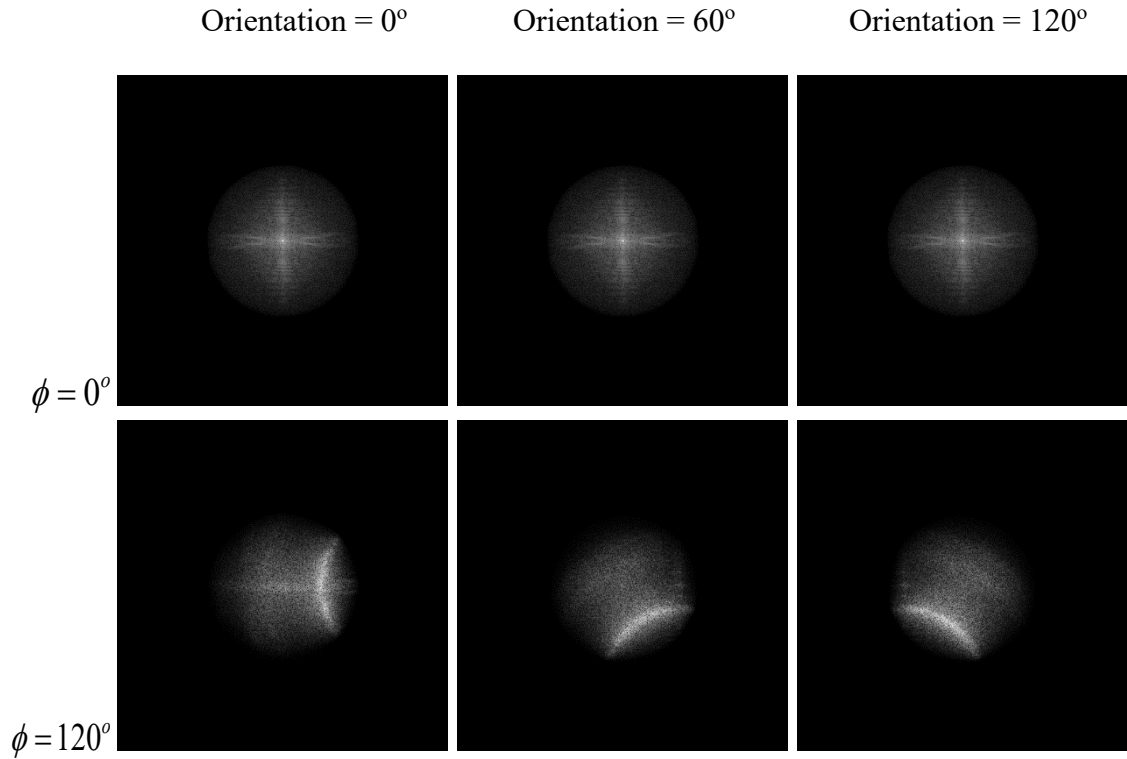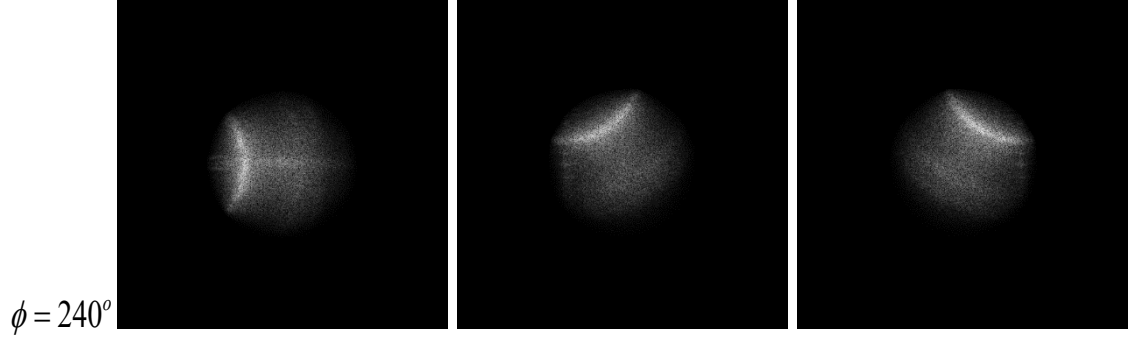
Figure 4.20. Components for three different phases and orientations. They are the results of the information components separation after applying the respective illumination patterns shown in Figure 4.19. All the images are printed on 512×512 pixel grids with the same scales.

4.3.1.7 Information component analysis

The separated terms in matrix of (13), which are the Fourier transforms of shifted objects in reciprocal space, are now analyzed [66]. The term

$$sp_{c1}(k) = \frac{1}{2}H_1(0)H_2(k)Dbar(k) \qquad (14)$$

is the unshifted component image for $0°$ orientation. It has an OTF given by

$$otf_1(k) = \frac{1}{2}H_1(0)H_2(k) . \qquad (15)$$

The second separated term, $\frac{1}{4}H_1(k_0)H_2(k)Dbar(k-k_0)$, is the shifted component

image containing the superresolution information from the conventionally unobservable

region. A shifting factor, $Ir(k)$, is introduced to sub-pixel shift the components. By using

the shifting factor, the second separated term can be shifted from the $(k-k_0)$ coordinates

back to the (k) coordinates to obtain: $sp_{c2}(k) = \frac{1}{4}H_1(k_0)H_2(k+k_0)Dbar(k)$. This

procedure is repeated for the third separated term to obtain

$$sp_{c3}(k) = \frac{1}{4}H_1(-k_0)H_2(k-k_0)Dbar(k) \qquad (16).$$

The OTFs for $sp_{c2}(k)$ and $sp_{c3}(k)$ are

$$otf_2(k) = \frac{1}{4}H_1(k_0)H_2(k+k_0),\qquad (17)$$

$$otf_3(k) = \frac{1}{4}H_1(-k_0)H_2(k-k_0).\qquad (18)$$

The derivation shown above follows that of Shroff et al.[66]. This process is repeated for 60° and 120° orientations of the sinusoidal illumination pattern. Thus, six more component images can be obtained. There are four component images with super-resolution along their respective rotations in Fourier space, given as $sp_{c5}(k)$ and $sp_{c6}(k)$ for 60° orientation, as well as $sp_{c8}(k)$ and $sp_{c9}(k)$ for 120° orientation. They have their own OTFs, $otf_5(k)$, $otf_6(k)$, $otf_8(k)$, and $otf_9(k)$. There are other two components, given as $sp_{c4}(k)$ and $sp_{c7}(k)$. They are the unshifted versions for 60° and 120° orientations, having OTFs similar to $otf_1(k)$, given as $otf_4(k)$ and $otf_7(k)$. These nine components need to be reconstructed with their OTFs to get an image with super-resolution in all directions in reciprocal space.

Here, the shifting factor, $Ir(k)$, given by

$$Ir(k) = \exp\{i[\cos(k\phi_i)+\sin(k\phi_i)]\},\qquad (19)$$

where the ϕ_i represent the different phases of 0, $2\pi/3$, $4\pi/3$, is applied to move the separated components back to their proper positions. The shifting factor, $Ir(k)$, shifts the different image components along with the super-resolution information back to the center of the observable region. The moved component images, $replc_{ci}(k)$, can be

reconstructed as a super-resolved image by adding them together as shown in Figure

4.21. Once all the components are combined, a deconvolution is needed to eliminate the

OTF.

	Orientation $= 0°$	Orientation $= 60°$	Orientation $= 120°$
$\phi = 0°$			
$\phi = 120°$			
$\phi = 240°$			
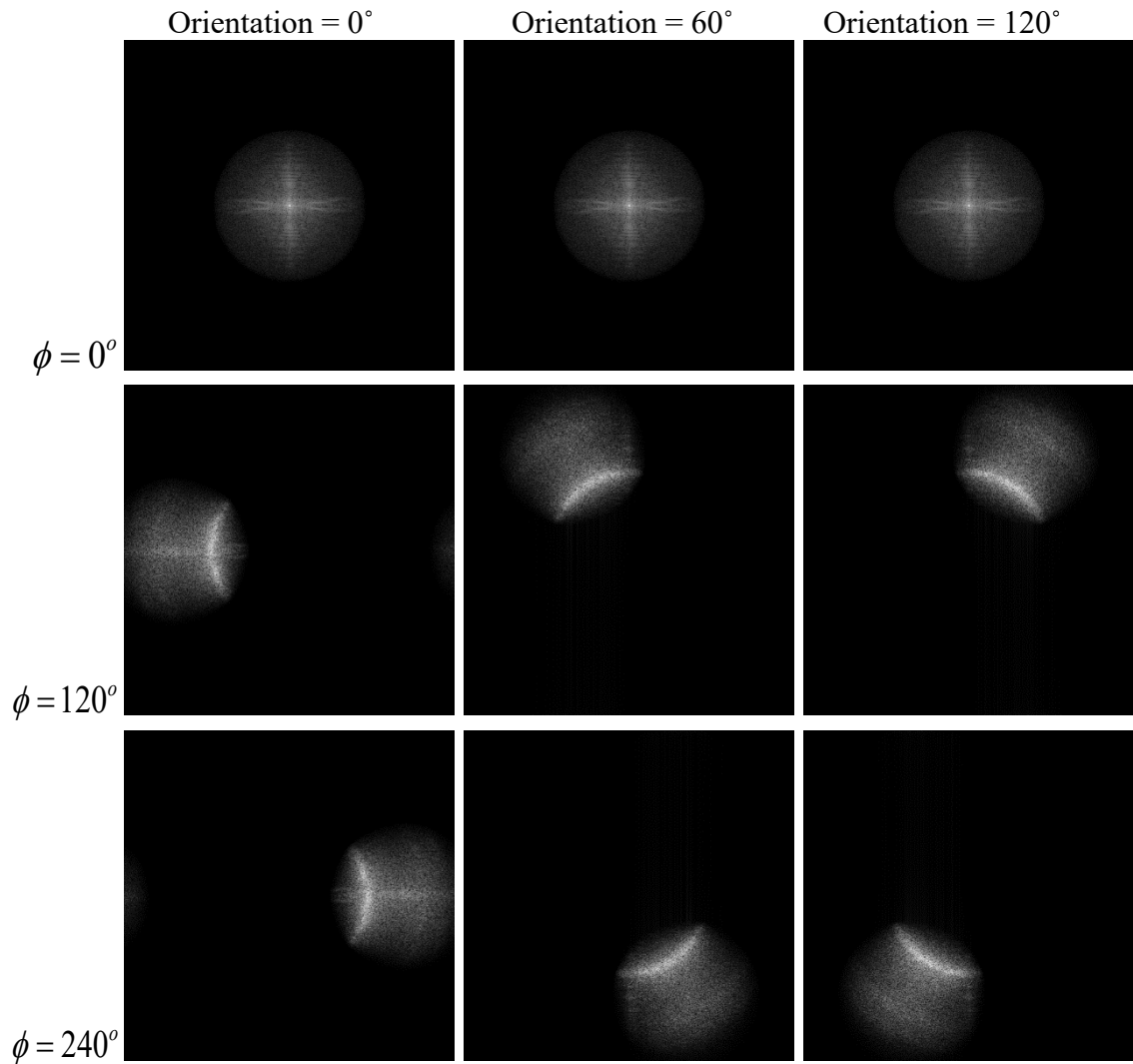
Figure 4.21. Moved components, $replc_{ci}(k)$. They are the results of moving the respective images shown in Figure 4.20 by the shift factor, $Ir(k)$, shown in equation (19).

4.3.1.8 Information components reconstruction

After obtaining the moved component images, $replc_{ci}(k)$, one estimate, $dr(k)$, of the object information, $Dbar(k)$, in reciprocal space for each phase and each pattern orientation is obtained as:

$$dr(k) = \sum_{i=1} \frac{4replc_{ci}(k)}{otf_i(k)}, \qquad (20)$$

where $otf_i(k)$ represents the proper OTFs for the moved component images, $replc_{ci}(k)$.

Each such estimate is valid in the circular region $|k| \leq k_0$, where $otf_i(k) \neq 0$, and k_0 is the radius of the normally observable region of reciprocal space. Many of these regions overlap, so there is more than one estimate of $replc_{ci}(k)$ at the same point k.

The noise-optimal way to combine such independent measurements of the same unknown is through a weighted average, in which each measurement is given a weight inversely proportional to its noise variance [11, 12]. The noise variance of $Dbar(k)$ is inversely proportional to $|otf_i(k)|^2$, and the noise-optimal weighted average becomes:

$$dr_{optimal-average}(k) = \frac{\sum_{i=1}\left[\frac{4replc_{ci}(k)}{otf_i(k)}\right]|otf_i(k)|^2}{\sum_{i=1}|otf_i(k)|^2} = \frac{\sum_{i=1} 4otf_i^*(k)replc_{ci}(k)}{\sum_{i=1}|otf_i(k)|^2}, \qquad (21)$$

where the sums are taken over all pattern orientations.

For the weighted average in equation (21), a direct linear inverse filter without regulation, is highly unstable in regions where the denominator approaches zero. To

regularize the estimate, equation (21) can be turned into a generalized Wiener filter by

introducing a Wiener parameter α^2 in the denominator:

$$dr_r(k) = \frac{\sum\limits_{i=1} 4otf_i^*(k)replc_{ci}(k)}{\sum\limits_{i=1} |otf_i(k)|^2 + \alpha^2}, \qquad (22)$$

where $dr_r(k)$ is the regularized estimate of the object image information, $Dbar(k)$,

shown in Figure 4.22. An estimate of the object in real space then can be obtained by an

inverse Fourier transform of $dr_r(k)$, after appropriate apodization.
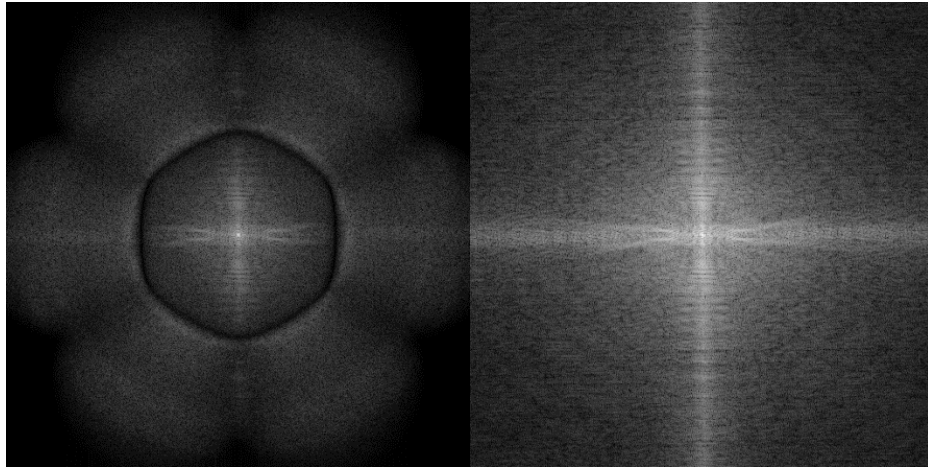
Figure 4.22. Fourier transform of reconstructed structured illumination image, $dr_r(k)$. It is an estimate of the object image information, $Dbar(k)$.

4.3.1.9 Apodization

Apodization is used in telescope optics in order to improve the dynamic range of the

image. Generally, apodization reduces the resolution of an optical image; however,

because it reduces diffraction edge effects, it can actually enhance certain small details.

In this work, the reassembled information components are apodized with a triangular

window function, $bhs(k)$, shown in Figure 4.23.
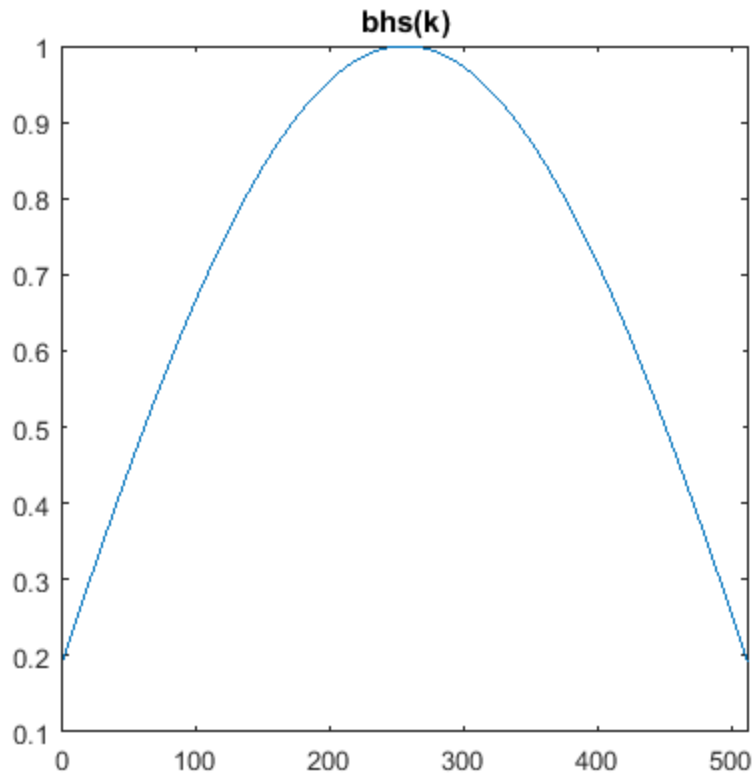
Figure 4.23. Magnitude plot of triangular function in reciprocal space, $bhs(k)$.

The cutoff frequency of the apodization function is set to 90% of the theoretical resolution limit, to account for the non-circular shape of the support region of the effective OTF.

4.3.1.10 Butterworth band-reject filtering

The diffuse ring in Figures 4.13 and 4.22 is the result of the quasi-periodic spacing of the cores in the fiberscope and it reduces the resolution of an optical image. Core spacing band is still exists. Thus, we applied a Butterworth band-reject filter to effectively

remove the honey-comb pattern, while maintaining the image quality, as shown in Figure

4.24.
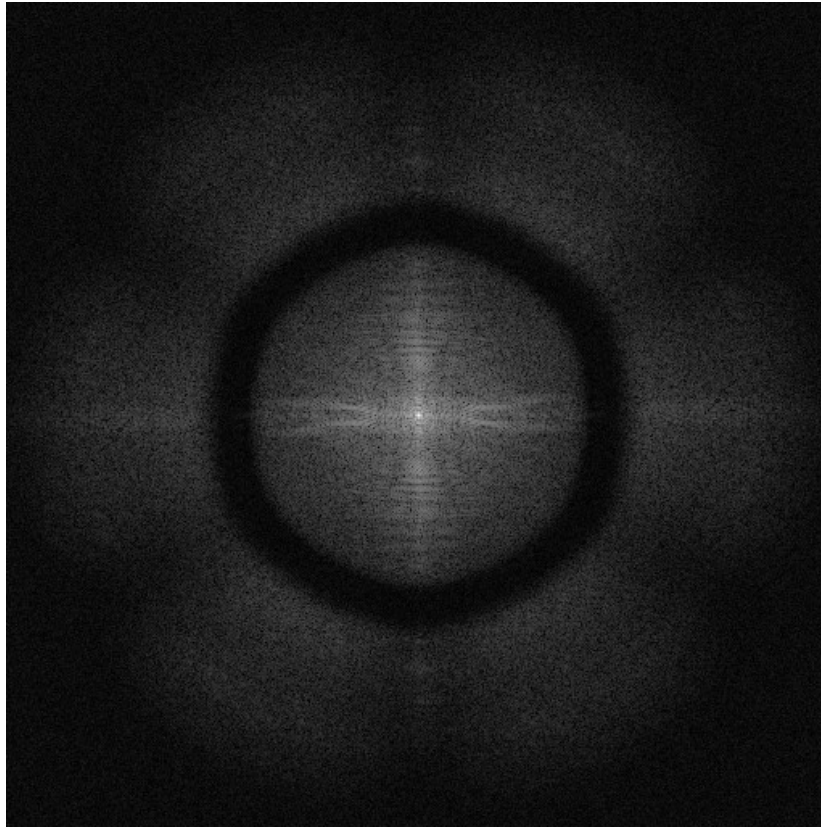
Figure 4.24. Apodized and band-rejected information components.

Finally, the apodized and band-rejected information components are inverse

Fourier transformed back to real space to obtain a high resolution reconstruction of the

object, $fimage(r)$, which is the reconstructed structured illumination fiberscope image in

real space, shown in Figure 4.25.
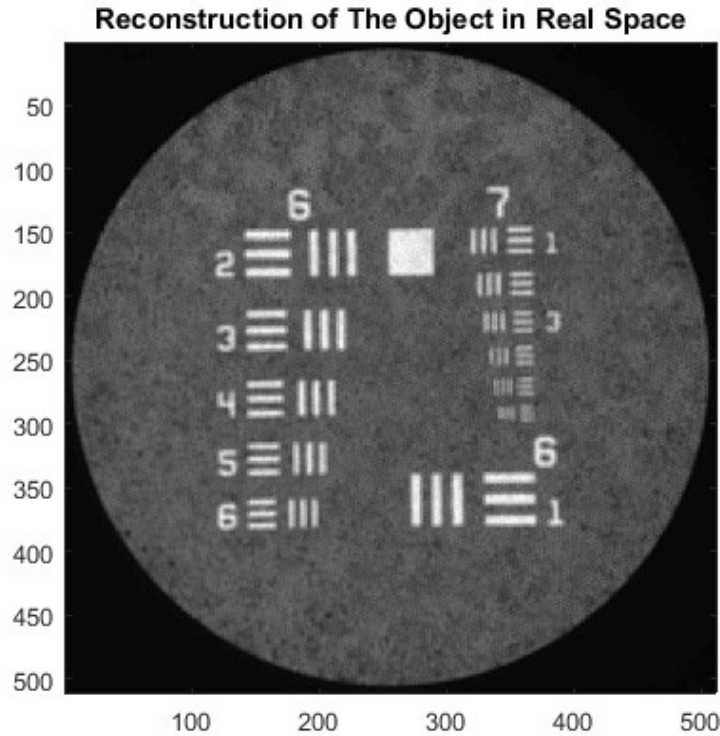
Figure 4.25. Reconstruction of SI image in real space, $fimage(r)$. It is the improved image by structured illumination technique and Butterworth Band-rejection, obtained by inverse Fourier transform of $dr_r(k)$ shown in Figure 4.24.

4.3.2   Results

4.3.2.1 USAF 1951 target

Figure 4.26 shows the result of the SIM technique and reconstruction algorithm using a

USAF target. The ROIs in the USAF target image were groups 6 and 7. The line period

of the ROIs ranged from 7.81 µm for element 1 in group 6 to 2.19 µm for element 6 in

group 7. Figure 4.26(c) is a conventional fiberscope image, and Figure 4.26(d) shows a

super-resolution image obtained using the proposed method. Figure 4.26(a) and 4.26(b)

are Fourier transforms of wide-field fiberscope and the proposed fiberscope images,

respectively. The resolution enhancement is illustrated in Figure 4.26(e) and 4.26(f).

Because all the elements in group 6 were clearly resolved in the conventional fiberscope image, we selected group 7 for the resolution test. Figure 4.26(e) shows the enlarged group 7 target images without and with the SIM technique. We plotted a line scan to show the intensity profile across the red and blue lines in each image. For plotting, the two images were first normalized, and the values were depicted to show the intensity variations. Figure 4.26(f) shows that most three lines in the elements of group 7 were clearly distinguishable when the SIM technique was applied. In contrast, the lines in the conventional wide-field illumination image could be resolved only up to the first element in group 7 due to the presence of the honey-comb pattern noise, which corresponds to a resolution of 3.91 μm. As most of the lines in element 5 in group 7 were resolved in the SIM image, the resolution was as high as 2.46 μm, which is beyond the resolution limit set by the fiber bundle core size. Furthermore, the measured SNR and peak signal to noise ratio (PSNR) were 4.2997 dB and 18.0307 dB, respectively. Thus, the SIM technique used in the reconstruction algorithm could overcome the physical limitation of data sampling imposed by the core sizes (2.9 μm) and enhance the image quality.
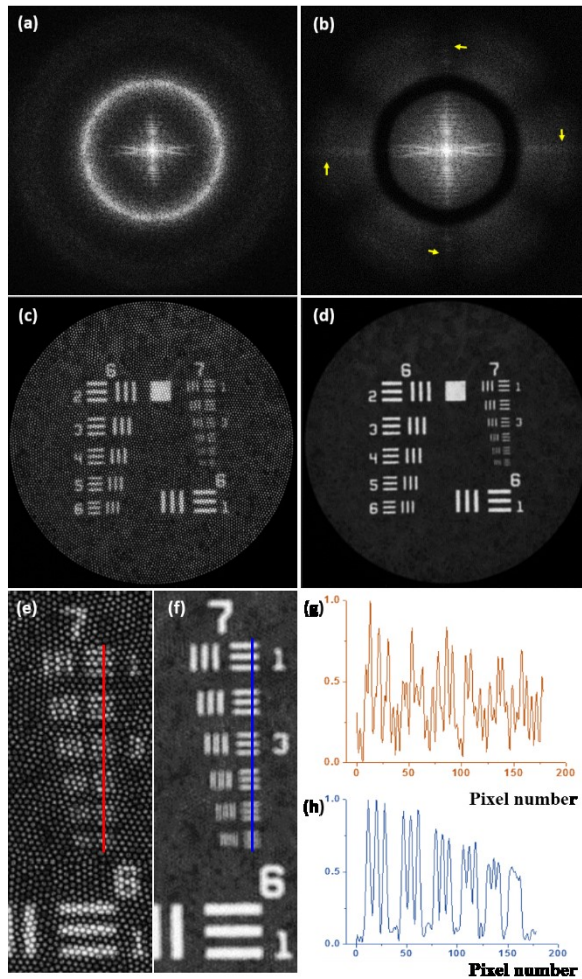
Figure 4.26. USAF 1951 target test results (yellow arrows indicate high spatial frequency components reconstructed by the SIM technique).

4.3.2.2 Purkinje cells from the cerebellum of the mouse brain

The SIM technique and reconstruction algorithm was evaluated using biological sample images. Fluorescence imaging of the Purkinje cells from the transgenic mouse brain was used to test our method. Figure 4.27(a) shows a conventional wide-field illumination fiberscope image. A dramatic improvement in the SIM image is observed (Figure 4.27(b)). As a result, individual cell bodies and axons are clearly distinguished and fine structures in the middle region are visible in the final reconstructed image. The calculated SNR and PSNR were 4.4471 dB and 13.8633 dB, respectively. This demonstrates that the

SIM technique and proposed algorithm can be effective and useful for biomedical imaging.
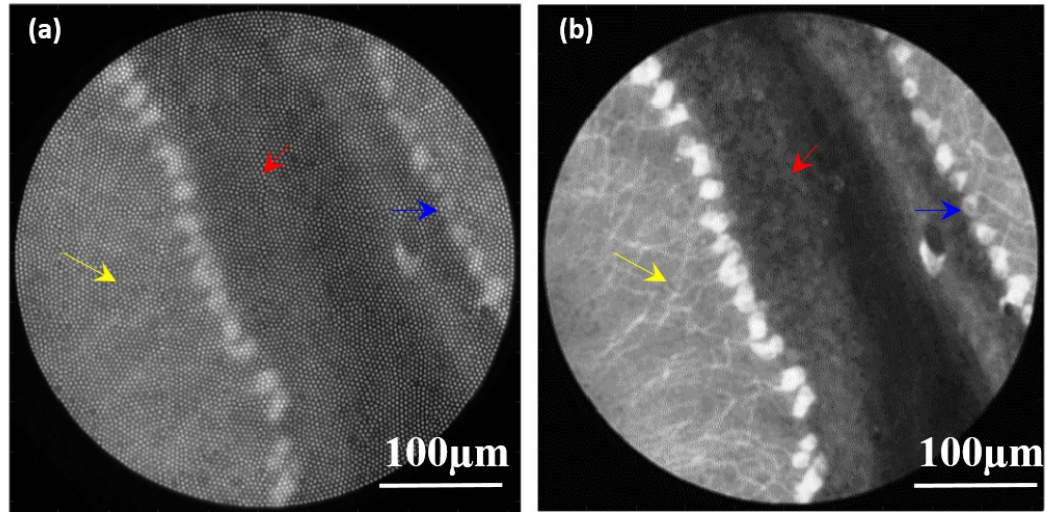
Figure 4.27. Biological sample test results.

4.3.3 Discussion

A combination of SIM and spatial frequency filtering method is proposed to enhance the resolution and improve the image quality of wide-field fiberscopy. With the USAF target and biological sample image test, the SIM technique with band-reject filtering in the Fourier domain is highly effective in improving the fiberscope imaging by eliminating the pixelation artifacts while improving image resolution.

CHAPTER 5: *IN VIVO* IMAGING OF ASTROGLIAL ACTIVITY IN FREELY BEHAVING MICE BRAIN

5.1   Background and Overview

Astrocytes (literally meaning 'star-like cells') are the most numerous and diverse neuroglial cells in the central nervous system (CNS). Astrocytes are an essential component of neural circuits and theyare extensively coupled through gap junctions and form highly interconnected networks, in which individual cells occupy distinct domains. Each cell extends highly ramified processes that ensheath synapses, contact nodes of Ranvier, and form endfeet specializations on blood vessels, placing astrocytes in an ideal position to both control the extracellular milieu and influence neuronal activity. Indeed, astrocytes have been shown to participate in diverse functions, including the clearance of neurotransmitters, maintenance of ionic homeostasis [72], hemodynamic control [73], and synaptic plasticity [74]. However, it remains unclear how astrocyte networks are controlled *in vivo* and when do these cells become engaged in the different tasks described above.

Astrocytes express a wide array of metabotropic G protein-coupled (Gq) receptors that, when activated, trigger a cascade of subcellular events that culminate in the release of Ca^{2+} from intracellular stores, allowing these glial cells to adjust their dynamical behavior in response to changes in neural activity. Ca^{2+} signaling in astrocytes has been linked to diverse phenomena, including vasodilation [73, 75] and synaptic plasticity [74, 76, 77], suggesting that the impact of astrocytes on various aspects of brain physiology is controlled by these metabotropic receptors. Nevertheless, the role of Ca^{2+} signaling in astrocytes *in vivo* remains uncertain, and mice that lack inositol trisphosphate receptor

two (IP3R2) channels that are responsible for receptor-evoked Ca^{2+} transients are overtly normal [78]. Our lack of understanding of the interaction of astrocytes with neural circuits reflects our limited knowledge of behavioral contexts in which astrocytic networks are activated. Despite the experimental evidence of astrocytic responsivity to multiple types of neurotransmitters, the pathways used to activate astrocytes *in vivo* and the patterns of activity exhibited by these cells during different behavioral states remain to be defined.

In vivo two-photon imaging using Ca^{2+}-sensitive dyes has revealed that the activity of astrocytic networks can be enhanced by local glutamatergic signaling [9, 79] or by stimulation of long-range cholinergic [80, 81] or noradrenergic neuromodulatory projections [82, 83]. How these local and global neuronal pathways interact to control the activity of astrocytic networks in awake, behaving animals has not been determined.

In this Chapter, to tackle the above-mentioned questions, transgenic mice that express the genetically encoded Ca^{2+} indicator GCaMP3 in astrocytes were used to validate the developed fiber-bundle imaging platforms that were described in Chapter 3 and to define the activity patterns of cortical and cerebellar astrocytes during distinct behavioral states.

In Section 5.2, a dual-fiber imaging probe is described to demonstrate that the increase in Ca^{2+} during arousal that accompanies locomotion promotes widespread activation of cortical astrocytic networks and enhances their response to local changes in neuronal activity.

In Section 5.3, the use of a real-time dual-color fiber-bundle imager is described for visualizing astrocytic Ca^{2+} activity in the primary visual cortex while simultaneously monitoring blood flow in the cerebral vasculature.

In Section 5.4, a long-term imaging platform that allows real-time and non-invasive imaging of the intact CNS of freely behaving animals is presented for unveiling the relationship between the activation of astrocyte networks and distinct behavioral states.

5.2   Dual-fiber Probe-based Simultaneous Imaging of Astrocytic Ca^{2+} in Multiple Brain Areas

In this Section, the spatially multiplexed fiber-bundle imager (described in Section 4 of Chapter 3) is utilized for simultaneous single-photon fiber optical imaging of the cerebellum and visual cortex. A dual fiber-optic probe reveals in mice that locomotion triggers simultaneous activation of astrocyte networks in multiple brain regions.

5.2.1   Methods
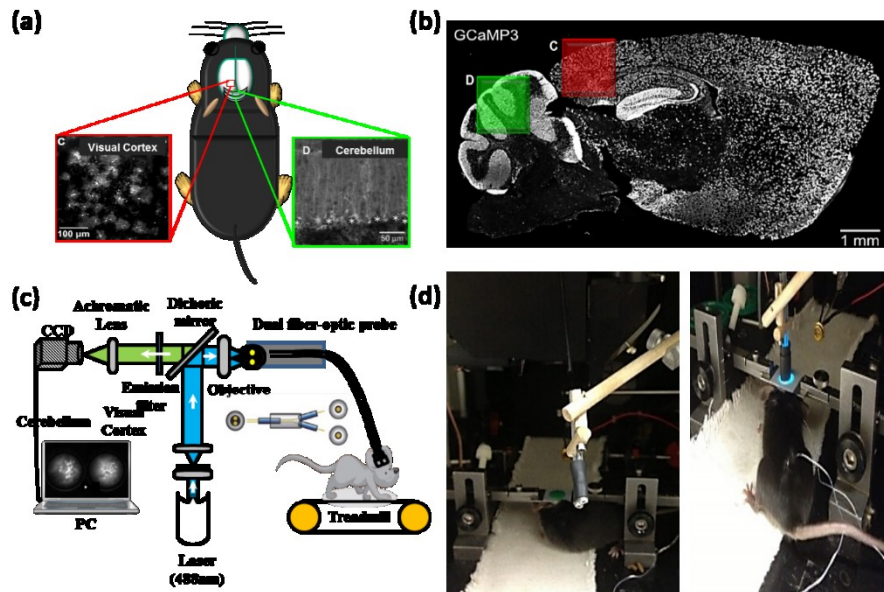
Figure 5.1. Simultaneous Ca^{2+} imaging of discrete brain regions. (a) Two target regions in the primary visual cortex (V1) and cerebellum of a mouse. (b) A sagittal plane view of the transgenic mouse (*GLAST-CreER; GCaMP3)* brain [19], (c) Schematic of the dual fiber-optic probe imaging system. (d) Photographs of the implemented system.

The distance between the optical axes of the two fiber bundles at the distal end was 3.5 mm. The excitation light from the fiber bundles was focused onto the tissue and the emitted light was collected through coupling / objective lenses placed in close proximity to the cover glass of the cranial windows (schematic in Fig. 5.1(c)). The microscope characteristics were as follows: the laser wavelength was 488 nm, OBIS488LS 20 mW, Coherent; a 10x beam expander, BE10M-A,Thorlabs; a dichroic mirror, FF499-Di01-25x36, Semrock; an objective lens, Plan 4x/0.10 NA Olympus; fiber bundles with the field of view diameter in the 600–650 μm range, FIGH-30-650S, Fujikura; a coupling/objective lens, a pair of aspheric lens, 352140-A/0.55NA, Thorlabs; a green fluorescent protein (GFP) emission filter; a focusing lens, an achromatic doublet lens,

AC254-150-ML-A, Thorlabs; a charge-coupled device (CCD) camera, GS2-FW-14S5M, Point Grey Research.

5.2.2 Ca^{2+} activity in cerebellar Bergmann glia during locomotion

Locomotion has been shown to trigger transient increases in intracellular Ca^{2+} in Bergmann glia [9]. This activity, visualized acutely with a Ca^{2+} indicator dye, was shown to extend over large areas of the cerebellum, requiring local activation of glutamate receptors. To define the mechanisms underlying the engagement of this glial network, we trained GCaMP3-expressing mice to walk on a treadmill and monitored locomotion-induced Ca^{2+} levels in Bergmann glia. In accordance with previous findings [9], brief bouts of locomotion were often associated with widespread increases in Ca^{2+} in Bergmann glia that persisted for many seconds after the cessation of locomotion.

To provide an independent measure of motor activity in these mice, muscle contraction was monitored during imaging trials. Post hoc analysis of electromyogram (EMG) recordings revealed that ''spontaneous'' Ca^{2+} transients that occurred in the absence of locomotion were often associated with an increase in the EMG power, suggestive of startle behavior.
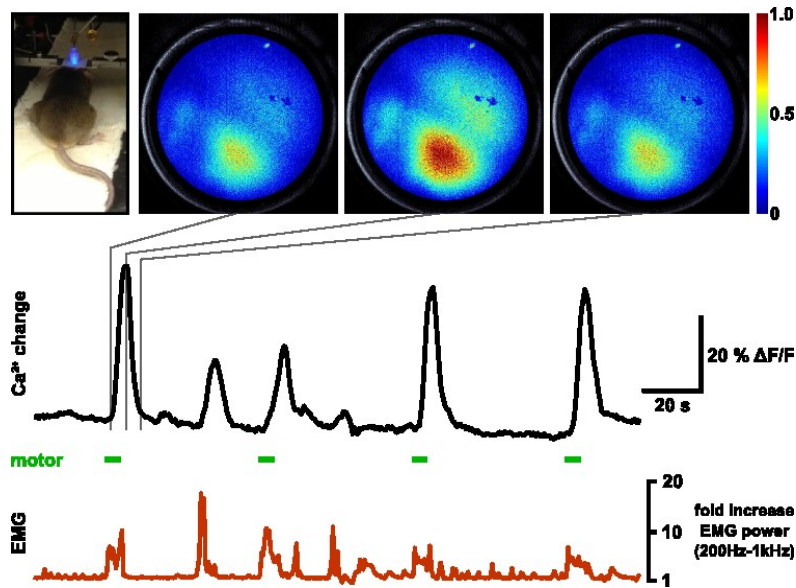
Figure 5.2. Imaging astrocytic Ca^{2+} transients *in vivo* using an optical fiber. (Top left) A photograph of a mouse that was head-fixed on a treadmill while Bergmann glial Ca^{2+} responses were imaged by using the optical fiber. (Top right panel) Pseudo-colored images of changes in the GCaMP3 fluorescence (= an increase in the intracellular Ca^{2+}) in cerebellar Bergmann glia during locomotion. (Middle panel) GCaMP3 fluorescence vs. time. Green bars indicate the treadmill activation periods. This manipulation activates the locus coeruleus, resulting in the release of norepinephrine in the cerebellum and activation of metabotropic receptors on Bergmann glia. (Bottom panel) EMG recorded from the flank of the animal, showing the correlation between muscle contraction and Ca^{2+} changes in Bergmann glia.

5.2.3   *Astrocytes Ca^{2+} Activity in Primary Visual Cortex (V1) during Locomotion*

Noradrenergic neurons in the brainstem nucleus locus coeruleus (LC) extend axon collaterals diffusely throughout the brain, providing the means to exert control over the brain activity states. To determine whether locomotion-induced engagement of the noradrenergic system results in the brain-global activation of astrocytes, astrocytic Ca^{2+} levels in the primary visual cortex (V1) were also monitored during locomotion.
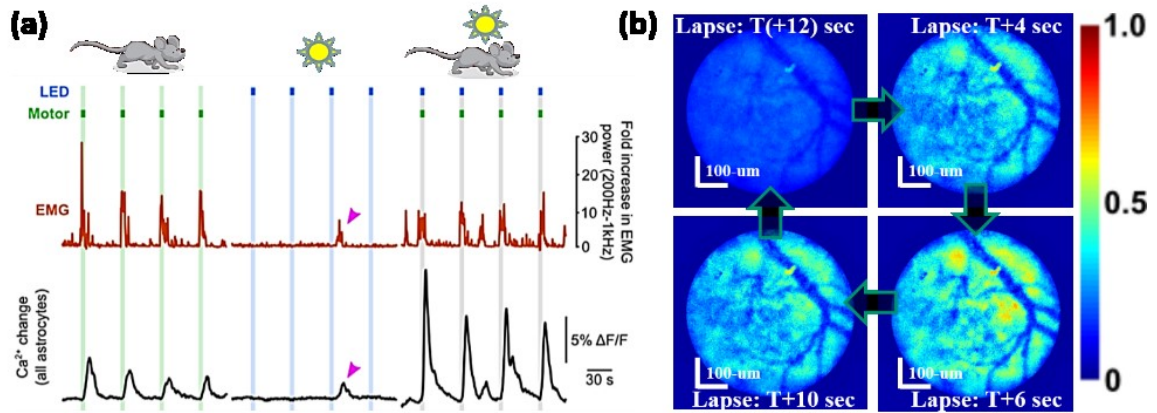
Figure 5.3. (a) Ca^{2+} responses of V1 astrocytes to enforced locomotion (green bars), visual stimulation (blue bars), and simultaneous enforced locomotion and visual stimulation (gray bars) [19]. Red traces represent EMG activity; black traces represent the mean Ca^{2+} change. The pink arrowhead highlight the Ca^{2+} elevation associated with spontaneous locomotion. (b) Imaging of V1 astrocytes by using an optical fiber-bundle. *T* is the treadmill activation time.

Remarkably, in complete darkness, enforced locomotion reliably elicited Ca^{2+} transients in V1 astrocytes, with the time course of response similar to that observed in cerebellar Bergmann glia.

5.2.4 *Simultaneous Imaging of Ca^{2+} in the Cerebellum and Visual Cortex during Locomotion*

To assess the relative timing and spatial extent of changes in the astrocytic activity, a dual fiber-optic imaging system was used to monitor GCaMP3 fluorescence simultaneously in different brain regions. When fiber-optic probes were positioned over cranial windows implanted above the visual cortex (V1) and cerebellum (lobules simplex), coincident Ca^{2+} elevations were detected in both astrocytes and Bergmann glia in response to voluntary and enforced locomotion. The magnitude of Ca^{2+} changes in these two regions covaried (correlation coefficient = 0.756, p < 0.001; N = 348 events from 6 mice), suggesting that

amplitude fluctuations primarily reflect different levels of activity of noradrenergic neurons (Fig. 5.4).

Although in both regions the responses were initiated at the same time (response onset delay in the cerebellum = 1.93 ± 0.13 s; response onset delay in V1 = 1.91 ± 0.10 s, 348 events from 6 mice, p = 0.8982), consistent with the minimal delay attributed solely to axonal conduction delays (~40 ms, assuming a conduction velocity of 0.5 m/s and an additional distance of 20 mm to V1), Ca^{2+} transients in the visual cortex peaked 1.6 ± 0.2 s later than Ca^{2+} transients in the cerebellum (p < 0.001), raising the possibility that local circuit activity modifies the timing of astrocyte recruitment.
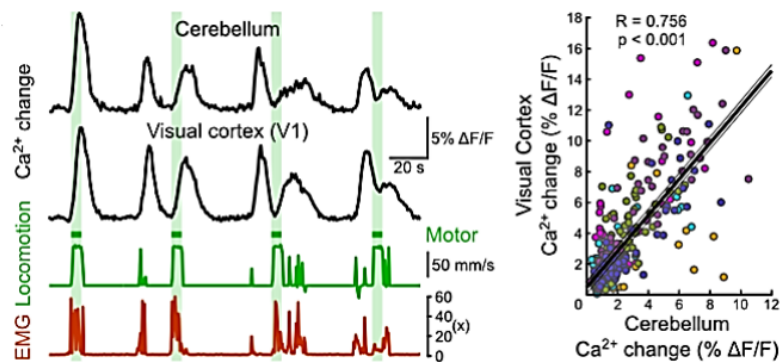
Figure 5.4. Locomotion induces simultaneous activation of astroglia in different brain regions [19]. (Left) Ca^{2+} responses of Bergmann glia and V1 astrocytes visualized simultaneously during enforced locomotion (green bars) and corresponding EMG activity. (Right) Covariance of Ca^{2+} responses of Bergmann glia and V1 astrocytes during spontaneous locomotion. N = 348 spontaneous locomotion events from 6 mice. Black lines represent mean ± SEM of 6 regression lines.

5.2.5   Discussion

These studies indicate that astrocyte networks have a high threshold for activation in periods of quiescence and suggest that recruitment of the noradrenergic system is

required to enhance the gain of these networks to enable local interactions between astrocytes and neurons in circuits involved in processing sensory information. The activation of astrocytes in V1 by norepinephrine during locomotion parallels recent *in vivo* electrophysiological studies indicating that locomotion triggers norepinephrine-dependent depolarization of neurons in V1 [84]. In contrast to neuronal activation, which began within 50 ms of locomotion onset, Ca^{2+} transients in astrocytes began more than a second later (1.4 ± 0.1 s, n = 106 events from 13 mice), presumably reflecting the additional biochemical steps required to release Ca^{2+} from intracellular stores.

Optical cross-talk between the fiber bundles was minimal: The coupling / objective lens pairs had a diameter of 2.4 mm and a working distance of 0.88 mm. Thus, with a distance of 3.5 mm separating the optical axes of the two fiber bundles, capturing light from the other structure would be very inefficient. If such a cross-talk occurred and Ca^{2+} responses in the cerebellum and visual cortex did not co-vary, it would be expected that many instances of small responses recorded by one probe would accompany robust responses recorded by the other. In addition, if a possible cross-talk between the fibers caused co-variation, responses measured by using the two fibers should have had the same kinetics; however, while the two signals did not significantly differ in their onset times, the signal recorded from the visual cortex peaked significantly later than the signal recorded from the cerebellum.

5.3 Simultaneous Functional Imaging of Astrocytic Ca^{2+} Signals and Blood Flow using a Real-time *In Vivo* Dual-color Fiber-bundle Fluorescence Imager

In this Section, a novel dual-color wide-field fiber-optic fluorescence microscope that allows real-time, achromatized, and high-resolution cellular imaging, is presented. The system uses a 650-µm-diameter multicore fiber bundle with a 2-mm-diameter achromatic imaging optical system capable of operating simultaneously at 488- and 532-nm excitations. To provide the imaging in real time, a custom software was developed, capable of co-registering two-channel fluorescence images from a dual CCD camera detection system and offering merged images at a video rate reaching 30 frames/s. The system performance was evaluated by *in vivo* functional brain imaging of astrocytic Ca^{2+} signals and blood flow in head-fixed live mice.

5.3.1 Methods

5.3.1.1 System design

The system setup is shown in Fig. 5.5. The system simultaneously used two excitation wavelengths of 488 nm (OBIS488LX50, Coherent) and 532 nm (DJ532-40, Thorlabs). The two excitation beams were combined by using a dichroic mirror (Di02R488, Semrock), and were coupled into a 30,000 core fiber bundle (FIGH-30-650S, Fujikura) by using a quad-edge laser-flat dichroic mirror (Di01-R405/488/532/635, Semrock) and a microscope objective (Plan 10X/0.25, Olympus). The distal end of the fiber was connected to a custom optical imaging system consisting of a pair of 2-mm-diameter achromatic doublet lenses (#65-567, Edmund Optics), enclosed by a custom-built lens housing (see Fig. 5.6) The light emitted by the sample passed back via the same route. The fluorescence signals were separated by a dichroic mirror (DMLP567L, Thorlabs) and

filtered both for green and red channels by individual emission filters (MF530-43, FB600-40, Thorlabs). A cold silver mirror with a right-angle kinematic mount (KCB1, Thorlabs) was used in the green channel to restore a horizontally flipped image, thus allowing co-aligned imaging. Two spatially overlapping but fluorescent probe-specific 640 × 480 pixel images were captured by two synchronized dual monochrome CCD cameras (FL2-03S2M, Point Grey Research). The two cameras were automatically synchronized to each other at the hardware level, were on the same IEEE-1394 bus, and had the same frame rate.
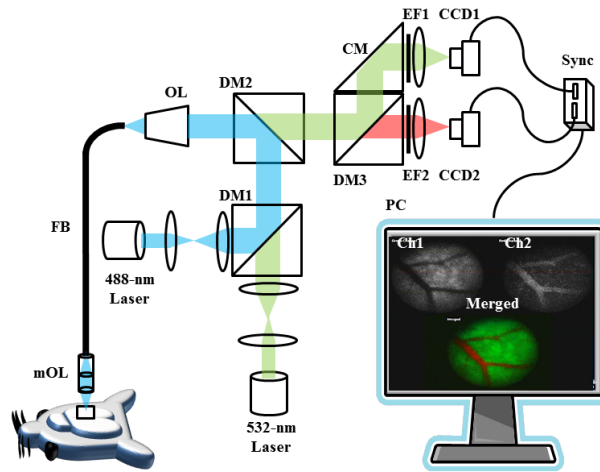
Figure 5.5. Schematic of the system setup: DMs: Dichroic mirrors, OL: Microscope objective, FB: Fiber bundle, mOL: Miniature objective, CM: Cold mirror, EFs: Emission filters.

5.3.1.2 Design and fabrication of the achromatic imaging probe

Two lens imaging is a well-known technique that is widely used in various imaging optical systems [85]. Matching achromatic doublet lens pairs yielded minimal spherical aberration with the added benefit of correcting chromatic aberration. The imaging probe was particularly designed to provide dual-color (GCaMP3 and Rhodamine-Red) *in vivo* brain imaging of a live mouse through the implanted cranial window. To image through a

4 mm^2-area cranial window (thickness: 100 μm) implanted over the primary visual cortex (V1) of a mouse, the probe required a working distance of 1 mm and a field of view diameter of 400 μm. In the previous work, the dual-lens imaging probe was described based on the geometrical optics model [19]. The prototype design is shown in Fig. 5.6.
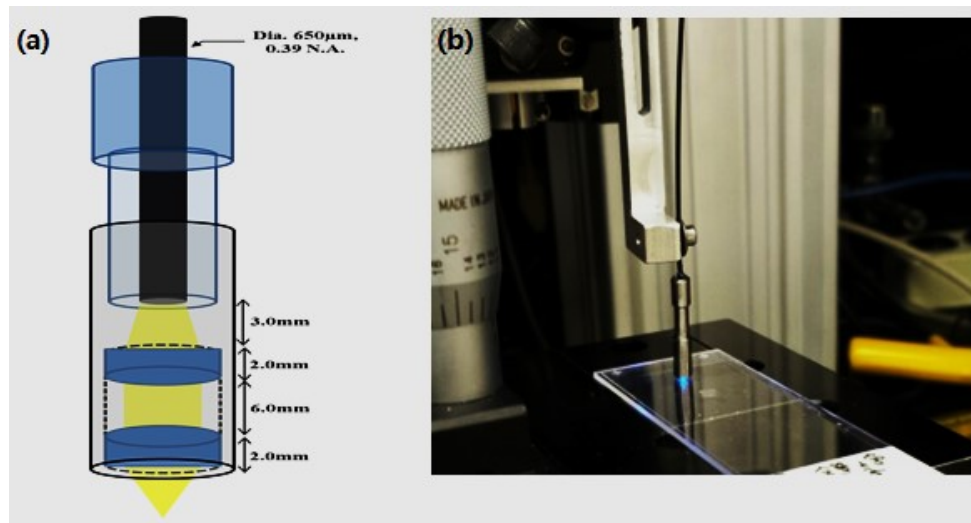
Figure 5.6. (a) Achromatic doublet pair imaging probe. (b) A photograph of the prototype.

To optimize the design parameters, the achromatic doublet lens pair was numerically modeled by using Zemax (OpticStudio 14.2, Zemax). Figure 5.7 shows the predicted spot diagrams of the design, for three different wavelengths. Three wavelengths of 0.48, 0.55, and 0.63 mm were tested based on the excitation/emission spectra of GCaMP3 and rhodamine dye (GCaMP3 exhibits an excitation peak at 490 nm and emission peak at 514 nm; rhodamine dye exhibits an excitation peak at 570 nm and emission peak at 590 nm). At the center wavelength of 550 nm, an NA 0.33 achromatic doublet lens pair imaging system provided a diffraction-limited resolution of 4.837 μm. The focal length shift varied within 0.4 μm (Fig. 5.7.) After fabricating the imaging probe, the magnification factor became approximately 1:1.75, resulting in the lateral resolution of 2.764 μm.
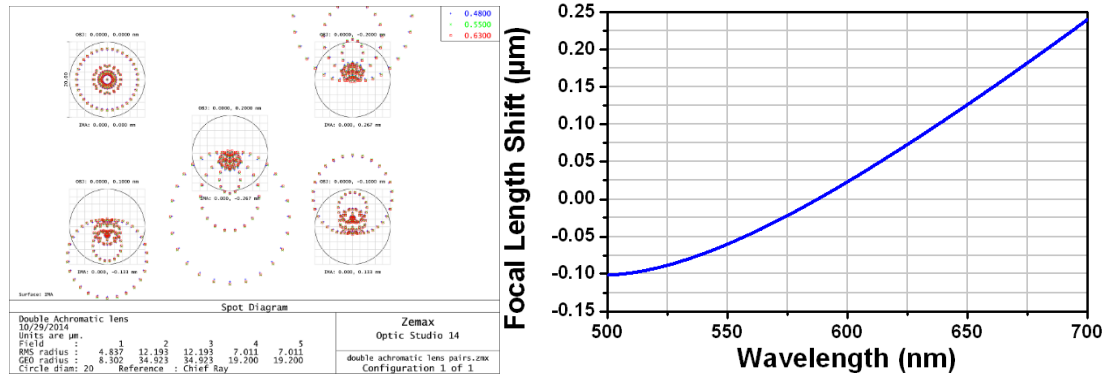
Figure 5.7. Zemax simulation results. (a) Beam spot size in the image plane. (b) Chromatic distortion.

5.3.1.3 Software development

The graphical user interface, data acquisition, and control software were programmed using visual C# .net framework (Visual Studio 2010, Microsoft) on a desktop PC with Intel® Core™ i5 CPU 650 @ 3.2 GHz with 8 GB RAM. To efficiently process a large amount of continuous image streams of the two synchronized dual monochrome CCD cameras, a multi-threaded parallel processing technique was adopted [86]. Specifically, three independent threads were used to retrieve raw data from the two cameras, subtract background images and display processed images in the graphical user interface (GUI), as shown in Fig. 5.8. Compared with single-threaded processing that would retrieve and process the captured images from the two cameras sequentially, the multi-threaded processing enabled the system to manage the image data from the two cameras simultaneously. Thus, the second camera did not need to wait for the completion of the first camera's processes. This becomes crucial when imaging involves large image sizes, heavy image-processing procedures, or multiple cameras having different frame rates. In particular, when the two channels have different fluorescence signal levels, having separate threads allows for independent averaging and integration time, thus enabling

107

dual-channel image equalization. In addition, in a single-threaded process, the total

system performance is decided using the slower camera and the system misses the images

acquired by the faster camera. By contrast, a multi-threaded system can simultaneously

manage both cameras and update the merged image according to the actual image

changes. During the image processing stage, the 8-bit raw image data acquired by the

cameras were subtracted from the background image and then were merged into each red

or green color of a 24-bit merged image. The third thread updated the three display

windows in the GUI triggered by a signal that was generated whenever the merged image

was updated. The three memory blocks for the three types of images in the dotted red

square in Fig. 5.8 were shared by the three threads and protected, to prevent overwriting

during the memory reading. Therefore, this system utilizes the mutual exclusion

algorithm (Mutex) to allow only one thread at a time to access the shared resource [87].
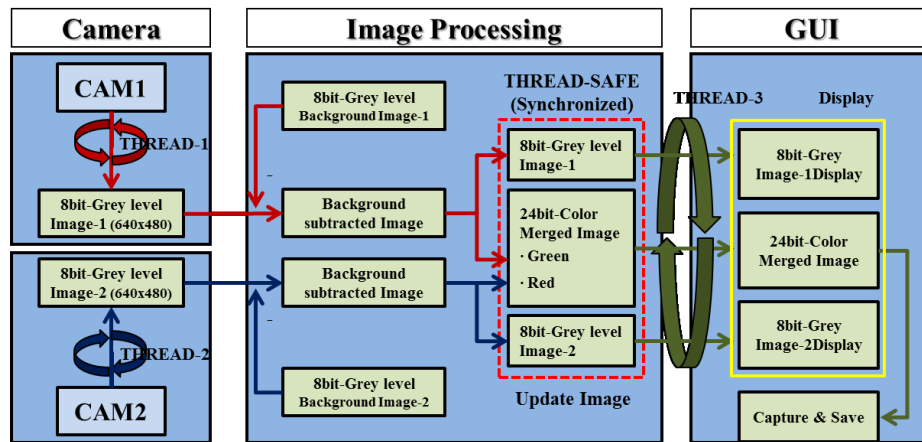
Figure 5.8. Schematic overview of the real-time dual-channel image acquisition and the
computation pipeline of merged images (Blue boxes: camera capture, image processing, and
windows form classes; Green boxes: data types used in the program; [CamID]: Camera ID, [W x
H]: 640 x 480 pixels, dashed arrows: data flow).

5.3.1.4 Animal protocols

All procedures were approved by the Johns Hopkins University Animal Care and Use Committee. Cre recombinase-conditional GCaMP3 mice were generated in the previous study [19]. A genetically encoded Ca^{2+} indicator, GCaMP3, was expressed in astrocytes to image Ca^{2+} signals.

For *in vivo* studies, all animal surgeries were performed under aseptic conditions. The animals were anesthetized with 1.5–2% isoflurane in 95% oxygen. The animal head was shaved, cleaned by using 70% ethanol and betadine, following which a scalp incision was made and small craniotomy was performed using a dental drill with the stereotaxic apparatus. Then, a coverslip (area: 4 mm^2; thickness: 100 µm) was placed over the craniotomy region and secured with cement. Next, a head plate was cemented to the animal skull. After the surgery, the animal head was immobilized by using a custom-designed head-fixation stage. To image the blood flow, the dextran-conjugated rhodamine dye (#R9379, Sigma-Aldrich) was dissolved into a 0.3% saline solution and injected into the tail vein. The laser power was optimized to 0.4 mW/mm^2 to prevent brain tissue from damaging. The tip of the imaging probe was positioned over the 4-mm^2–area cranial window by using micromanipulators. The duration of individual episodes of *in vivo* imaging never exceeded 1 min.

5.3.2   Simultaneous Functional Imaging of Astrocytic Ca^{2+} Signals and Blood flow in the Visual Cortex of Awake, Head-fixed Mice

The system performance was evaluated in *in vivo* imaging of GCaMP3 and rhodamine dye fluorescence in transgenic head-fixed mice. Astrocytic Ca^{2+} activity in the visual cortex was imaged while simultaneously monitoring rhodamine-dextran labeled blood

vessels to observe the flow of red blood cells (Fig. 5.9) Because global Ca^{2+} activity in astrocytes can be evoked by arousal events [9], three air puffs were delivered during each imaging session [88]. In Fig. 5.9, pseudo-colored astrocytes are readily visible (green) near the blood vessels. Photometric Ca^{2+} changes are clearly observable. In the red channel imaging, the flow of red blood cells through the vessel was visualized.
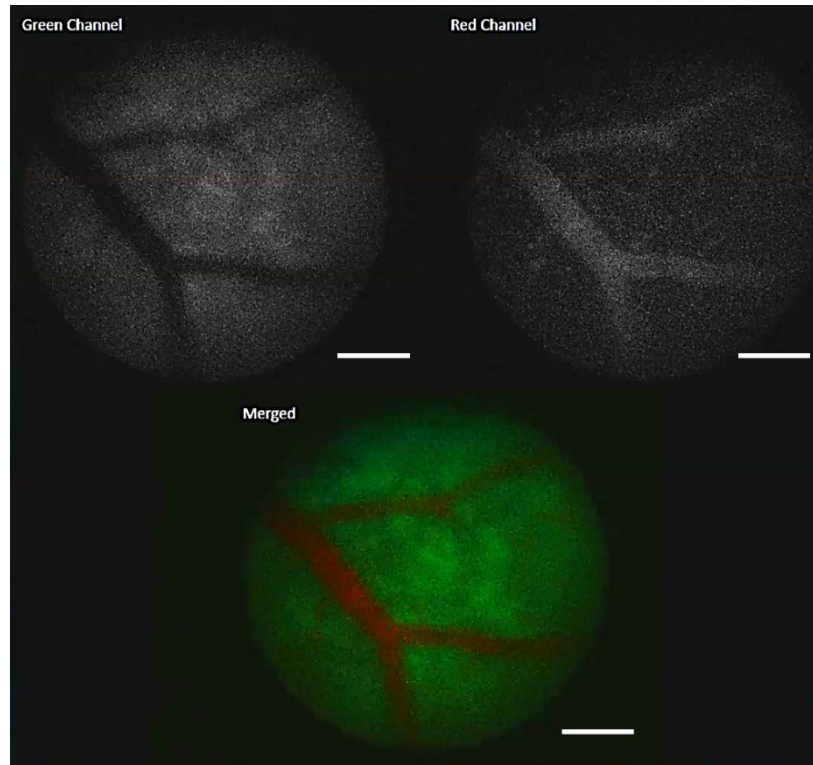
Figure 5.9. Dual-color functional brain imaging in live mice. The white scale bar corresponds to 100 μm.

5.3.3 Discussion

In this Section, real-time dual-color imaging of fluorescence signals *in vivo* was demonstrated by using a fiber-optic bundle fluorescence microscope. Potential technical improvements include the use of a spatial filter to limit the off-axis auto-fluorescence lights or SLM microscopy, introduced in Chapter 4, of which the latter enables either

structured illumination or scanless confocal imaging, while maintaining high-speed data acquisition [70, 89-91].

The dual-camera detection system provides the spatial, temporal, and optical resolution needed for capturing high-quality images in biomedical applications. This dual-color imaging system could have applications in other areas, such as ratiometric Ca^{2+} imaging [58]. In addition, the same system can be employed for imaging neural activity in *in vivo* experiments on mice expressing ultrasensitive fluorescent Ca^{2+} sensor proteins, such as GCaMP6 or RCaMP [7, 59].

Astroglia are central to the neurovascular coupling that couples neural circuitry to a local blood flow and metabolic support [92]. The basal lamina of blood vessels is almost entirely covered by astrocytic endfeet. This astrocytic activity leads to the release of vasoactive agents that regulate the local blood flow. Therefore, astrocytes can be viewed as neurovascular bridges. In our experiments, Ca^{2+} increases in astrocytes were always linked to blood flow changes, indicating neurovascular coupling.

5.4 Behaviorally-relevant Astrocyte Network Activation within the Brain in Freely Behaving Animals

In this Section, we describe a novel imaging platform that allows to probe the correlation between the brain activity and behavior in freely moving mice. The system utilizes a fiber-bundle based fluorescence microscope for long-term imaging of cellular activity in the mouse brain and simultaneous monitoring of the corresponding animal behavior by using near infrared (NIR) cameras. Taking advantage of this novel imaging platform and transgenic mice, we demonstrate that astrocytes, which are usually considered to be passive supporting cells, can play an active role in mammalian brain.

5.4.1 Methods

5.4.1.1 System setup

The novel imaging platform utilized two NIR cameras (FI8910W, Foscam US) for 24-h-long tracing of animal motion, and a fiber-bundle based fluorescence microscope for imaging cellular activity in the brain. The fiberscope used a 0.5 mW, 488 nm laser (OBIS488LX, Coherent) triggered by an analog modulation (NI-USB 6009, National Instrument), and a 30,000 cores, 650-µm-diameter multicore coherent fiber bundle (FIGH-30-650S, Fujikura). The laser beam was expanded by a beam expander and was reflected off a dichroic mirror (DMLP490R, Thorlabs). The incident laser beam was then coupled to the fiber bundle by using a microscope objective lens (Plan N 10X/0.25 N.A., Olympus). The distal tip of the imaging probe consisted of a 2.4-mm-diameter aspheric lens pair (352140-A, Thorlabs) and a custom-built lens housing (Fig. 5.10(b)). The fiber-optic probe was positioned on a 1-mm^2-area cranial window by using a custom built head-mount setup without touching the brain tissue (Fig. 5.12(b)). Fluorescent light from

the brain was collected by the same fiber and passed back via the same microscope objective lens, the dichroic mirror and the emission filter (MF525/39, Thorlabs). The resultant fluorescence signal was detected by using a CCD camera (GS2-FW-14S5M, Point Grey Research).
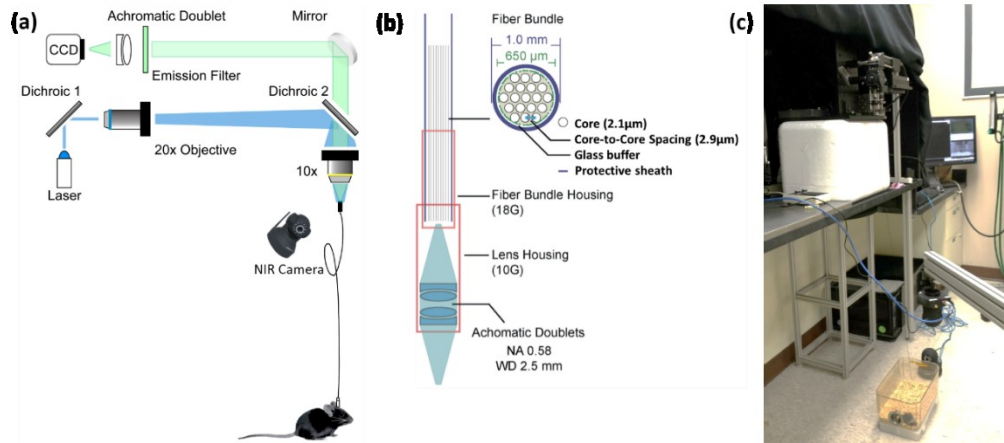
Figure 5.10. System configuration. (a) Optical layout. (b) Imaging probe design. (c) A photograph of the system implementation.

5.4.1.2 Animal protocols
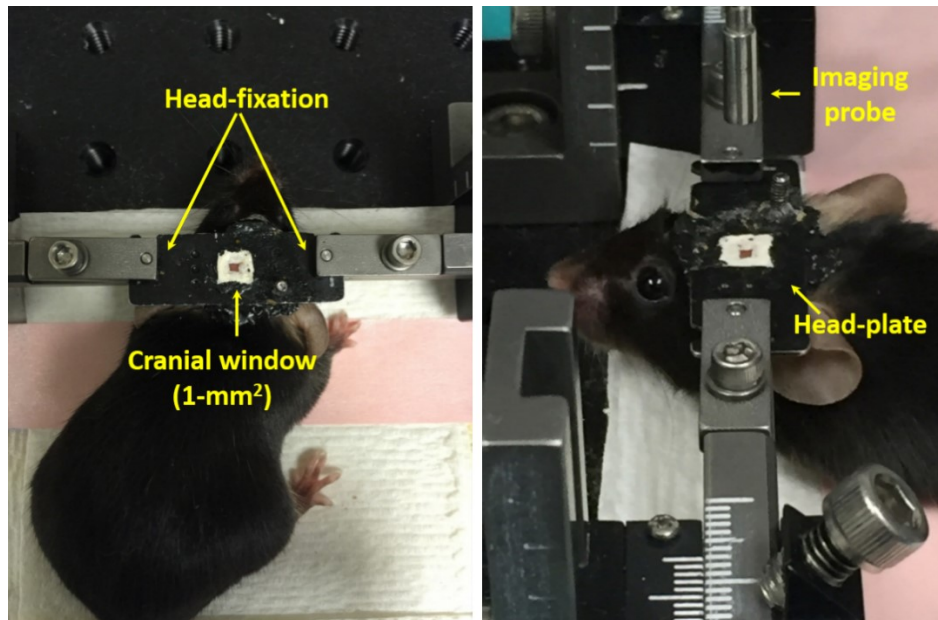
Figure 5.11. Head fixation using a custom-built head plate.

For *in vivo* studies, all procedures were in compliance with the protocols approved by the

Animal Care and Use Committee at Johns Hopkins University. Animal surgeries were

performed under aseptic conditions. The animals were anesthetized by injecting ketamine

(100 mg/kg) and xylazine (10 mg/kg). The animal head was shaved, cleaned by using

70% ethanol and betadine, following which a scalp incision was made and small

craniotomy was performed using a dental drill with the stereotaxic apparatus. After the

surgery, the fiber-optic imaging probe was fixed on the 1-mm^2-area cranial window by

using x-y-z micromanipulators and fixed by using the head mount setup. Data from the

cameras were acquired simultaneously, at a sampling rate of 2 Hz (integration time: 500

ms) for the brain activity and 30 Hz for the animal motion.
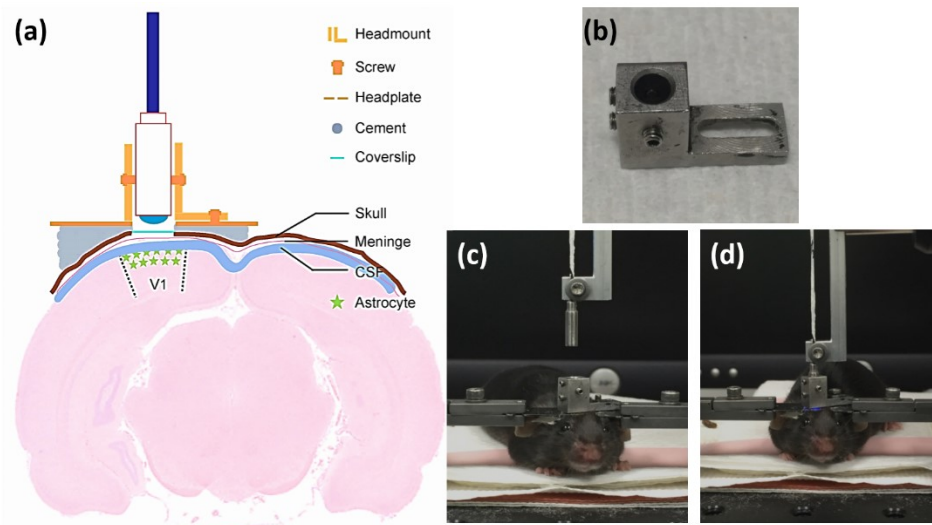
Figure 5.12. The head mount setup. (a) Schematic of the head mount. (b) A photograph of the head mount. (c) Fiber-optic coupling to the head mount by a micromanipulator. (d) The head mount and the optical fiber.

5.4.1.3 Software development

All of the devices were synchronized and controlled by using a custom-built *BrainImage*

PC program (Visual Studio 2010, Microsoft). When the program started, the system

triggered the laser operation for 1 min every hour, and the cameras simultaneously

recorded the brain activity and animal motion data for 1 min of the laser operation. Figure

5.13 shows the GUI of the developed program for controlling the system. The program

layout consists of three windows: functional brain imaging (left), animal motion 1 (top

view), and animal motion 2 (front view). When the program triggers the laser and the

cameras start to record data, the on-air button (red circle) and green color background are

activated, while the recording button and the background color are darkened (implying

deactivation) during the dormant period. All the brain images are saved in the

BrainImage root folder on the PC hard drive, and the synchronized motion .mp4 codec

videos are saved in the program folder in series according to the measurement time

sequences. For future analysis, all raw data were saved with corresponding time-stamps

to align the sequences.
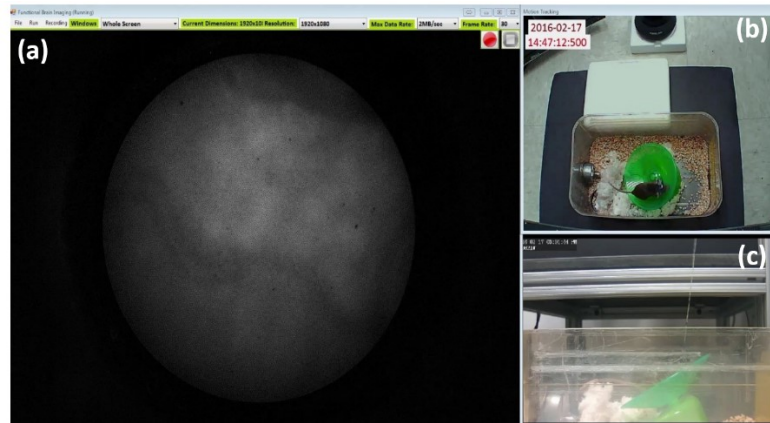
Figure 5.13. *BrainImage* PC program (a) Graphical User Interface, (b) Animal motion tracking 1
(top-view), (c) Animal motion tracking 2 (front-view)

5.4.1.4 Image analysis

Data were processed and analyzed in MATLAB (Matlab 2014a, Mathworks). Cellular

activity ($\Delta F/F$ fluorescence intensity) traces report $(F-F_{median})/F_{median}$, with F representing

the fluorescence averaged over all pixels within the region of interest (ROI) of one image frame and F_{median} representing the median F of all image frames.

5.4.2 Results

5.4.2.1 System characterization

The system was characterized by imaging standard resolution test targets. As shown in Fig. 5.14(a), the measured field of view (FOV) was 462 μm in diameter. The lateral resolution was ~3.48 μm (Fig. 5.14(b)). The axial response was tested by using 4-μm-diameter fluorescent beads. The measured axial resolution at full width half maximum (FWHM) was 47.92 μm.
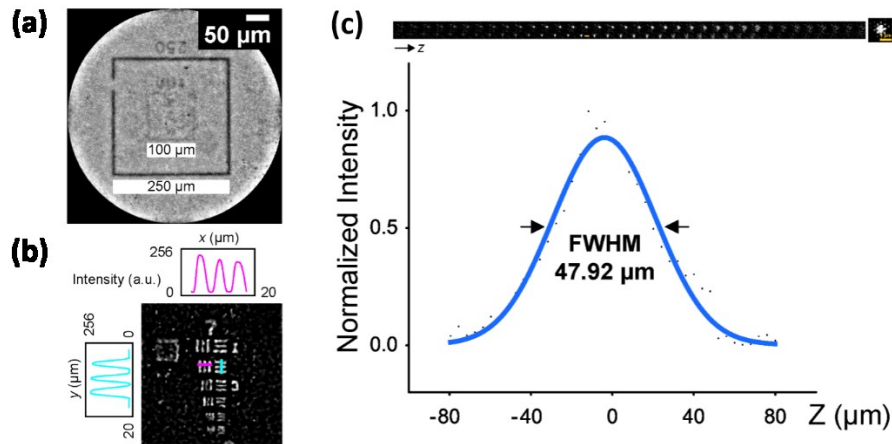
Figure 5.14. System characterization. (a) Field of view (FOV). (b) Lateral resolution. (c) Axial resolution.

The system performance was also tested by *in vitro* and *in vivo* brain imaging of transgenic mice. As is seen from Fig. 5.15, both GFP and GCaMP3 fluorescence were captured by using the proposed imaging system. The fluorescent astrocytes were clearly resolved and in accordance with the previous findings, astrocytic Ca^{2+} signals were

successfully detected during enforced locomotion while GFP signals were constant (Fig. 5.15).
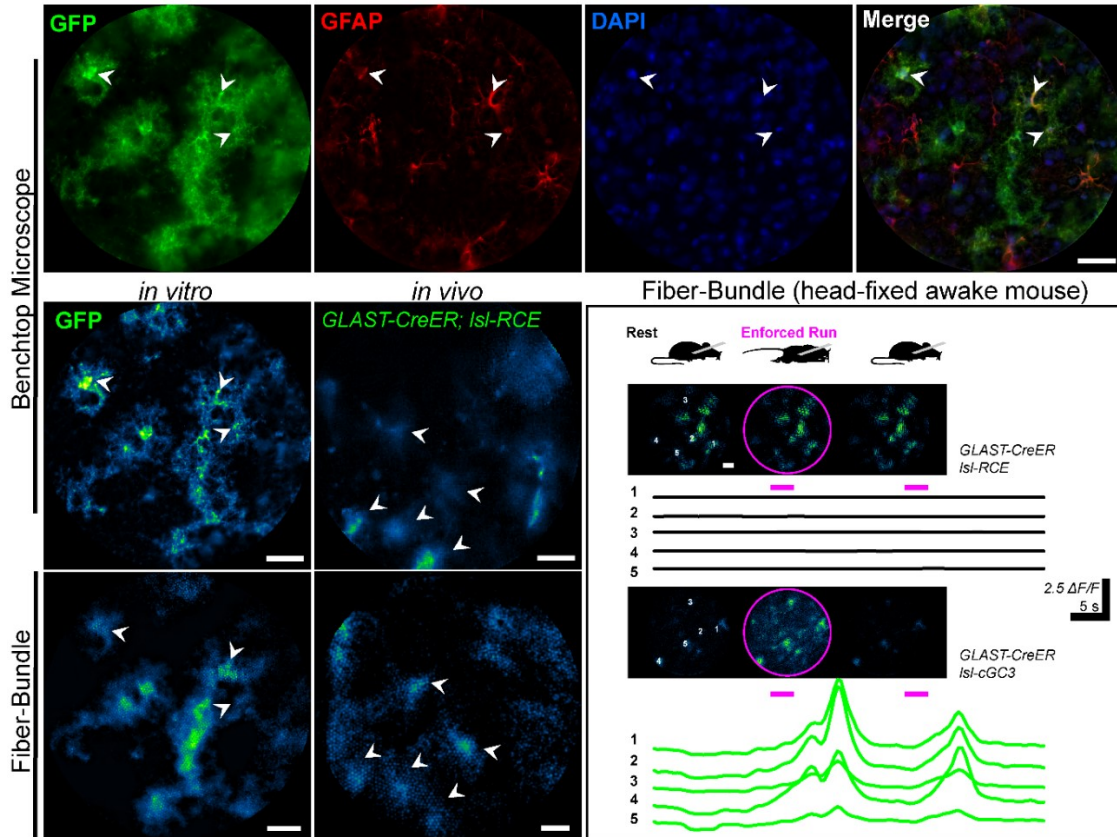
Figure 5.15. Testing the system performance by *in vitro* and *in vivo* imaging. (Top panel) Results of bench-top microscope imaging. (Lower left panels) Fiber-bundle images. (Lower right panels) Comparison between GFP and GCaMP3 fluorescence signals during enforced locomotion; fluorescence signals were constant in GFP mice while wide-spread elevations of Ca^{2+} were observed in GCaMP3 mice.

5.4.2.2 In vivo freely moving animal brain imaging and long-term data analysis

Figure 5.16 illustrates an example of behaviorally relevant astrocyte activity in freely moving mice. As shown in Fig. 5.16, when the animal stirred its head, "spontaneous" Ca^{2+} transients occurred in the absence of locomotion, which was not observable in head-

fixed animal brain imaging. The corresponding brain activity (Ca^{2+} signal) is shown in the middle panel of Fig. 5.16. By retaining these data sample plots for 24 h, we were able to categorize and compare distinct animal behaviors (such as eating, drinking, sleeping, and running) with specific brain activity patterns. Interestingly, astrocytic Ca^{2+} fluorescence signal during sleep remained mostly constant and exhibited minimal oscillations (Fig. 5).
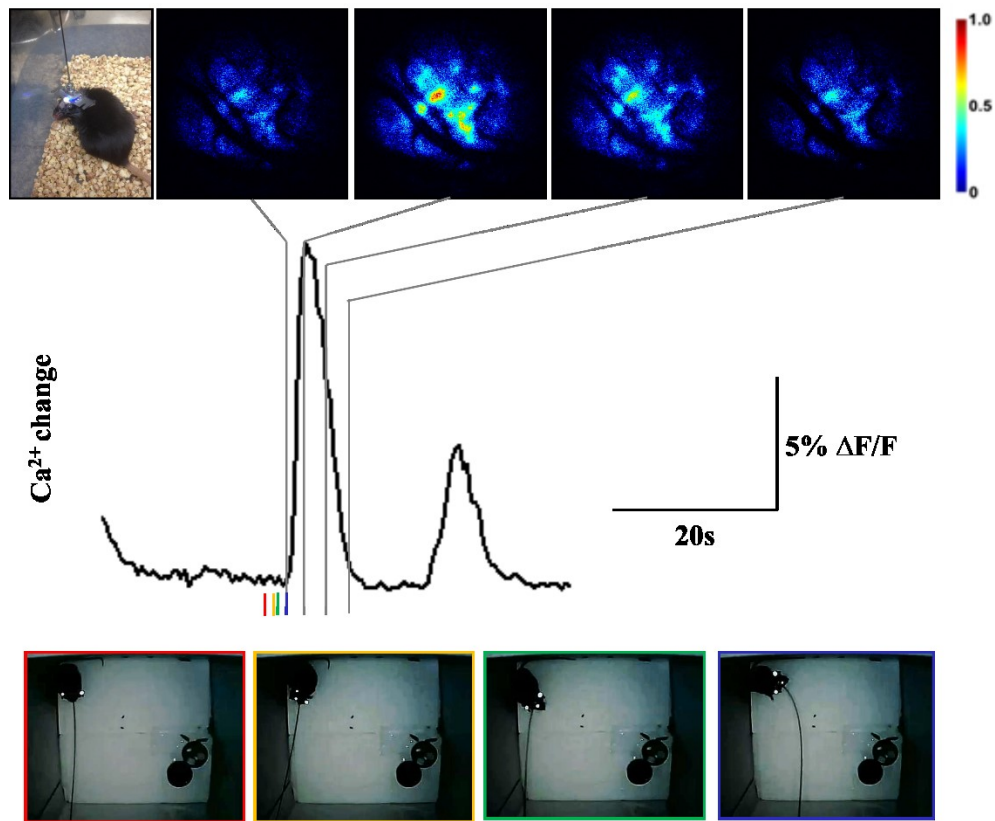
Figure 5.16. Imaging astrocyte Ca^{2+} transients in a freely moving mouse. (Top left) A photograph of the freely moving mouse, for which astrocytic Ca^{2+} responses in the primary visual cortex (V1) were imaged by using an optical fiber. (Top right panel) Pseudo-colored images of temporal changes in the GCaMP3 fluorescence during the head movement. (Middle trace) GCaMP3 fluorescence vs. time, with color bars indicating different times. (Bottom panel) Animal motion recorded by using a NIR camera, for different times in the middle panel.
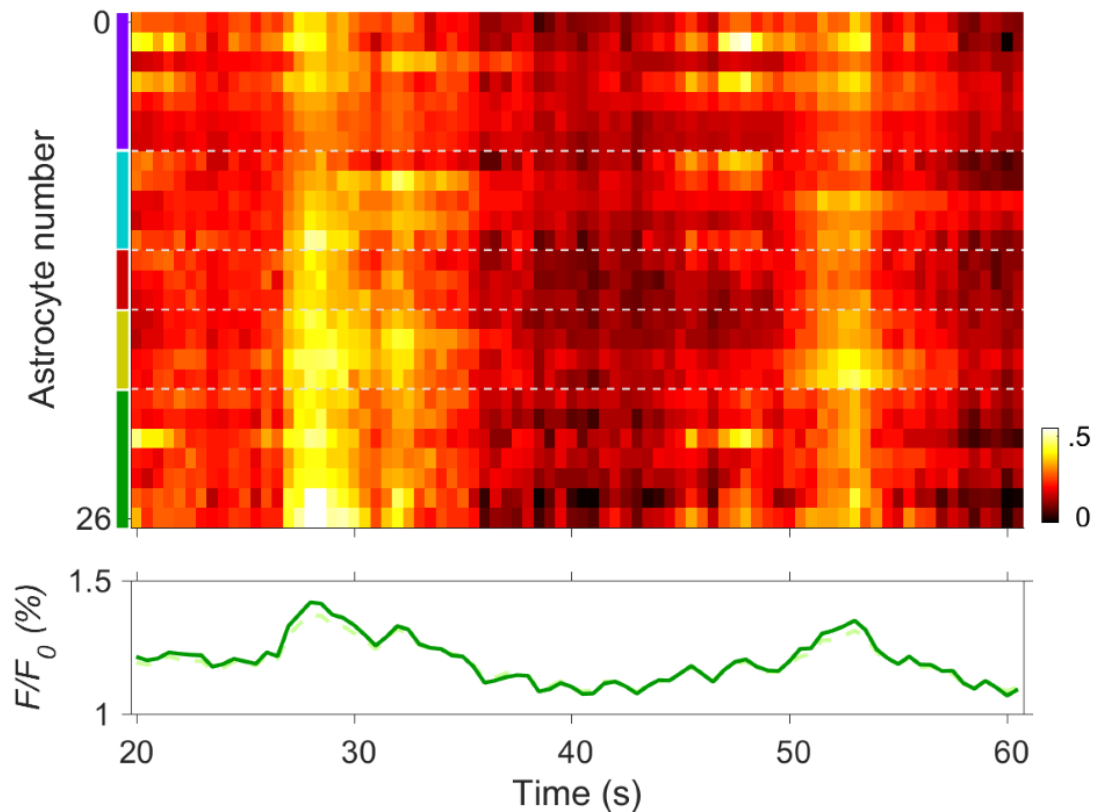
Figure 5.17. Ca^{2+} responses of V1 astrocytes to the head movement. The raster plot shows the temporal progression of the Ca^{2+} signal amplitude for all astrocytes in the field of view, with the colors on the left encoding the different fields of view. The traces in the bottom panel show the average Ca^{2+} signals for the different fields of view.

This system also enables long-term monitoring of brain activity and animal motion, and the results of a 24-h-long imaging experiment are summarized in Fig. 5.18. Astrocytes have recently been hypothesized to modulate slow wave activity that characterizes circadian sleep cycle. Because our recording windows were 1-min-long each, no apparent correlation between the activation of astrocytic network and circadian sleep cycle was observed in the current study. However, frequency analysis can be made possible by reducing the sampling rate to, e.g., 0.2 Hz (e.g., sample every 5 s).
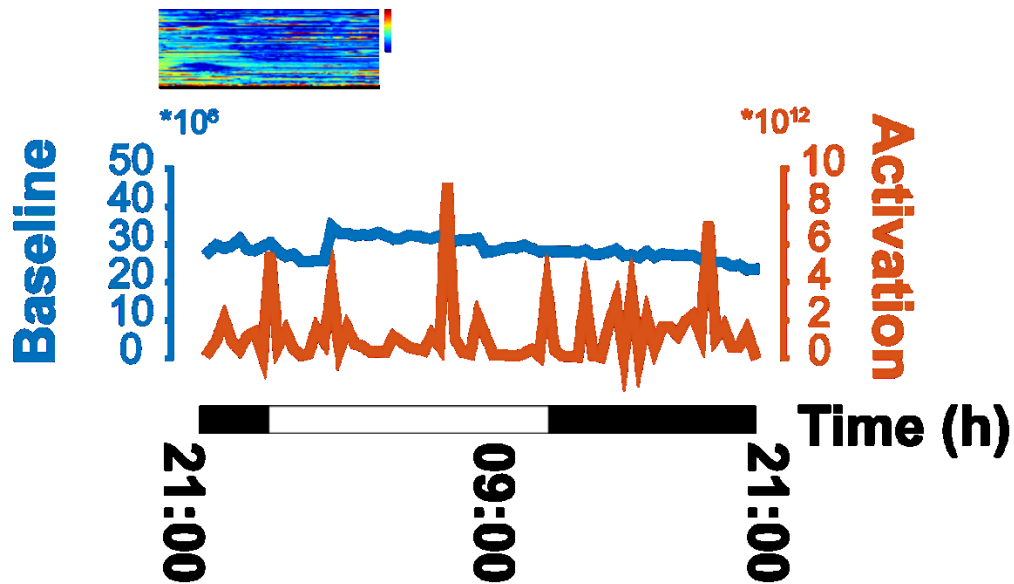
Figure 5.18. Results of a 24-h-long imaging experiment. The blue trace represents the change in the baseline signal. The orange trace represents the average (over astrocytes) change in Ca^{2+}. The black bar on the bottom indicates time.

5.4.3 Discussion

Relating functional cellular activity to animal behavior requires concurrent monitoring of both [93]. This Section presented the capability of combined behavioral and optical signal analyses, highlighting the potential importance of momentary behavioral patterns on brain activity. The system enabled precise synchronization of brain imaging data with behavioral data, thus facilitating the analysis of the relationship between neurochemical activity and behavior. Furthermore, the imaging platform, software, and NIR illumination during night allowed to record behavioral and neurochemical activity over the period of 24 h. This unique characteristic is likely to be useful for a wide range of studies, such as long-term monitoring of disease progression and cellular migration within the brain. Future studies will focus on developing automated conditioning and real-time online data analysis.

CHAPTER 6: MULTISPECTRAL TISSUE CHARACTERIZATION FOR INTESTNINAL ANASTOMOSIS

6.1   Background and Overview

Over a million anastomoses are performed in the US each year for visceral indication alone (gastrointestinal, urologic, and gynecologic surgeries) [94]. To date, intestinal anastomosis surgeries are performed either openly or through minimally invasive techniques using sutures or mechanical staplers [95-98]. Despite the routine nature of intestinal anastomosis procedures, the rate of complications such as anastomotic leakage and strictures is between 3% and 19% and remains unchanged despite the introduction of newer techniques and technologies [99, 100]. These complications undermine the clinical outcomes and often require repeat surgery, leading to a significant increase in treatment cost, morbidity, and mortality [101]. Generally, suturing techniques such as suture placements are guided by the surgeon's visual perception. Although there have been remarkable advances in surgical imaging systems [102, 103] and contrast-enhancing methods [104] for improving surgical vision [105], it is desirable to have optical imaging tools to guide and improve the surgeon's intraoperative decisions and facilitate anastomosis with a clearer target-to-background tissue contrast to improve surgical outcomes.

Multispectral imaging (MSI) is an advanced imaging technique to capture scene information at different spectral wavelengths, which has been used to spatially and spectrally classify similar materials according to their distinguished signatures[106]. Multispectral images show structural properties that may be invisible using a single

wavelength and can also reveal subsurface features at longer wavelengths, such as near-infrared light. Various biomedical applications [107] such as cancer detection[108] and blood oxygen saturation observations in skin [109] have been reported by employing this technique. On the other hand, polarization-sensitive imaging (PSI) uses the scattering and polarization properties of light propagating in the tissue [110]. When incident light strikes the tissue surface, a portion of the light is reflected as specular reflection, while another portion propagates through the tissue. The light propagating through the tissue is depolarized. However, the Fresnel reflection from the surface retains the original polarization state. By considering the fact that the difference in the polarization states depends on the light penetration depth, polarization control techniques are often used for depth-selective measurements [111]. In addition, cross-polarization imaging methods can be used to eliminate specular reflection from the tissue surface, allowing clear identification of subsurface structures, which is often required for surgical procedures [112, 113].

In this chapter, an MSI platform that offers a guide to surgeons for optimum suture placement in bowel anastomosis is presented. This platform provides a novel combination of an MSI system with PSI, for analyzing spatial and spectral data acquired from tissues at all points across the measured imaging area. MSI for displaying subsurface tissue information beyond the human visual spectrum to guide and optimize suture placements has not been applied to date. The system performance is evaluated through *ex vivo* porcine small intestinal tissue imaging, as the morphology and size is similar to human small intestine. Although *ex vivo* tissue does not possess blood flow, tensile strength, or tissue perfusion similar to those of intact live tissue, their anatomical

122

tissue characteristics such as blood vessels, thickness, and tissue types remain unchanged. The data on the spatial and spectral characteristics of the tissues, which were obtained from MSI images, were further processed to identify blood vessels, differentiate between thin and thick tissue areas, and segment different tissue regions. Blood vessel avoidance is clinically important to limit bleeding and retain blood supply to the suture site for healing [114]. Thicker tissue areas have higher mechanical and suture retention strength, and are more suitable for suture placement. Predicting mechanical strength of tissue is highly relevant in robot-assisted surgical procedures with limited haptic feedback as well as in pediatric surgeries where anastomosis is performed in often paper-thin tissue, and long tissue gaps exist between ends requiring large forces to approximate and secure the ends [115]. Tissue thickness also influences the ideal suture bite size, which is typically recommended as 1.5 times tissue thickness. Tissue classification is important to identify the cut line and the area of the tissue within the surgical field that needs to be sutured. The segmentation and identification resulted in a numerical topographic suture map corresponding to desirable suture locations, which could assist surgeons in suturing.

6.2   Materials and Methods

The method consisted of 4 main steps (Fig. 6.1). First, for data acquisition, a portable MSI system (Hardware/Software) acquired raw data (X) and output data (Y) of multiple single-band images for image analysis. Second, 3 submaps were created by blood vessel segmentation, thickness differentiation, and multispectral tissue classification. Specifically, in the blood vessel map, for example, pixels which confidently belong to a blood vessel are assigned a value of 0 and everything else a value of 1. A 2D Gaussian

123

smoothing is used to generate values between 0 and 1 to create a vessel-possibility map around the confidently-segmented blood vessels. Thick tissues that could be sutured well were also assigned a value of 1 and thin tissues were assigned a value of 0, and 2D Gaussian smoothing filtered values assigned to tissue regions between confident-thin (0) and confident-thick (1) areas. Additionally, morphological image processing of the multispectral tissue classification output identifies the bowel cut section, from which a submap for bite depth can be created. Third, given the parameters from the image analysis, a suture map (J) was generated by combining the submaps using an element-wise matrix multiplication operator, where high-intensity pixels correspond to desirable suture locations. Fourth, an optimization technique identified local peaks in the suture map as candidates for desired suture locations. Equidistant suture placements are chosen from the candidates based on the recommended inter-suture distance of 1.5 times the tissue thickness to help surgeons prioritize and identify the areas that are suitable for suture placements.
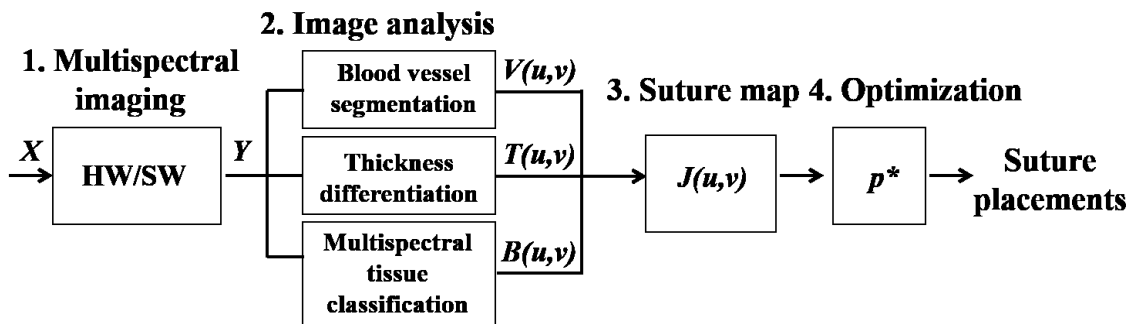
Figure 6.1. System block diagram to create recommendations for optimal suture placements.

6.2.1 *Implementation of the MSI System*

A schematic of the MSI platform is presented in Fig. 6.2. A predetermined narrowband high-power light-emitting diode (LED) light source (SR-02, Quadica Developments Inc., Ontario, Canada) was used with a fiber-optic ring light guide and a condensing lens to generate 3 uniform illumination lights (center wavelengths: 470 nm, 600 nm, and 770 nm) in series. These wavelengths in the visible spectrum were selected to demonstrate hemoglobin absorption and to examine the effects of wavelengths on penetration depth [116]. Since the LED light was unpolarized and the use of non-polarization-maintaining fibers randomized the polarization state of the light [117], we applied a polarizing sheet onto the distal end of the ring light guide to create linearly polarized illumination. Reflected light from the tissue passes back through the empty space of a ring light guide, a rotating linear polarizer filter (46 mm, Prinz Optics GmbH, Stromberg, Germany), a macro lens (Fujinon HF 12.5 SA-1, Phoenix Imaging Ltd., Michigan, USA) and finally reaches a near-infrared camera (acA2000-50gmNIR, Basler, Pennsylvania, USA). By adjusting the angle of the linear polarizer attached to the camera, we can effectively control the amount of polarization effects. To reduce specular reflections from the tissue surfaces, 2 linear polarizers were set orthogonal to each other. Three different spectral images were acquired at 6 fps, with the image size of 1280×1080 pixels. LED-based MSI has an advantage over hyperspectral imaging in that it enables high-speed image acquisition and data processing, which could be potentially useful for real-time guidance. Both LED control and image acquisition were programmed using a custom C# script (Visual Studio 2010, Microsoft, USA). The acquired images were cropped to obtain the tissue region of interest (735×637 pixels) for image processing. The 470 nm band

images were selected for blood vessel segmentation [118]. In addition, all 3 spectral band images were combined to form composite images that were used for the multispectral analysis.
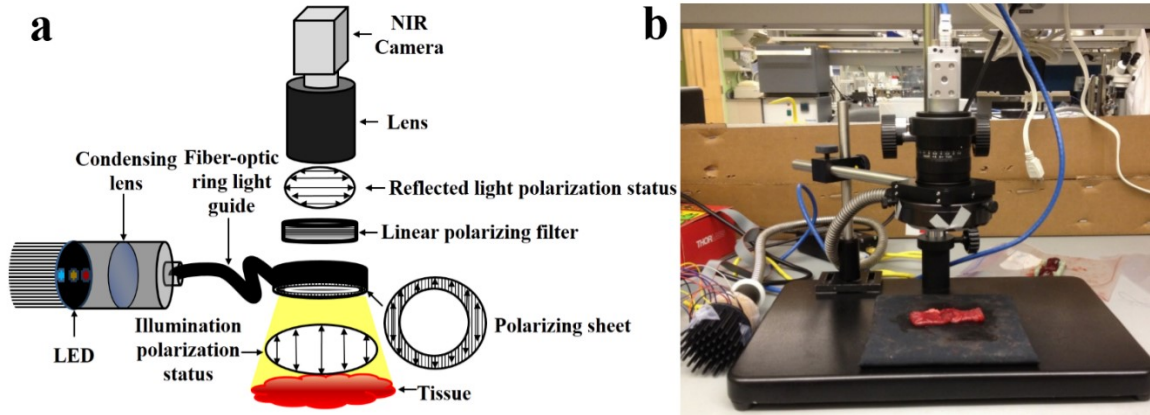
Figure 6.2. (a) Schematic of the MSI system and (b) A photo of system implementation.

6.2.2 Animal Tissue Preparation

Fresh porcine small bowels were obtained from a local abattoir and dissected into segments of 20 cm to 30 cm long. The sample was moistened with physiological saline and preserved at 4°C for up to 30 hours from the time of slaughter until imaging. Before imaging, different segments of the small and large bowels were dissected into 5-cm-long specimens. During the measurements, the remaining samples were preserved in saline in sealed sterile containers for hydration maintenance for up to 30 min.

6.2.3 Image Analysis and Suture Map

In this study, 3 tissue maps of blood vessel segmentation (V), thickness differentiation (T), and bite depth based on multispectral tissue classification (B) were produced.

- Blood vessel segmentation: vasculature structure is identified by applying a 2D filter [119] on the single-band cross-polarized 470 nm channel. The filter identifies and segments vessels by examining the Hessian of the image and measuring the eigenvalues of the Hessian [119]. The resulting blood vessel map is negated to assign the value of 0 to blood vessels. The vessel map was further smoothed with a 2D Gaussian avoid neighboring pixels.

- Tissue thickness differentiation: the images obtained at 470 nm, 600 nm, and 770 nm were evaluated using a supervised spectral angle mapper (SAM) method .[28,29] The SAM technique characterizes the spectral similarity between individual pixels of a sample and *a priori* reference by computing the angle of difference between their spectral vectors. We chose as a reference an averaged spectrum of five arbitrary, non-overlapping tissue regions within a similar tissue thickness. The outcome of SAM was an abundance map that resembled the original image, with spectral signature information of each tissue type. In this application, the endmember references were predefined to be the double-layered (non-incised) and single-layered (incised) tissue areas as the spectral library for SAM method. The SAM extracted features were used to confirm the thicker tissue area within the surgical suture site. A similar smooth kernel, as explained in blood vessel segmentation, is applied to SAM's extracted thicker tissue endmember to indicate local maximums for the final suture map convolution.

- Bite depth from multispectral tissue classification: the acquired multispectral images were analyzed using the image analysis software MultiSpec, a freeware multispectral image data analysis system. By creating a composite image from

multispectral images, 4 different regions (background, inner/outer tissues, and mesentery) were manually defined by designating training fields, and the discriminant analysis was performed to classify the corresponding regions. The inner and outer tissues were then used to extract the boundary of the cut section, where sutures should be placed. The distance of suture placement from the cut section is also referred to as the *bite depth*. Normally, surgeons choose a bite depth of 1.5 times the thickness of the lumen. We create a *bite depth* map which approximates this empirical rule.

The combination of the above 3 mentioned tissue maps resulted in the suture map. The intensity levels of the suture map, *J(u,v)*, ranged from 0 to 1, where 0 denotes a location that should absolutely be avoided for suture and 1 denotes a location that could be used for suture with minimal complications. The fusion operator used to combine these different matrix maps into a single suture map is the element-wise matrix multiplication:

$$J = V \otimes T \otimes B, \quad (1)$$

where V is blood vessel segmentation map, T is the thickness differentiation map, and B is the map obtained from processing of the multispectral tissue classification, and $\otimes$ is the element-wise matrix multiplication operator, i.e., $J(u, v) = V(u, v) \times T(u, v) \times B(u, v)$, where u and v are the horizontal and vertical pixel indices.

The optimal suture points could be calculated automatically by solving the following optimization problem locally:

$$p^* = \arg\max_{p=[u,v]} J(u,v), \quad (2)$$

where *p*= [u*, v*]* is a local maximum of the suture map *J*.

This optimization problem is not convex and does not have a global maximum. Local maxima were extracted as candidates for suture placements. A computationally-efficient method to solve this non-linear optimization problem approximately is to first eliminate all the pixels that are smaller than a threshold. The remaining pixel values are then compared to their 8 neighbors. If a value is larger than all 8 neighbors it is kept as a local maximum. This method will find most of the local maxima in the suture map image quickly. Using an equidistance consistency constraint, the candidate list of placements can be refined to include only equidistant suture placement recommendations. The final list of recommendations along with a colormap visualization of the suture map J are provided to the surgeon to make informed decision on avoiding vessels, choosing thick tissue to retain stronger forces, and be at an accepted distance from the lumen cut section.

6.3 Results

6.3.1 MSI

Fig. 6. 3 shows a porcine intestinal tissue imaging result at 3 different wavelengths, where the superficial features including the blood vessels are accentuated at 470 nm (red arrows). At 770 nm, light penetrates deeper within the tissue, revealing subsurface features (yellow arrows in Fig. 6. 3(c) and (f)). The figure also demonstrates that the cross-polarization scheme can successfully eliminate surface reflections such as glare from the tissue. Note that as the illumination wavelength band increases from blue to red and near-infrared, the image contrast decreases owing to the increased scattering and mean free path at longer wavelengths.
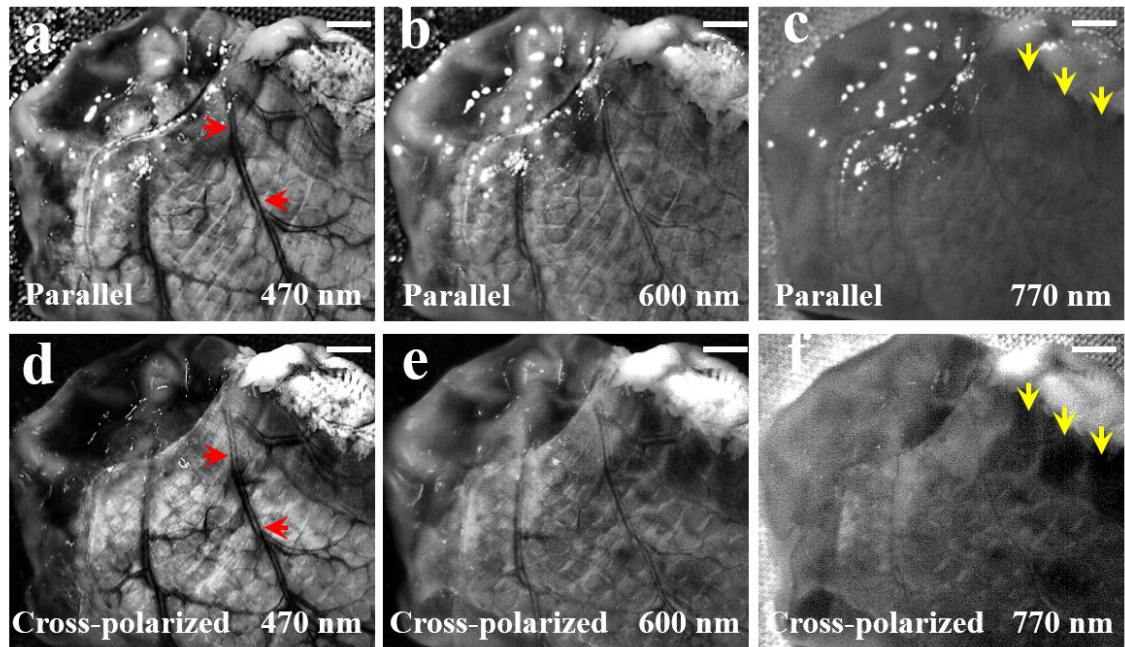
Figure 6.3. Different spectral band images of a tissue sample and surface reflection removal. Arrows indicate features of blood vessels in red color; and the revealed subsurface features in yellow color. White scale bars: 2 mm.

6.3.2   Blood Vessel Map
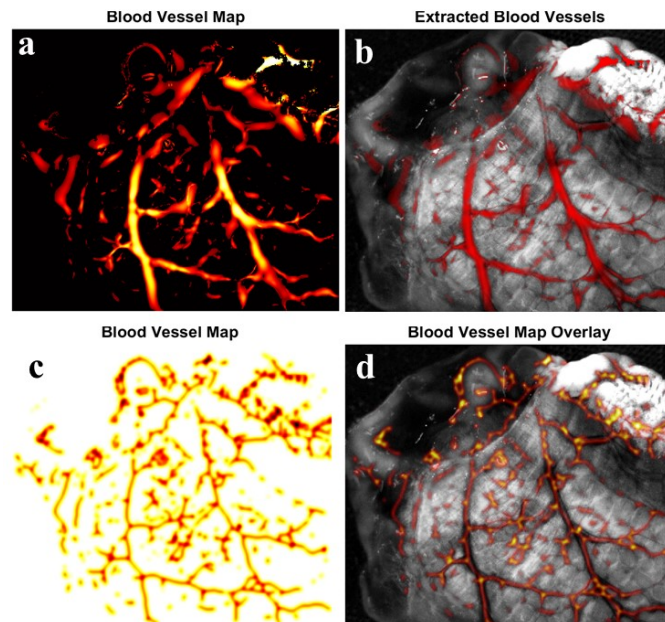
Figure 6.4. (a) Blood vessel segmentation using Frangi 2D filter.[24] (b) Blood vessel segmentation result (red) image overlay on the single-band image at 470 nm. (c) Blood vessel map $V(u, v)$ created by Gaussian filter smoothing of the output of the Frangi 2D filter. (d) Image overlay of inverted vessel map (inverted for better visualization) on the single-band reflectance image of the intestine.

Fig. 6. 4(a) shows the result of the 2D Frangi filter [119] on the single-band cross-polarized 470 nm channel, which identifies the vasculature structure using a colormap. The values range from 0 to 1, where larger values correspond to a more confident identification of a blood vessel. Fig. 6. 4(b) overlays the result in red on the input image for visualization and comparison purposes. The blood vessel map in Fig. 6. 4(c) is extracted from the vasculature structure by negating and Gaussian filter smoothing. The dark areas identify blood vessels that should be avoided to prevent stricture. Blood vessel avoidance is achieved by element-wise multiplication of the blood vessel map to other maps. Fig. 6. 4(d) visualizes the blood vessel map on the input 470-nm band image.

6.3.3   Thickness Map

Thickness differentiation was performed using SAM [120, 121]. A pilot study for thickness measurement, as demonstrated in Fig. 5, involved the use of 3 controlled bovine colon samples with layer heights of 0.75 mm (S1), 7.27 mm (S2), and 9.72 mm (S3). The mesenteries attached to the intestine were considered as separated tissues, which were extracted before the thickness analysis.
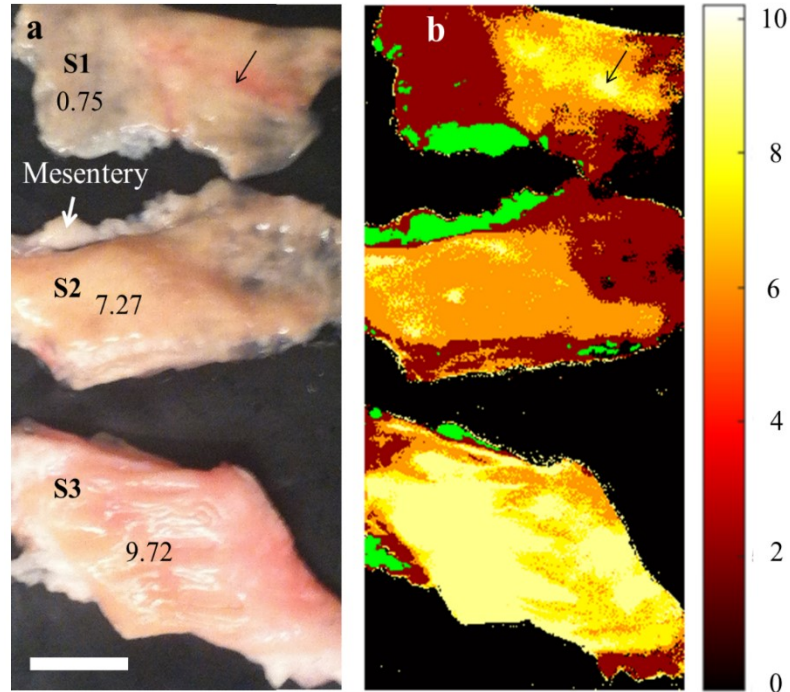
Figure 6.5. (a) Digital photograph of 3 bovine colon tissues with different specified thicknesses (Units in mm). (b) Thickness differentiation using the SAM method, with a thickness-corresponding colormap. The mesentery is indicated as a different tissue in green color. Black arrows: Thicker tissue areas; White scale bar: 10 mm; Colormap unit: mm.

Fig. 6. 5(b) shows the analyzed tissue thickness indicated by a heat colormap to represent thickness ranging from 0 to 10 mm. The result was mostly consistent with the measured physical dimensions of each sample, as shown in Fig. 6. 5(a). In addition it also indicates the effect of tissue types on thickness analysis, especially in the situation of a thin non-homogenous sample such as S1, where blood vessel at similar height as S2 is classified as having the same thickness as the sample S3 (Fig. 6. 5, black arrows).

Similarly, the same SAM method was applied to the multispectral images of the same porcine intestinal tissue in order to extract thick tissue area, as it is highly influenced on applied suture tension and bite size. Bowel wall thickness increases with age from 0.5 mm for infants to 2.0mm for adults based on ultrasounds [122] and is

generally thicker than 0.9 mm in healthy pediatric and adult subjects [123]. Thus, a lower

limit of wall thickness for suturing was considered to be 1mm. The bowel tissue sample

with a scalpel was prepared to contain a thinned out section with thickness below 1mm

on the left (Fig. 6. 6 orange, corresponding to a zero for the suture map calculations) and

a thicker section of about 2mm thickness on the right (Fig. 6. 6, red, corresponding to a 1

for the suture map calculations). Fig. 6. 6 shows the tissue thickness analysis using the

supervised SAM method with predefined endmember references of thicker tissue section

on the single-layered intestinal region (in red color) and thinner tissue section at the

double-layered intestinal section (in orange color). The single-layered region indicates

the incised section while the double-layered one indicates non-incised region. Prior to the

SAM analysis, the image is analyzed to segment features such as the mesentery (in green)

or blood vessels (in yellow).
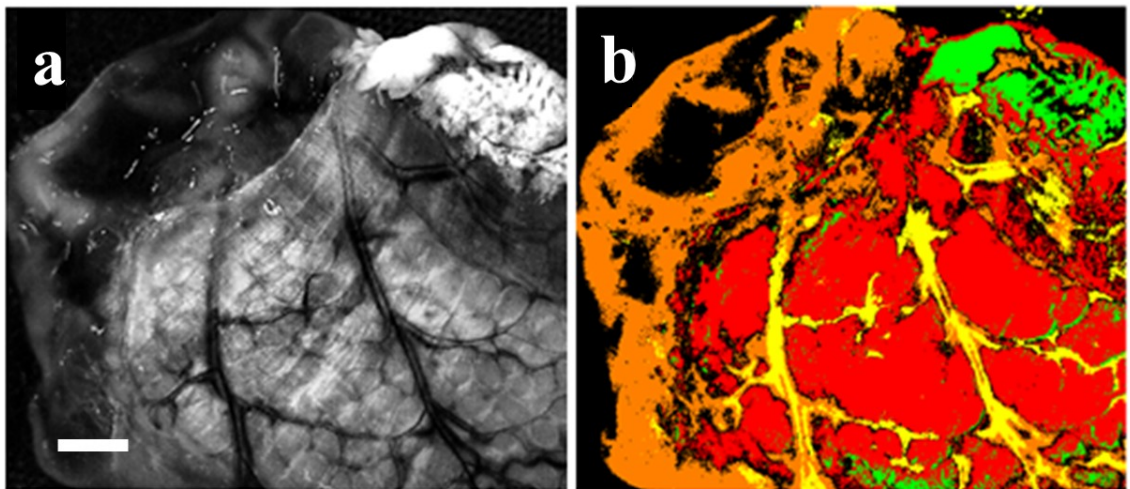
Figure 6.6. (a) Representative single band reflectance image at 470 nm. (b) Thickness differentiation using the SAM method, with a thickness-corresponding colormap. Red color shows the thicker layer and orange color shows the thinner layer. Tissue classification of the mesentery (green) and blood vessels (yellow) were performed prior to the thickness analysis. White scale bar: 2 mm.

A smooth Gaussian kernel convolution was further implemented on this non-incised region. The smoothing kernel is used on the thickness binary map to signify the necessary thick tissue density for the convolution of *B(u,v)* and *V(u,v)* maps (Fig. 6.7).
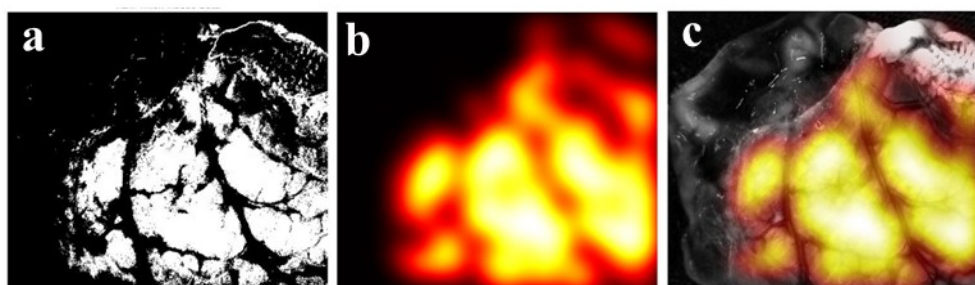
Figure 6.7. (a) Thickness binary map as evaluated by the SAM algorithm. (b) Smoothed thickness map *T(u,v)*. Larger values (brighter) denote areas with thicker tissue which are better suited for suture placement. (c) Overlay of thickness map over a single-band image for better visualization.

6.3.4   Multispectral Tissue Classification and Bite Depth Map
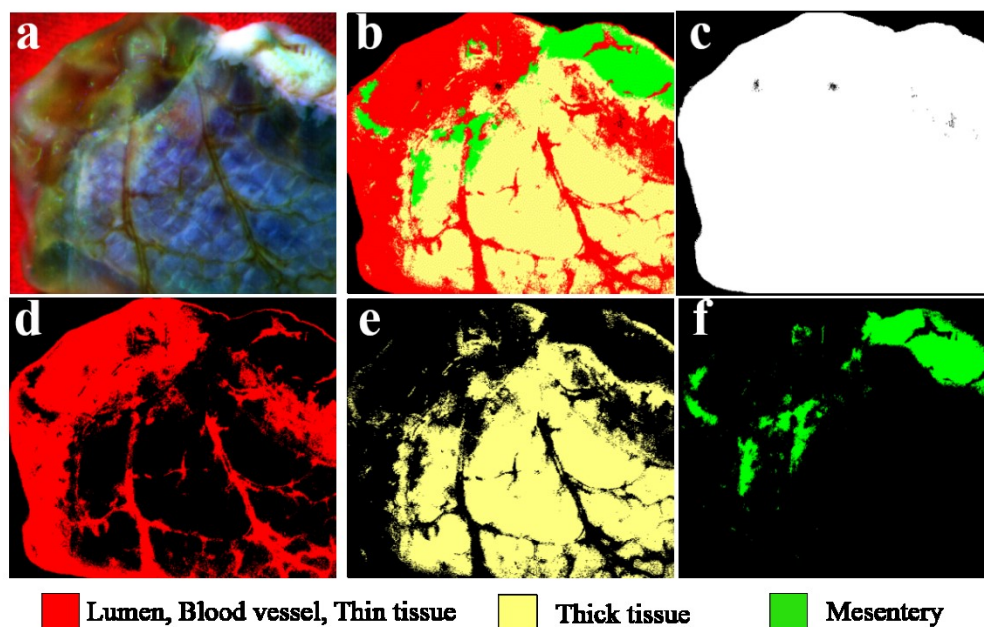
Figure 6.8. Multispectral tissue classification. (a) Composite image created from 3 spectral band images. (b) Classified image using the supervised classification algorithm. (c) Background color-matching image (black). (d) Image showing the vulnerable tissue (lumen, blood vessels and thin tissue regions) (red). (e) Image showing the thick tissue regions (yellow). (f) Image showing the mesentery (green).

The multispectral tissue analysis results using multispec program are shown in Fig. 6. 8. The composite image (Fig. 6. 8(a)) of the porcine intestinal tissue was created from 3 spectral band images of the background, lumen (mucosa, submucosa layer), blood vessels, thick/tissue outer layer of serosa and the mesentery. Those 4 regions were segmented in different colors (Fig. 6. 8 (b)). The foreground mask is shown in Fig. 6. 8(c). The lumen, blood vessel, and thin tissue areas of serosa and mesentery are shown as red (Fig. 6. 8(d)) and yellow (Fig. 6. 8(e)), respectively, whereas the mesentery is depicted in green (Fig. 6. 8(f)). Although a small tissue portion including the blood vessels was indicated in red, the program successfully segmented the inside and outside tissue areas and the mesentery. The blood vessels will be accurately accounted for in the final map, using the specific blood vessel segmentation results (Section 6.3.2). One can observe that lumen, blood vessel, thin/thick tissue regions of the intestine and mesentery are successfully segmented by the algorithm after repetition of training sets for several tissue types as supervised by the user. The inside and outside of the lumen can be used to extract the edge between the two regions, which outlines the cut line (Fig. 6. 9(a)-6. 9(c)). The cut line is used as a reference to place sutures at a certain distance for better healing. To extract the edge regions, we used standard binary image processing methods of dilation and erosion in MATLAB (R2015a, Mathworks Inc., Massachusetts, USA). This line (Fig. 6. 9(c)) was used to determine the bite-size distance, given the tissue type and size. In surgery, the rule of thumb for the general suture technique is to calculate the suture placement distance from the tissue cut end (suture width) as 1.5 times the tissue thickness, $\tau 23$. The computed bite-size distance was convolved with a smooth Gaussian to account for uncertainty in the bite-size distance computation. The standard deviation σ of the Gaussian filter is chosen to give more weight

to points that are at 1.5τ [mm] distance, but are not closer than δ mm from the cut edge.

For the 99.7% of the filtered values to be in this range (3σ-rule), $\sigma = (1.5\tau - \delta)/3$. The value

of δ depends on the suture size, but usually should not be smaller than 0.5mm. With a tissue

thickness of 1mm, σ=0.33mm. The resulting map, B(u,v), is depicted in Fig. 6. 9(d)-6. 9(e).
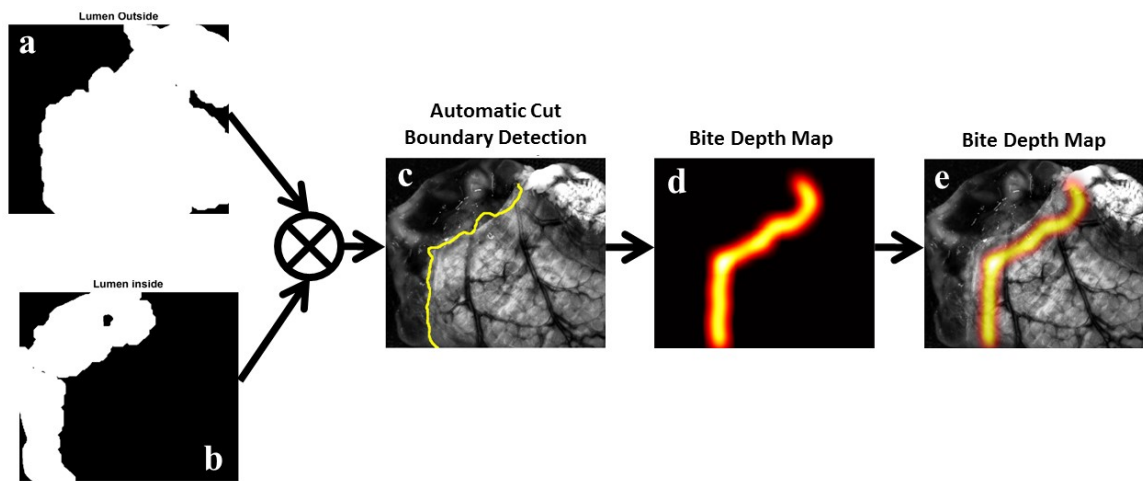
Figure 6.9. Multispectral image analysis facilitates segmentation of (a) outer layer of the lumen (Serosa) and (b) inner layers of the lumen (Mucosa and submucosa layers). (c) The cut edge is automatically extracted by pixel-wise multiplication of a dilated map of outer and inner layers of the lumen. (d) A bite depth map B(u,v) is generated by translating and smoothing the cut edge by 1.5 times the thickness of the tissue. (e) Overlay of the bite depth map on a single-band image for better visualization.

6.3.5 Suture Map and Suture Placement Recommendations
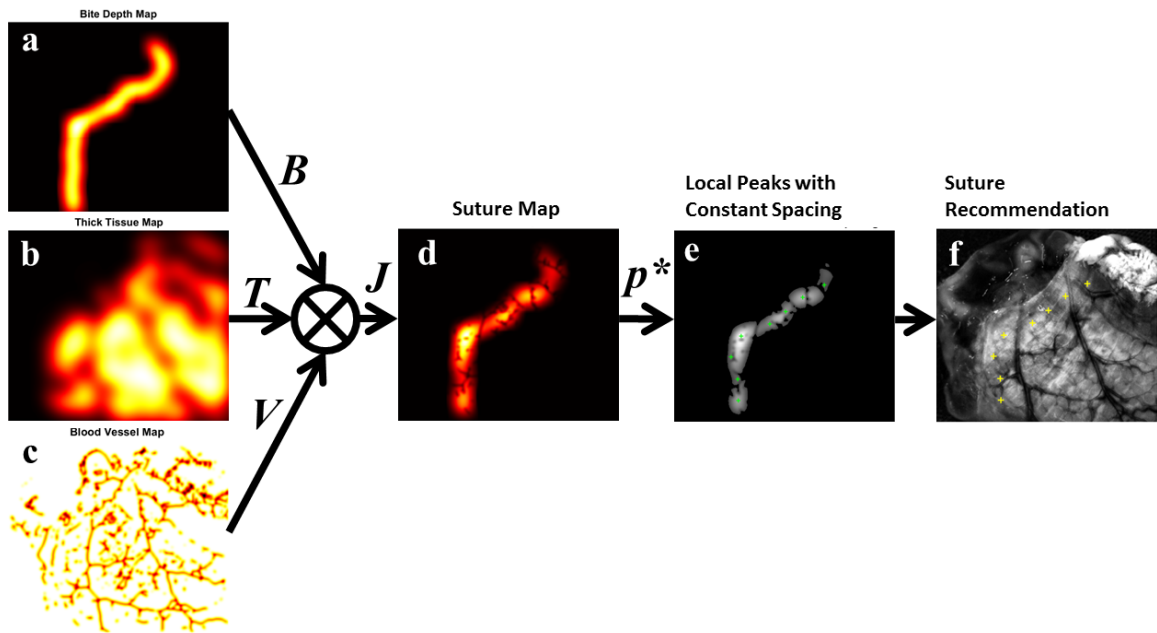
Figure 6.10. Suture map and suture placement recommendations. (a) Bite-depth map $B(u,v)$. (b) Thick tissue map $T(u,v)$. (c) Blood vessel map $V(u,v)$. (d) Combined map $J(u,v)$. (e) Selection of local peaks with equal-space consistency constraint. (f) An overlay image of the recommended suture locations.
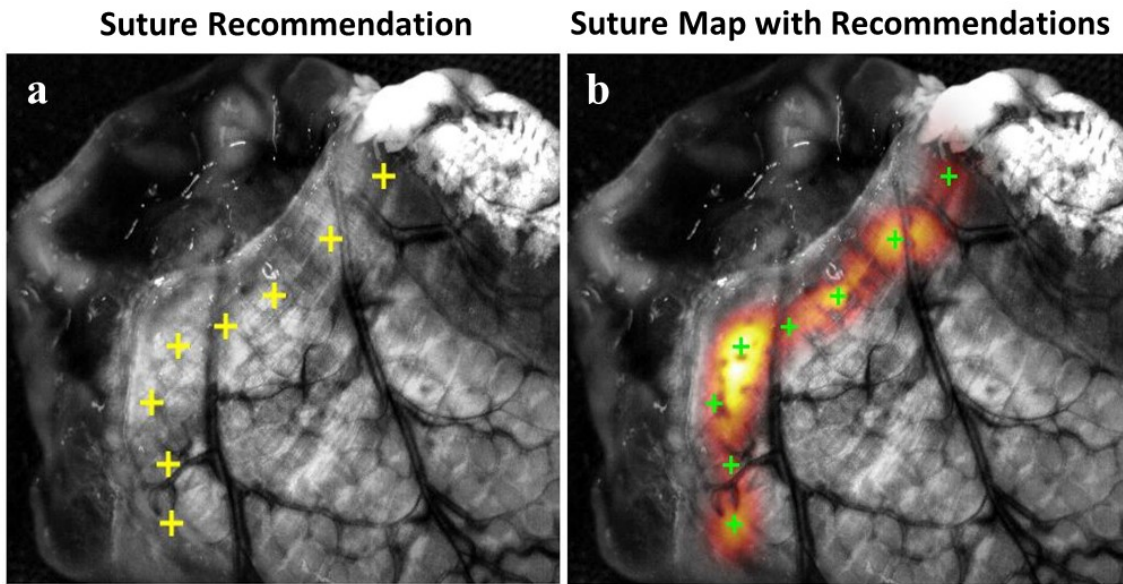
Figure 6.11. (a) A magnified view of the suture placement recommendations and (b) A colormap overlay of the suture map provided to the surgeon to overrule recommendations and choose other acceptable regions.

Finally, a suture map including the anatomical and geometrical information was generated using the smooth gradients from the individual image analyses (Fig. 6. 10). The bite-depth, tissue thickness, and blood vessel maps (Fig. 6. 10(a)-6. 10(c)) are combined using a multiplier operator to create the suture map, as shown in Fig. 6. 10(d). Suture placement recommendations are the local maxima from the suture map and are depicted in Fig. 6. 10(e) with the overlay image shown in Fig. 6. 10(f)). At the end, the surgeon is provided both the recommendations as well as a colormap overlay of the acceptable suture locations on the image so that they can decide if they want to overrule the recommendation of the software.

6.4   Discussion

Providing surgeons with subsurface tissue information beyond standard surface shapes and patterns obtained using current surgical imaging techniques may improve the surgeon's decision making and lead to better surgeries and reduced complication rates. Towards this goal, an MSI platform was developed and evaluated for intestinal anastomosis. The system successfully determined blood vessel locations, tissue thickness, correctly classified the tissue regions, and combined the information to recommend optimal suture locations. Limitations of this study include the small sample size and the use of flattened two-dimensional *ex vivo* tissue [124]. Future research should focus on acquiring more *ex vivo* tissue data to allow separation of training and test data sets and to compare to ground truth. Another important step is to translate these findings to *in vivo* studies on tissues. Other tissue characteristics such as tissue perfusion, which is important for healing and can be detected using MSI, should also be included in the analysis and

suture location optimization. Such suture maps processed in real-time may potentially provide access to the best tissue information for anastomosis and thus mitigate the highly variable experiences and intraoperative decisions of surgeons. These suture maps showing the optimal suturing regions could also provide guidance to automated surgical procedures, where robots assist surgeons [125] in performing safer operations with higher precision in less time. In summary, this study demonstrates the feasibility of an MSI platform for the identification of blood vessels, differentiation between thin and thick tissue areas, and segmentation of different tissue types. The information is useful in determination of the optimal suture placements, which contributes to the development of a safer operation with reduced complications.

CHAPTER 7: CONCLUSIONS

In this Chapter, the technical achievements and contribution of this dissertation are summarized along with some discussion of future research directions.

7.1 Summary of Contributions

In this dissertation, a fiber-optic bundle-based microscope imager was implemented for studying the astrocyte network activities in the brain of freely moving mice. Several imaging systems were constructed to achieve high-resolution cellular imaging up to 3 μm. Novel image-processing algorithms were applied to improve the quality of fiber-bundle imaging (SNR of 4.4 dB, PSNR of 18.03 dB with two-fold resolution improvement both in axial and lateral resolutions). The developed imaging platform was utilized for correlating the astrocytic network activity with distinct patterns of animal behavior.

To visualize cellular imaging and astrocytic Ca^{2+} activity *in vivo*, several fiber-bundle imagers were constructed and evaluated. A dual-mode fiber bundle imager was developed for simultaneous confocal reflectance and fluorescence imaging. Automatic calculation of gene transfection efficacy was assessed using human cervical cancer cells. A single ball-lens integrated fiber-bundle imaging probe was designed to offer a better lateral resolution of ~2 μm and longer working distance of 1.5 mm. Two types of imaging probes, one with 350 μm field-of-view, 324 μm working distance and another with 500 μm field-of-view, 1.5 mm working distance, were fabricated to demonstrate their applicability to deep and surface brain imaging *in vivo* respectively. A spatially multiplexed fiber-bundle imager allowing simultaneous imaging of multiple brain regions was proposed and experimentally demonstrated.

To improve the fiber-bundle image quality, structured illumination microscopy was used with depth-resolved imaging (12 μm axial resolution) and super-resolution imaging (2.46 μm lateral resolution). A DMD was used to generate and optimize the structured illumination pattern promptly (~60 Hz); thus, optically sectioned images were obtained from live mice brain in the first-in-first-out processing. Super-resolution fiber-bundle imaging was numerically and experimentally demonstrated to surpass the diffraction limit on the resolution of 2.9 μm by achieving 2.46 μm, based on linear structured illumination.

To validate the developed imaging systems, each system was used for *in vivo* mouse brain imaging. Dual-fiber probe-based simultaneous astrocytic Ca^{2+} imaging was performed to demonstrate that locomotion triggers simultaneous activation of astrocytic networks in multiple brain regions of the primary visual cortex and cerebellum. Real-time dual-color functional brain imaging was conducted to demonstrate that astrocytic Ca^{2+} activity is coupled to vascular hemodynamics in the cerebral cortex. Finally, the platform for brain imaging of freely behaving mice revealed that astrocytic networks are activated during behaviorally relevant tasks such as resting to active state changes.

In addition, for guiding optimal suture placements in tissue anastomosis, a portable multispectral imaging system was developed and studied for the proof-of-concept validation of intestinal anastomosis in the *ex vivo* porcine model experiment.

7.2   Future Work

In the future work, expanding the current study to the investigation of casual relationships between discrete brain regions of visual cortex, motor cortex, and cerebellum, to the

studies of neuro-glia interactions, and to the studies of social behavior in freely behaving mice by using multi-furcated fibers. In addition, multispectral imaging-guided surgical robot activation and *in vivo* animal studies are envisioned as well.

BIBLIOGRAPHY

1.   Chung, K. and K. Deisseroth, *CLARITY for mapping the nervous system.* Nat Methods, 2013. **10**(6): p. 508-13.

2.   Chung, K., et al., *Structural and molecular interrogation of intact biological systems.* Nature, 2013. **497**(7449): p. 332-7.

3.   Harvey, C.D., et al., *Intracellular dynamics of hippocampal place cells during virtual navigation.* Nature, 2009. **461**(7266): p. 941-6.

4.   Szuts, T.A., et al., *A wireless multi-channel neural amplifier for freely moving animals.* Nat Neurosci, 2011. **14**(2): p. 263-9.

5.   Grinvald, A. and R. Hildesheim, *VSDI: a new era in functional imaging of cortical dynamics.* Nat Rev Neurosci, 2004. **5**(11): p. 874-85.

6.   Tian, L., et al., *Imaging neural activity in worms, flies and mice with improved GCaMP calcium indicators.* Nat Methods, 2009. **6**(12): p. 875-81.

7.   Chen, T.W., et al., *Ultrasensitive fluorescent proteins for imaging neuronal activity.* Nature, 2013. **499**(7458): p. 295-300.

8.   Dombeck, D.A., et al., *Functional imaging of hippocampal place cells at cellular resolution during virtual navigation.* Nat Neurosci, 2010. **13**(11): p. 1433-40.

9.   Nimmerjahn, A., E.A. Mukamel, and M.J. Schnitzer, *Motor behavior activates Bergmann glial networks.* Neuron, 2009. **62**(3): p. 400-12.

10.   Flusberg, B.A., et al., *High-speed, miniaturized fluorescence microscopy in freely moving mice.* Nat Methods, 2008. **5**(11): p. 935-8.

11. Kerr, J.N. and A. Nimmerjahn, *Functional imaging in freely moving animals.* Curr Opin Neurobiol, 2012. **22**(1): p. 45-53.

12. Oh, G., E. Chung, and S.H. Yun, *Optical fibers for high-resolution in vivo microendoscopic fluorescence imaging.* Optical Fiber Technology, 2013. **19**(6, Part B): p. 760-771.

13. Tanbakuchi, A.A., et al., *Clinical confocal microlaparoscope for real-time in vivo optical biopsies.* J Biomed Opt, 2009. **14**(4): p. 044030.

14. Piyawattanametha, W., et al., *In vivo near-infrared dual-axis confocal microendoscopy in the human lower gastrointestinal tract.* J Biomed Opt, 2012. **17**(2): p. 021102.

15. Szabo, V., et al., *Spatially selective holographic photoactivation and functional fluorescence imaging in freely behaving mice with a fiberscope.* Neuron, 2014. **84**(6): p. 1157-69.

16. Han, J.H., J. Lee, and J.U. Kang, *Pixelation effect removal from fiber bundle probe based optical coherence tomography imaging.* Opt Express, 2010. **18**(7): p. 7427-39.

17. Reichenbach, K.L. and C. Xu, *Numerical analysis of light propagation in image fibers or coherent fiber bundles.* Opt Express, 2007. **15**(5): p. 2151-65.

18. Chen, X., K.L. Reichenbach, and C. Xu, *Experimental and theoretical analysis of core-to-core coupling on fiber bundle imaging.* Opt Express, 2008. **16**(26): p. 21598-607.

19. Paukert, M., et al., *Norepinephrine controls astroglial responsiveness to local circuit activity.* Neuron, 2014. **82**(6): p. 1263-70.

20. Lecoq, J., et al., *Visualizing mammalian brain area interactions by dual-axis two-photon calcium imaging.* Nat Neurosci, 2014. **17**(12): p. 1825-9.

21. Guo, Q., et al., *Multi-channel fiber photometry for population neuronal activity recording.* Biomed Opt Express, 2015. **6**(10): p. 3919-31.

22. Saleh, B.E.A., *Fundamentals of Photonics, 2nd Edition.* 2007: Wiley. 1200.

23. Wilson, T., C.J.R. Shepparu, and K. Löschke, *Theory and practice of scanning optical microscopy. Academic Press, London 1984, 213 Seiten, 138 Abbildungen, Preis $ 39.50 ISBN 0-12-757760-2.* Crystal Research and Technology, 1985. **20**(12): p. 1608-1608.

24. Lukosz, W., *Optical Systems with Resolving Powers Exceeding the Classical Limit. II.* Journal of the Optical Society of America, 1967. **57**(7): p. 932-941.

25. Mehta, A.D., et al., *Fiber optic in vivo imaging in the mammalian nervous system.* Curr Opin Neurobiol, 2004. **14**(5): p. 617-28.

26. Flusberg, B.A., et al., *Fiber-optic fluorescence imaging.* Nat Methods, 2005. **2**(12): p. 941-50.

27. Helmchen, F., *Miniaturization of fluorescence microscopes using fibre optics.* Exp Physiol, 2002. **87**(6): p. 737-45.

28. Pawley, J., ed. *Handbook of Biological Confocal Microscopy.* 3 ed. 2006, Springer US. XXVIII, 985.

29. Helmchen, F., et al., *A miniature head-mounted two-photon microscope. high-resolution brain imaging in freely moving animals.* Neuron, 2001. **31**(6): p. 903-12.

30. Gu, M., C.J.R. Sheppard, and X. Gan, *Image formation in a fiber-optical confocal scanning microscope.* Journal of the Optical Society of America A, 1991. **8**(11): p. 1755-1761.

31. Xi, P., ed. *Optical Nanoscopy and Novel Microscopy Techniques*. 1 edition ed. 2014, CRC Press.

32. Sung, K.B., et al., *Near real time in vivo fibre optic confocal microscopy: sub-cellular structure resolved.* J Microsc, 2002. **207**(Pt 2): p. 137-45.

33. Wang, T.D. and J. Van Dam, *Optical biopsy: a new frontier in endoscopic detection and diagnosis.* Clin Gastroenterol Hepatol, 2004. **2**(9): p. 744-53.

34. Liang, C., et al., *Fiber confocal reflectance microscope (FCRM) for in-vivo imaging.* Opt Express, 2001. **9**(13): p. 821-30.

35. Sung, K.B., et al., *Fiber optic confocal reflectance microscopy: a new real-time technique to view nuclear morphology in cervical squamous epithelium in vivo.* Opt Express, 2003. **11**(24): p. 3171-81.

36. Lane, P.M., et al., *Confocal fluorescence microendoscopy of bronchial epithelium.* J Biomed Opt, 2009. **14**(2): p. 024008.

37. Bertani, H., et al., *Advances in Endoscopic Visualization of Barrett's Esophagus: The Role of Confocal Laser Endomicroscopy.* Gastroenterol Res Pract, 2012. **2012**: p. 493961.

38. Shieh, F.K., et al., *High-definition confocal endomicroscopy of the common bile duct.* J Clin Gastroenterol, 2012. **46**(5): p. 401-6.

39. Coron, E., et al., *Colonic mucosal biopsies obtained during confocal endomicroscopy are pre-stained with fluorescein in vivo and are suitable for histologic evaluation.* Endoscopy, 2012. **44**(2): p. 148-53.

40. Ilyin, S.E., M.C. Flynn, and C.R. Plata-Salaman, *Fiber-optic monitoring coupled with confocal microscopy for imaging gene expression in vitro and in vivo.* J Neurosci Methods, 2001. **108**(1): p. 91-6.

41. Doronina-Amitonova, L.V., et al., *Multicolor in vivo brain imaging with a microscope-coupled fiber-bundle microprobe.* Applied Physics Letters, 2012. **101**(23): p. 233702.

42. Kang, J.U., ed. *Fiber Optic Sensing and Imaging*. 1 ed. 2013, Springer-Verlag New York. VII, 171.

43. Miyamoto, D. and M. Murayama, *The fiber-optic imaging and manipulation of neural activity during animal behavior.* Neurosci Res, 2015.

44. Gobel, W., et al., *Miniaturized two-photon microscope based on a flexible coherent fiber bundle and a gradient-index lens objective.* Opt Lett, 2004. **29**(21): p. 2521-3.

45. Jung, J.C., et al., *In vivo mammalian brain imaging using one- and two-photon fluorescence microendoscopy.* J Neurophysiol, 2004. **92**(5): p. 3121-33.

46. Kim, J.K., et al., *Fabrication and operation of GRIN probes for in vivo fluorescence cellular imaging of internal organs in small animals.* Nat Protoc, 2012. **7**(8): p. 1456-69.

47. Barretto, R.P. and M.J. Schnitzer, *In vivo optical microendoscopy for imaging cells lying deep within live tissue.* Cold Spring Harb Protoc, 2012. **2012**(10): p. 1029-34.

48. Kim, J.K., J.W. Choi, and S.H. Yun, *350-mum side-view optical probe for imaging the murine brain in vivo from the cortex to the hypothalamus.* J Biomed Opt, 2013. **18**(5): p. 50502.

49. Cha, J. and J.U. Kang. *Spatially Multiplexed Fiber-optic Microscopy for Simultaneous Imaging of Multiple Brain Regions*. in *CLEO: 2014*. 2014. San Jose, California: Optical Society of America.

50. Cha, J., et al. *Spatially Multiplexed Fiber-optic SLM Microscopy for Applications of Optogenetics*. in *Imaging and Applied Optics 2015*. 2015. Arlington, Virginia: Optical Society of America.

51. J. M. Senior S. E. Moss S. D, C., *Multiplexing Techniques for Noninterferometric Optical Point-Sensor Networks: A Review.* Fiber and Integrated Optics, 1998. **17**(1): p. 3-20.

52. Juskaitis, R. and S.V. Shatalin. *Multiplexing of fiber optic sensors using scanning microscopy*. 1994.

53. Dubaj, V., et al., *Optic fibre bundle contact imaging probe employing a laser scanning confocal microscope.* J Microsc, 2002. **207**(Pt 2): p. 108-17.

54. Lane, P.M., *Terminal reflections in fiber-optic image guides.* Appl Opt, 2009. **48**(30): p. 5802-10.

55. Dzik, W.H. and P. Szuflad, *Method for counting white cells (WBCs) in WBC-reduced red cell concentrates.* Transfusion, 1993. **33**(3): p. 272-3.

56. Huang, Y., et al., *Motion compensated fiber-optic confocal microscope based on a common-path optical coherence tomography distance sensor.* Optical Engineering, 2011. **50**(8): p. 083201-083201-7.

57. Hughes, E.G., et al., *Oligodendrocyte progenitors balance growth with self-repulsion to achieve homeostasis in the adult brain.* Nat Neurosci, 2013. **16**(6): p. 668-76.

58. Broder, J., et al., *Estimating weak ratiometric signals in imaging data. I. Dual-channel data.* J Opt Soc Am A Opt Image Sci Vis, 2007. **24**(9): p. 2921-31.

59. Akerboom, J., et al., *Genetically encoded calcium indicators for multi-color neural activity imaging and combination with optogenetics.* Front Mol Neurosci, 2013. **6**: p. 2.

60. Kim, C.K., et al., *Simultaneous fast measurement of circuit dynamics at multiple sites across the mammalian brain.* Nat Methods, 2016.

61. Goodman, J.W., *Introduction to Fourier Optics, Third Edition*. 2005: Roberts & Company.

62. Verlag, S., M.G. Abdallah, and H.E. Gascoigne, *High Sensitivity Moiré: Experimental Analysis for Mechanics and Materials by Daniel Post, Bongtae Han and Peter Ifju.* Experimental Techniques, 1994. **18**(2): p. 45-46.

63. Gustafsson, M.G., *Surpassing the lateral resolution limit by a factor of two using structured illumination microscopy.* J Microsc, 2000. **198**(Pt 2): p. 82-7.

64. Gustafsson, M.G.L., D.A. Agard, and J.W. Sedat. *Doubling the lateral resolution of wide-field fluorescence microscopy using structured illumination*. 2000.

65. Shroff, S.A., J.R. Fienup, and D.R. Williams. *OTF compensation in structured illumination superresolution images*. 2008.

66. Shroff, S.A., J.R. Fienup, and D.R. Williams, *Phase-shift estimation in sinusoidally illuminated images for lateral superresolution.* J Opt Soc Am A Opt Image Sci Vis, 2009. **26**(2): p. 413-24.

67. Liao, Z., *A computer algorithm to implement linear structured illumination imaging*. 2010.

68. Xu, D., et al., *Fast optical sectioning obtained by structured illumination microscopy using a digital mirror device.* J Biomed Opt, 2013. **18**(6): p. 060503.

69. Wilson, T., *Optical sectioning in fluorescence microscopy.* J Microsc, 2011. **242**(2): p. 111-6.

70. Bozinovic, N., et al., *Fluorescence endomicroscopy with structured illumination.* Opt Express, 2008. **16**(11): p. 8016-25.

71. Winter, C., et al., *Automatic adaptive enhancement for images obtained with fiberscopic endoscopes.* IEEE Trans Biomed Eng, 2006. **53**(10): p. 2035-46.

72. Djukic, B., et al., *Conditional knock-out of Kir4.1 leads to glial membrane depolarization, inhibition of potassium and glutamate uptake, and enhanced short-term synaptic potentiation.* J Neurosci, 2007. **27**(42): p. 11354-65.

73. Mulligan, S.J. and B.A. MacVicar, *Calcium transients in astrocyte endfeet cause cerebrovascular constrictions.* Nature, 2004. **431**(7005): p. 195-9.

74. Min, R. and T. Nevian, *Astrocyte signaling controls spike timing-dependent depression at neocortical synapses.* Nat Neurosci, 2012. **15**(5): p. 746-53.

75.   Attwell, D., et al., *Glial and neuronal control of brain blood flow.* Nature, 2010.
       468(7321): p. 232-43.

76.   Di Castro, M.A., et al., *Local Ca2+ detection and modulation of synaptic release
       by astrocytes.* Nat Neurosci, 2011. **14**(10): p. 1276-84.

77.   Jourdain, P., et al., *Glutamate exocytosis from astrocytes controls synaptic
       strength.* Nat Neurosci, 2007. **10**(3): p. 331-9.

78.   Petravicz, J., T.A. Fiacco, and K.D. McCarthy, *Loss of IP3 receptor-dependent
       Ca2+ increases in hippocampal astrocytes does not affect baseline CA1
       pyramidal neuron synaptic activity.* J Neurosci, 2008. **28**(19): p. 4967-73.

79.   Schummers, J., H. Yu, and M. Sur, *Tuned responses of astrocytes and their
       influence on hemodynamic signals in the visual cortex.* Science, 2008. **320**(5883):
       p. 1638-43.

80.   Takata, N., et al., *Astrocyte calcium signaling transforms cholinergic modulation
       to cortical plasticity in vivo.* J Neurosci, 2011. **31**(49): p. 18155-65.

81.   Chen, N., et al., *Nucleus basalis-enabled stimulus-specific plasticity in the visual
       cortex is mediated by astrocytes.* Proc Natl Acad Sci U S A, 2012. **109**(41): p.
       E2832-41.

82.   Bekar, L.K., W. He, and M. Nedergaard, *Locus coeruleus alpha-adrenergic-
       mediated activation of cortical astrocytes in vivo.* Cereb Cortex, 2008. **18**(12): p.
       2789-95.

83.   Ding, F., et al., *alpha1-Adrenergic receptors mediate coordinated Ca2+ signaling
       of cortical astrocytes in awake, behaving mice.* Cell Calcium, 2013. **54**(6): p. 387-
       94.

84.   Polack, P.O., J. Friedman, and P. Golshani, *Cellular mechanisms of brain state-dependent gain modulation in visual cortex.* Nat Neurosci, 2013. **16**(9): p. 1331-9.

85.   Sharma, U., et al., *Fiber optic confocal laser Doppler velocimeter using an all-fiber laser source for high resolution measurements.* Opt Express, 2005. **13**(16): p. 6250-8.

86.   Zhang, X., S.E. Wong, and F.C. Lightstone, *Message passing interface and multithreading hybrid for parallel molecular docking of large databases on petascale high performance computing machines.* J Comput Chem, 2013. **34**(11): p. 915-27.

87.   Lamport, L., *A new solution of Dijkstra's concurrent programming problem.* Commun. ACM, 1974. **17**(8): p. 453-455.

88.   Bonder, D.E. and K.D. McCarthy, *Astrocytic Gq-GPCR-linked IP3R-dependent Ca2+ signaling does not mediate neurovascular coupling in mouse visual cortex in vivo.* J Neurosci, 2014. **34**(39): p. 13139-50.

89.   Santos, S., et al., *Optically sectioned fluorescence endomicroscopy with hybrid-illumination imaging through a flexible fiber bundle.* J Biomed Opt, 2009. **14**(3): p. 030502.

90.   Mertz, J., *Optical sectioning microscopy with planar or structured illumination.* Nat Methods, 2011. **8**(10): p. 811-9.

91.   Lane, P.M., et al., *Fiber-optic confocal microscopy using a spatial light modulator.* Opt Lett, 2000. **25**(24): p. 1780-2.

92.   MacVicar, B.A. and E.A. Newman, *Astrocyte regulation of blood flow in the brain.* Cold Spring Harb Perspect Biol, 2015. **7**(5).

93.   Schaefer, A.T. and A. Claridge-Chang, *The surveillance state of behavioral automation.* Curr Opin Neurobiol, 2012. **22**(1): p. 170-6.

94.   Weiser, T.G., et al., *An estimation of the global volume of surgery: a modelling strategy based on available data.* Lancet, 2008. **372**(9633): p. 139-44.

95.   Slieker, J.C., et al., *Systematic review of the technique of colorectal anastomosis.* JAMA Surg, 2013. **148**(2): p. 190-201.

96.   Marano, L., et al., *Sutureless jejuno-jejunal anastomosis in gastric cancer patients: a comparison with handsewn procedure in a single institute.* BMC Surg, 2012. **12 Suppl 1**: p. S27.

97.   Vignali, A., et al., *Factors associated with the occurrence of leaks in stapled rectal anastomoses: a review of 1,014 patients.* J Am Coll Surg, 1997. **185**(2): p. 105-13.

98.   Neutzling, C.B., et al., *Stapled versus handsewn methods for colorectal anastomosis surgery.* Cochrane Database Syst Rev, 2012. **2**: p. CD003144.

99.   Ashburn, J.H., et al., *Consequences of anastomotic leak after restorative proctectomy for cancer: effect on long-term function and quality of life.* Dis Colon Rectum, 2013. **56**(3): p. 275-80.

100.   Calin, M.D., et al., *Colic anastomotic leakage risk factors.* J Med Life, 2013. **6**(4): p. 420-3.

101.   Lujan, J.J., et al., *Factors influencing the outcome of intestinal anastomosis.* Am Surg, 2011. **77**(9): p. 1169-75.

102. Kang, J.U., et al., *Real-time three-dimensional Fourier-domain optical coherence tomography video image guided microsurgeries.* J Biomed Opt, 2012. **17**(8): p. 081403-1.

103. Huang, Y., et al., *Microvascular anastomosis guidance and evaluation using real-time three-dimensional Fourier-domain Doppler optical coherence tomography.* J Biomed Opt, 2013. **18**(11): p. 111404.

104. Glatz, J., et al., *Concurrent video-rate color and near-infrared fluorescence laparoscopy.* J Biomed Opt, 2013. **18**(10): p. 101302.

105. Shademan, A., et al. *Feasibility of near-infrared markers for guiding surgical robots*. 2013.

106. Lu, G. and B. Fei, *Medical hyperspectral imaging: a review.* J Biomed Opt, 2014. **19**(1): p. 10901.

107. Kainerstorfer, J.M., P.D. Smith, and A.H. Gandjbakhche, *Noncontact Wide-Field Multispectral Imaging for Tissue Characterization.* Selected Topics in Quantum Electronics, IEEE Journal of, 2012. **18**(4): p. 1343-1354.

108. Panasyuk, S.V., et al., *Medical hyperspectral imaging to facilitate residual tumor identification during surgery.* Cancer Biol Ther, 2007. **6**(3): p. 439-46.

109. Arimoto, H., *Multispectral polarization imaging for observing blood oxygen saturation in skin tissue.* Appl Spectrosc, 2006. **60**(4): p. 459-64.

110. Roblyer, D., et al., *Multispectral optical imaging device for in vivo detection of oral neoplasia.* J Biomed Opt, 2008. **13**(2): p. 024019.

111. Liu, Y., et al., *Investigation of depth selectivity of polarization gating for tissue characterization.* Opt Express, 2005. **13**(2): p. 601-11.

112. Groner, W., et al., *Orthogonal polarization spectral imaging: a new method for study of the microcirculation.* Nat Med, 1999. **5**(10): p. 1209-12.

113. Jacques, S.L., J.C. Ramella-Roman, and K. Lee, *Imaging skin pathology with polarized light.* J Biomed Opt, 2002. **7**(3): p. 329-40.

114. Altan, A., et al., *Effect of collateral circulation on healing of small intestinal anastomosis in rabbits.* Hepatogastroenterology, 1997. **44**(16): p. 1046-50.

115. Lal, D., et al., *Current patterns of practice and technique in the repair of esophageal atresia and tracheoesophageal fistua: an IPEG survey.* J Laparoendosc Adv Surg Tech A, 2013. **23**(7): p. 635-8.

116. Sotoca, J.M., F. Pla, and J.S. Sanchez, *Band Selection in Multispectral Images by Minimization of Dependent Information.* Systems, Man, and Cybernetics, Part C: Applications and Reviews, IEEE Transactions on, 2007. **37**(2): p. 258-267.

117. Matioli, E., et al., *High-brightness polarized light-emitting diodes.* Light Sci Appl, 2012. **1**: p. e22.

118. McEwen, M.P., G.P. Bull, and K.J. Reynolds, *Vessel calibre and haemoglobin effects on pulse oximetry.* Physiol Meas, 2009. **30**(9): p. 869-83.

119. Frangi, A.F., et al., *Multiscale vessel enhancement filtering*, in *Medical Image Computing and Computer-Assisted Intervention — MICCAI'98: First International Conference Cambridge, MA, USA, October 11–13, 1998 Proceedings*, W.M. Wells, A. Colchester, and S. Delp, Editors. 1998, Springer Berlin Heidelberg: Berlin, Heidelberg. p. 130-137.

120. Park, B., et al., *Contaminant Classification of Poultry Hyperspectral Imagery using a Spectral Angle Mapper Algorithm.* Biosystems Engineering, 2007. **96**(3): p. 323-333.

121. Dennison, P.E., K.Q. Halligan, and D.A. Roberts, *A comparison of error metrics and constraints for multiple endmember spectral mixture analysis and spectral angle mapper.* Remote Sensing of Environment, 2004. **93**(3): p. 359-367.

122. Haber, H.P. and M. Stern, *Intestinal ultrasonography in children and young adults: bowel wall thickness is age dependent.* J Ultrasound Med, 2000. **19**(5): p. 315-21.

123. Chiorean, L., et al., *Transabdominal ultrasound for standardized measurement of bowel wall thickness in normal children and those with Crohn's disease.* Med Ultrason, 2014. **16**(4): p. 319-24.

124. Kainerstorfer, J.M., et al., *Direct curvature correction for noncontact imaging modalities applied to multispectral imaging.* J Biomed Opt, 2010. **15**(4): p. 046013.

125. Leonard, S., et al., *Smart tissue anastomosis robot (STAR): a vision-guided robotics system for laparoscopic suturing.* IEEE Trans Biomed Eng, 2014. **61**(4): p. 1305-17.

CURRICULUM VITAE

Jaepyeong Cha was born in Republic of Korea (South), October 17, 1983. He received his B.S. and M.S. degrees in Electrical and Computer Engineering and Biomedical Engineering from Seoul National University in 2007 and 2011, respectively. He enrolled in the Ph.D. program at the Johns Hopkins University, Baltimore, Maryland, in 2011. Since then, he worked under the guidance of Professor Dr. Jin U. Kang, in the Photonics and Optoelectronics group. His current research interests include functional brain imaging at cellular resolution in freely moving animals and medical imaging guided surgical intervention. He is a Howard Hughes Medical Institute International Student Research Fellow and student member of SPIE, OSA, and IEEE.